



UNIVERSITÄT
DES
SAARLANDES

Preparation, Properties and Application of Ionic Liquid-Derived Carbon-Based Catalysts for the Oxygen Reduction Reaction

Dissertation

zur Erlangung des Grades
des Doktors der Naturwissenschaften
der Naturwissenschaftlich-Technischen Fakultät
der Universität des Saarlandes

von

Zhenzhen Wang

Saarbrücken
2023

Tag des Kolloquiums: 28.04.2023

Dekan: Prof. Dr. Ludger Santen

Berichterstatter: Prof. Dr. Dr. h.c. Rolf Hempelmann

PD Dr. Guido Falk

Vorsitz: Prof. Markus Gallei

Akad. Mitarbeiter: Dr. Haibin Gao

**Preparation, Properties and Application of Ionic
Liquid-Derived Carbon-Based Catalysts for the
Oxygen Reduction Reaction**

Zhenzhen Wang

geb. in Wuhan, China

DISSERTATION

Universität des Saarlandes, Saarbrücken

Acknowledgements

I am entirely thankful for those who helped me during the tough times on my journey to earn a Ph.D. Without their supports and efforts, I would not have been able to accomplish my Ph.D.

First and foremost, I would like to express gratitude to my advisors, Professor Rolf Hempelmann and Professor Shichun Mu. I could not wish for better mentors than they do with guidance on scientific training and personality shaping. I am grateful for the continued support from Professor Hempelmann and the inclusive atmosphere in the highly diversified research groups. I appreciate the precious opportunity from Professor Mu to collaborate with his robust and productive team. Also, special mention to those I worked with at Transfercentre Sustainable Electrochemistry (TSE) at Saarland University and Wuhan University of Technology: Dan Durneata, Dina Klippert, Daniel Rauber, Galina Skorikova, Sylvia Kuhn, PD. Dr. Harald Natter, Huihui Jin, Jiawei Zhu, Manjie Xiao. There are also many people I have met that helped me a lot, that it is difficult to thank them all. I am truly grateful.

Finally, I want to express my eternal gratitude to my family who has supported me throughout my life. Especially to my mother, Guangrong, who always encourages me to keep positive in all of my endeavors and gives all the best she has to support me. To my husband, Xiaozhuang, thank you for all the good and bad times we have had together. To my son, Mulin, thanks for the happiness brought to my life.

Abstract

Clean energy storage and conversion technologies are in high demand as the energy crisis and environmental concerns impose tremendous pressure on the sustainability of modern human society. However, the noble-metal catalysts required in oxygen reduction reaction (ORR) remain an obstacle impeding the broad application of clean technologies such as fuel cells and metal-air batteries. So far, many advancements have been achieved with non-noble metal alternative catalysts, especially carbon-based ones. Ionic liquids possess low volatility, high solubility, and tunable composition, making them ideal candidates as carbonaceous precursors. This thesis adopted ethyl-methyl-imidazolium dicyanamide, [emim] [DCA], as an example to prepare nitrogen-doped carbon nanotubes (N-CNTs) composites and porous nitrogen-doped carbons with core-shell structured FeCo alloy nanoparticles for ORR. The correlation between the obtained catalysts and ORR catalytic activity was investigated and their potentials in the rechargeable Zn-air battery were also presented.

Zusammenfassung

Saubere Energiespeicher- und -umwandlungstechnologien sind sehr gefragt, da die Energiekrise und Umweltbelange einen enormen Druck auf die Nachhaltigkeit der modernen menschlichen Gesellschaft ausüben. Die für die Sauerstoffreduktionsreaktion (ORR) erforderlichen Edelmetallkatalysatoren bleiben jedoch ein Hindernis, das die breite Anwendung sauberer Technologien wie Brennstoffzellen und Metall-Luft-Batterien behindert. Bisher wurden viele Fortschritte mit alternativen Nichtedelmetallkatalysatoren erzielt, insbesondere mit solchen auf Kohlenstoffbasis. Ionische Flüssigkeiten besitzen eine geringe Flüchtigkeit, eine hohe Löslichkeit und eine einstellbare Zusammensetzung, was sie zu idealen Kandidaten als kohlenstoffhaltige Vorstufen macht. Diese Dissertation nahm Ethyl-Methyl-Imidazolium-Dicyanamid, [emim] [DCA], als Beispiel zur Herstellung von Stickstoff-dotierten Kohlenstoff-Nanoröhren (N-CNTs)-Kompositen und porösen Stickstoff-dotierten Kohlenstoffen mit Kern-Schale-strukturierten FeCo-Legierungs-Nanopartikeln für die ORR. Die Korrelation zwischen den erhaltenen Katalysatoren und der katalytischen ORR-Aktivität wurde untersucht und ihr Potenzial in der wiederaufladbaren Zn-Luft-Batterie wurde ebenfalls vorgestellt.

Table of Contents

Acknowledgements	I
Abstract	II
Zusammenfassung	III
Table of Contents	IV
1. Background and Introduction	1
1.1. Fundamentals of Electrocatalytic Oxygen Reduction Reaction	3
1.2. Non-Noble Metal Carbon-Based ORR Electrocatalysts	6
1.2.1. Metal-Free Carbon-Based ORR Electrocatalysts	7
1.2.2. Transition Metal Carbon-Based ORR Electrocatalysts	14
1.3. Ionic Liquid-Derived Carbon-Based ORR Electrocatalyst	21
1.3.1. Metal-Free Carbon-Based ORR Electrocatalysts	23
1.3.2. Transition Metal/Carbon-Based ORR Electrocatalysts	26
1.3.3. Porous Structure Engineering	27
1.4. Motivation and Scope of This Thesis	31
2. Characterization Methods	33
2.1. Physicochemical Characterization	33
2.2. Electrocatalytic Measurements	36
2.2.1. Preparation of Working Electrode	36
2.2.2. ORR Measurement	36
2.2.3. Catalyst Stability Test	40
2.2.4. Catalyst Anti-poisoning Test	40
2.2.5. OER Measurement	41
2.3. Zn-Air Batteries Assembly and Measurements	41

3. Template-Promoted Synthesis of Nitrogen-Doped CNTs from Ionic Liquid for Enhanced ORR Activity	43
3.1. Introduction	44
3.2. Experimental Section	46
3.3. Results and Discussion	47
3.3.1. N-CNTs Formation Mechanism	47
3.3.2. Effects of Silica-Template on Catalyst Compositions and Structures	53
3.3.3. Electrocatalytic ORR Performance of Catalysts	60
3.4. Conclusion	65
4. Ionic Liquid-Derived FeCo Alloys Encapsulated in Nitrogen-Doped Carbon Framework as Advanced Bifunctional Catalysts for Zn-Air Batteries	67
4.1. Introduction	68
4.2. Experimental Section	71
4.3. Results and Discussion	72
4.3.1. Material Characterization Results	72
4.3.2. Electrocatalytic Performance toward ORR&OER	79
4.3.3. Liquid and All-Solid-State Zinc–Air Batteries Performance	88
4.4. Conclusion	91
5. Conclusions and Outlooks	93
5.1. Conclusions	93
5.2. Outlook	95
6. References	96
7. Publications	109
8. Eidesstattliche Versicherung	110

Chapter 1

1. Background and Introduction

With the growing world population and increasing energy consumption, our planet suffers from the negative consequences of industrial expansion powered by fossil resources (oil, gas, and coal), such as global warming, environmental pollution and energy crisis. To meet these challenges, countries and regions have been making long-term commitments to reduce the use of fossil fuels under the 1.5-degree goal of the Paris Agreement. In recent decades, we have witnessed robust growth in deploying renewable energies (such as solar photovoltaic (PV), wind and hydrogen). Up to 2020, the global renewable generation capacity has amounted to 2 799 GW, accounting for more than a quarter of total power generation. However, the uptake of renewables has been slower in end-use sectors such as residential applications, electric vehicles, and stationary power plants. It requires a surge in clean energy technologies and infrastructure to accelerate renewable energy deployment and meet with the net zero emissions targets under the architecture of the Paris Agreement.[1]

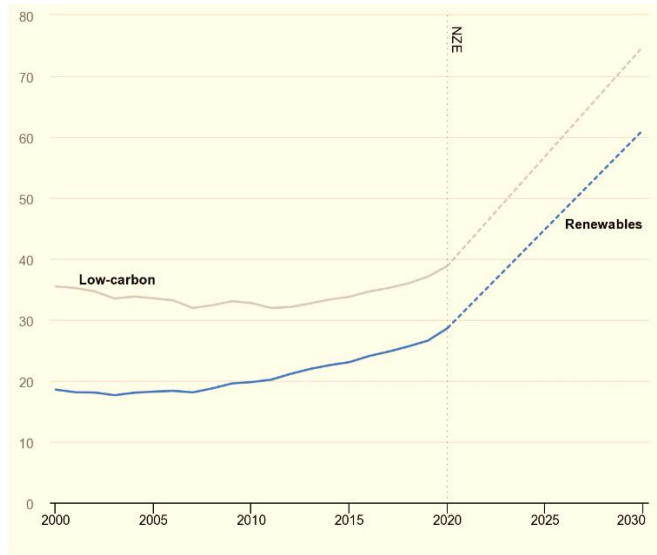


Figure 1.1 Renewables and low-carbon share in power generation in the Net Zero Scenario, 2000-2030.

Adapted from ref.[1]

In this scenario, proton exchange membrane fuel cells (PEMFCs) and metal-air batteries, as the representatives of clean energy storage and conversion technologies, have attracted extensive attention. PEMFCs are new-generation energy conversion technologies that can continuously convert the chemical energy of hydrogen and oxygen redox reactions to electrical energy. The distinguishing features of PEMFCs include high power density, high conversion efficiency, zero pollution emission, and high operation reliability, which make the PEMFCs attractive for civilian and military applications in transportation, distributed stationary power plants, and portable devices.[2] Apart from that, metal-air batteries, especially zinc-air batteries (ZABs), are also promising candidates for future electric vehicles and other energy-consumption devices by virtue of their high theoretical energy density ($1086 \text{ Wh}\cdot\text{kg}^{-1}$), low price (<10\$ per kWh estimated) and good safety. However, the large-scale commercialization of PEMFCs and metal-air batteries is impeded by the deficiency of cost-effective, highly active and durable oxygen-reduction electrocatalysts. As the pivotal reaction on the cathode, ORR at the electrode

usually requires an efficient electrocatalyst to overcome the sluggish kinetics and boost the reaction rate so that a desirable overall system performance in energy techniques is enabled.[3] Therefore, it's highly important to develop efficient ORR catalysts.

1.1. Fundamentals of Electrocatalytic Oxygen Reduction Reaction

Discussions about oxygen reduction reaction mechanisms beforehand would provide direct implications for designing catalysts. The electrocatalytic oxygen reduction reaction generally occurs at the catalyst interface where the heterogeneous catalytic processes in between triple-phases of solid catalysts, aqueous electrolytes, and gaseous reactants and intermediates. There are a total of four net coupled proton and electron transfers (CPETs) in a complete electrochemical ORR either via a “direct” 4e⁻-reduction to H₂O (in an acidic medium) and OH⁻ (in an alkaline medium) or via a two-step 2e⁻-pathway which involves a reduction to hydrogen peroxide (in acidic medium) and HO₂⁻ (in alkaline medium) as the intermediate species, followed by the further reduction to H₂O.[4] The comprehensive reaction path of ORR in acidic and alkaline electrolyte are summarized in

Table 1.1.

Table 1.1 Oxygen reduction reaction pathways in an acidic and alkaline electrolyte, respectively.

	two-step 2e pathway	direct four-electron pathway
Acidic solution	$O_2 + 2H^+ + 2e^- \rightarrow 2H_2O_2$ (0.695V vs. SHE) $H_2O_2 + 2H^+ + 2e^- \rightarrow 2H_2O$ (1.776V vs. SHE)	$O_2 + 4H^+ + 4e^- \rightarrow 2H_2O$ (1.229V vs. SHE)
Alkaline solution	$O_2 + H_2O + 2e^- \rightarrow HO_2^-$ (-0.076V vs. SHE) $HO_2^- + H_2O + 2e^- \rightarrow 3HO^-$ (0.878V vs. SHE) $2HO_2^- \rightarrow 2HO^- + O_2$ (disproportionation of H ₂ O ₂)	$O_2 + 2H_2O + 4e^- \rightarrow 4OH^-$ (0.401V vs. SHE)

From the view of proton and electron transfer sequences, the kinetic of ORR on catalysts involves four key steps (**Figure 1.2**):

- The adsorption of oxygen at the surface of catalysts
- The coupled electron/proton transfer of ORR
- Splitting of O=O bond
- The desorption of the intermediate species and product

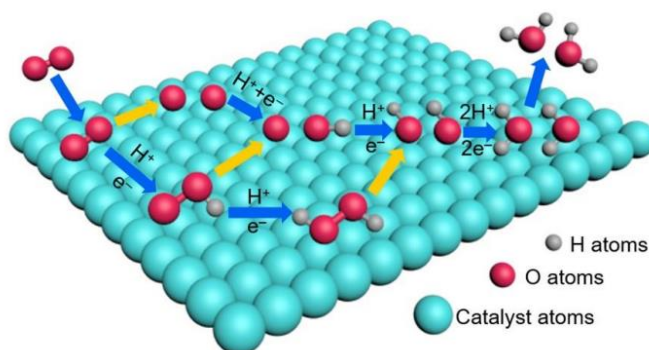


Figure 1.2 Schematic representation of the reaction pathway for ORR and the resulting intermediates on the surface of a catalyst. The blue arrows show the proton/electron transfer. The yellow arrows indicate the O-O bond cleavage. Adapted from ref.[5]

The rate-determining step (RDS) which identified as the elementary reaction with the minimum reaction free energy is of paramount importance. Much effort has been devoted to recognizing the rate-determining step (RDS). Previous reports have discovered that the adsorption of O₂ as OOH* or the desorption of OH* as water is most likely the RDS. Nørskov modulated the ORR on Pt (111) surface and proposed the dissociative or associative mechanism established on the oxygen dissociation energy barrier on the catalyst surface. As shown in **Table 1.2**, the dissociative mechanism involves the O–O bond breaking in O₂ and the protonation of O* to OH* and H₂O, and the associative mechanism involves the chemisorption of the O₂ molecule and direct proton/electron transfer to it and to OOH*, which breaks into O* and OH* and finally form H₂O.[6]

Table 1.2 Two possible ORR mechanisms: associative and dissociative mechanisms in an acidic and alkaline electrolyte, respectively.

	Dissociative mechanism	Associative mechanism
Acidic solution	$O_2(g) + 2* \rightarrow 2O^*$ $2O^* + 2H^+ + 2e^- \rightarrow 2OH^*$ $2OH^* + 2H^+ + 2e^- \rightarrow 2H_2O(l) + 2*$	$O_2(g) + * \rightarrow O_2^*$ $O_2^* + H^+ + e^- \rightarrow OOH^*$ $OOH^* + H^+ + e^- \rightarrow O^* + H_2O(l)$ $O^* + H^+ + e^- \rightarrow OH^*$ $OH^* + H^+ + e^- \rightarrow H_2O(l) + *$
Alkaline solution	$O_2(g) + 2* \rightarrow 2O^*$ $O^* + H_2O(l) + e^- \rightarrow OH^* + OH^-$ $OH^* + e^- \rightarrow OH^- + *$	$O_2(g) + * \rightarrow O_2^*$ $O_2^* + H^+ + e^- \rightarrow OOH^* + OH^-$ $OOH^* + e^- \rightarrow O^* + OH^-$ $O^* + H_2O(l) + e^- \rightarrow OH^* + OH^-$ $OH^* + e^- \rightarrow OH^- + *$
where * denotes the active site on electrocatalyst, (l) and (g) refer to liquid and gas phases, respectively, and O*, OH* and HOO* are the intermediates adsorbed on active sites		

Density functional theory (DFT) modeling is a valuable computational tool for studying the ORR electrocatalysis by establishing theoretical models to gain in-depth understanding to active sites and reaction mechanisms. It helps to how elementary reaction energetics are impacted by electrocatalysis composition and structure. More importantly, DFT calculations can explain and predict catalytic behavior at the atomic level, which provides valuable guidance for the design of efficient ORR catalysts.[7] Nørskov correlated the free energy of intermediates from DFT calculations of their adsorption energy and evaluated their relationship with the electrode potential, suggesting that a proper catalyst should possess moderate adsorption energy that should bind atoms and molecules not too weakly so that it can activate the reactants, and not too strongly to desorb the intermediate/final products. Due to the complex reaction and sluggish kinetic

process at the three-phase interface of cathode, ORR electrocatalysts have become the major bottleneck to realizing the large-scale application of clean energy technologies.

1.2. Non-Noble Metal Carbon-Based ORR Electrocatalysts

The cathodic oxygen reduction reaction (ORR) is approximately six or more orders of magnitude kinetically slower than the anodic hydrogen oxidation reaction, diminishing overall system efficiency. At present, platinum group materials (PGM) have been the most commonly used catalysts in ORR because of their high activity and selectivity towards the effective $4e^-$ pathway oxygen reduction.[8] Duan et al. have reported the type of jagged platinum nanowires as an advanced ORR catalyst that exhibited ultra-high mass activity of $13.6 \text{ A mg}^{-1} \text{ Pt @}0.9 \text{ V}$.[9] Nevertheless, the high cost and scarcity of PGM significantly inhibit their wide deployment. Moreover, the sluggish kinetics of ORR usually demand high Pt loadings to overcome the reaction barrier. As a result, the expense of Pt catalyst makes up about 50% of the overall cost of a fuel cell system, according to the white book proposed by the US Department of Energy, with a Pt loading of $5 \text{ kW}\cdot\text{g}^{-1}$.[10, 11] Aside from the high cost, PGM catalysts suffer from dramatic degradation under corrosive operation conditions, that platinum nanoparticles aggregation and detachment from the carbon support and is prone to time-dependent drift, methanol crossover, and carbon monoxide(CO) deactivation.[12] Thus, there is a pressing need to developing non-precious metal-based alternatives for the scalable implementation of new energy conversion technologies in the long-term economic prospects.

Carbon-based electrocatalysts have been regarded as promising alternatives to noble metals featuring multiple advantages of earth abundance, low price, high electronic conductivity, robust tolerance under acidic/alkaline operation conditions, and structural

and morphological tenability at molecular levels. The two main categories of non-noble metal carbon-based catalysts are metal-free carbon-based catalysts and transition metal carbon-based catalysts.

1.2.1. Metal-Free Carbon-Based ORR Electrocatalysts

Pristine carbon is constructed from graphene units that consists of an ordered array of hexagonal honeycombs of carbon atoms with a large sp^2 -hybridized π -conjugation system. A defect-free graphitic structure is chemical-inert to adsorb or activate O_2 and intermediates in the ORR. It has been revealed that introducing heteroatom-dopant or constructing defects would break the integrity of the π conjugation to activate the sp^2 carbon atoms to be electrocatalytic-active.[13]

1.2.1.1. Heteroatom-Doped Carbon-Based ORR Electrocatalysts

Heteroatom-doping is the strategy to replace carbon atoms with heteroatoms in a certain position. The introduction of heteroatoms with different sizes and electronegativity results in (i) charge redistribution and asymmetry spin state which enhance the chemical absorption of O_2 and intermediates in ORR, and (ii) electron transfer between inhomogeneous atoms which facilitate ORR. DFT calculations also show that the electrocatalytic activity of non-metallic carbon-based catalysts is highly relevant to the altered electron spins and charge redistribution induced by doping.[14, 15]

It could date back to 2009 when Dai and coworkers discovered the first nitrogen-doped carbon nanotube array to be electrocatalytic active for oxygen reduction reaction (ORR). The ground-breaking work revealed that charge redistribution induced by nitrogen doping reduces the oxygen molecule adsorption and dissociation energy on adjacent positively-charged carbon atoms, leading to enhanced electrocatalytic activity towards

ORR.[16] Subsequently, B, O, F, Si, P, S, Cl, Se, Br, and I have been utilized as single or multiple dopants to further improve the electrocatalytic activity of the carbon materials. As shown in **Figure 1.3**, the impact of heteroatoms on the electronic structure of carbon frameworks depends on the absolute difference in electronegativity between heteroatoms and C atoms. [17]

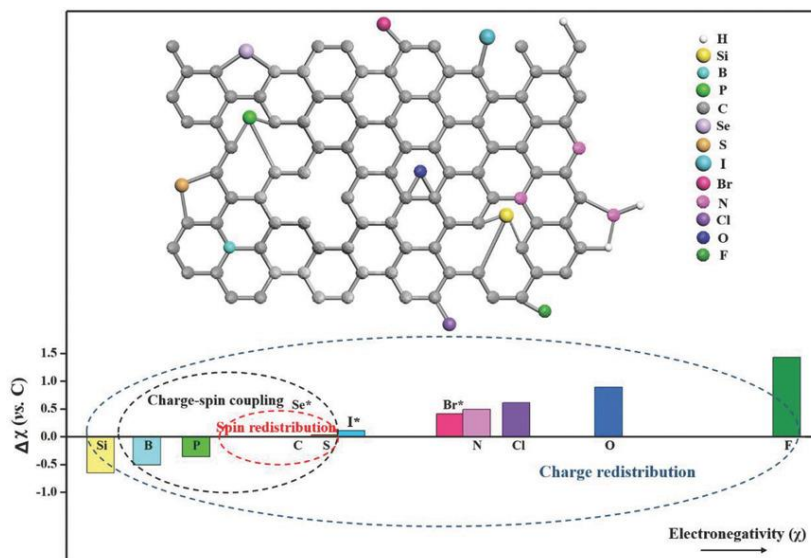


Figure 1.3 Illustration on hetero-doped carbon materials. Upper panel: atomic configurations of different heteroatoms doped in carbon lattice. Lower panel: different origin of doping effects as charge-redistribution, spin redistribution, and charge–spin coupling based on the relative electronegativity of heteroatom dopants. Se, Br, and I labeled with the superscript of * are too large to be incorporated into the carbon lattice and spatial distortion has to be considered for inducing catalytic activities. Adapted with permission from respective publisher. Adapted from ref.[17]

Because the nitrogen atom has a similar atomic size to carbon and a lone electron pair that can be donated to the sp^2 -hybridized π -conjugation system of the carbon network, it has been recognized as the most effective hetero-dopant which can simultaneously alter the chemical stability, surface polarity, electric conductivity, and electron-donor properties of carbon materials. Typically, four dominant nitrogen atoms in

the carbon skeleton are involved in electrocatalytic ORR, such as pyridinic N, pyrrolic N, quaternary N and pyridinic-N-oxide as the atomic configuration illustrated in **Figure 1.4 (a)**. The correlation between different types of nitrogen and their electrocatalytic activity towards ORR have been extensively explored and debated. Guo et al. finely tuned the configuration of nitrogen atoms on the platform of highly oriented pyrolytic graphite (HOPG) and evidenced that carbon atoms adjacent to pyridinic N are active in ORR (**Figure 1.4 (b)**). [18] Dai's group demonstrated with CNTs that the carbon atoms adjacent to the nitrogen atom show a higher positive charge density, which balances the strong electron affinity of the nitrogen atom. The incorporation of nitrogen atoms changes the chemisorption mode of O₂ from conventional end-on adsorption (Pauling model) to side-on adsorption (Yeager model) on the surfaces of nitrogen-doped carbon nanotubes (**Figure 1.4 (c)**). This parallel diatomic adsorption can effectively weaken the oxygen-oxygen (O-O) bond, thereby promoting the ORR process on the surface of N-CNTs.[16] The associative mechanism through direct four-electrons pathway on N-doped carbon materials in acidic electrolyte was proposed by Kim et al. Based on the DFT calculation of the adsorption energy of oxygen on the carbon atoms adjacent to pyridinic N sites and the energy barrier for the first electron transfer, which assumed as the rate determining step. As shown in **Figure 1.4 (d)**, the carbon located on the edge and adjacent to a valley graphitic N atom exhibited the lowest energy barrier for the first electron transfer coupled with a relatively low oxygen adsorption energy. After a water molecule is released, the C-N bond was cleaved by the adsorbed oxygen atom (observed by experiment) and formed a stable CHO group and a pyridinic N. It indicated that graphitic N and pyridinic N play vital parts in the four-electron reduction of oxygen.[19]

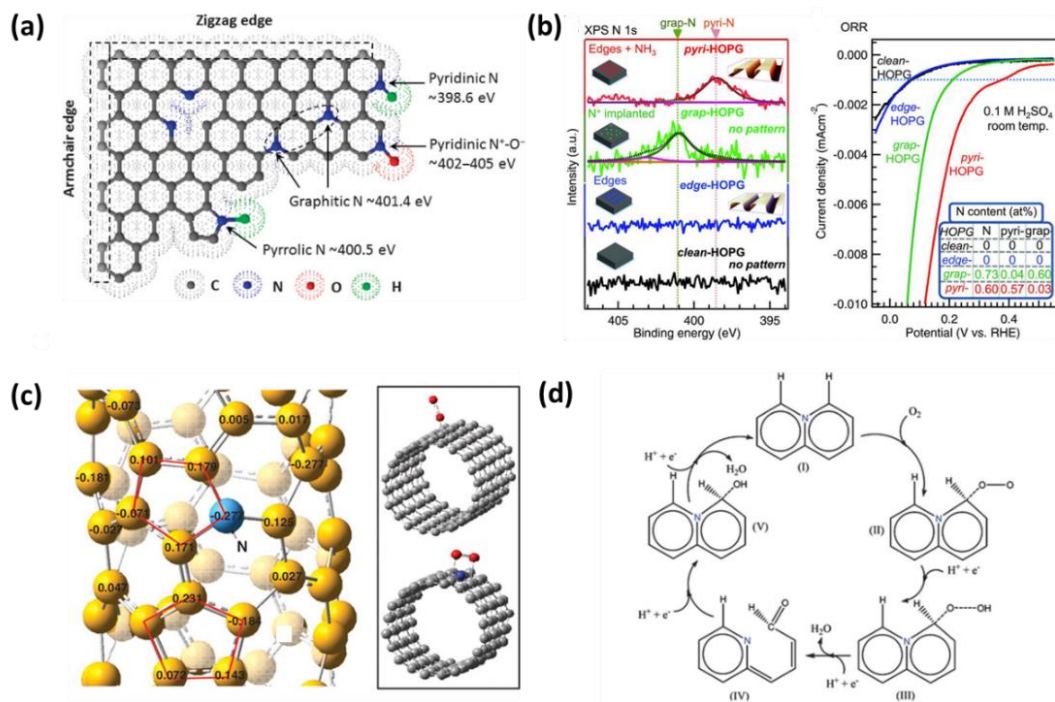


Figure 1.4 a) Scheme illustration of nitrogen species in nitrogen-containing graphitic carbons.[20] b) N 1s XPS spectra of model catalysts and ORR results for model catalysts corresponding to (Nitrogen contents of the model catalysts are shown in the inset,[18] c) Calculated charge density distribution for NCNTs and schematic representations of adsorption modes of an oxygen molecule in CCNTs and NCNTs, [16] d) Schematic pathway of the ORR on nitrogen-doped carbon catalysts. Adapted from ref.[19]

Although carbon materials doped nitrogen have exhibited good ORR catalytic activity, their performance can be further enhanced by codoping (N-S, N-P, N-B) or multi-doped (N-S-P, N-O-S, N-S-B) because of the synergistic electronic interaction between different dopants.[21-23] Dai's group designed and prepared the B, N-codoped CNTs[24] and graphene[25] and investigated the effects of the B, N-codoping on the ORR activities (**Figure 1.5 (a) – (b)**). It was found that the B, N-codoped graphene with an optimized ratio (B: C: N =12:77:11) exhibited the highest activity in ORR, compared to its single doped counterparts (**Figure 1.5 (c-d)**). [26]

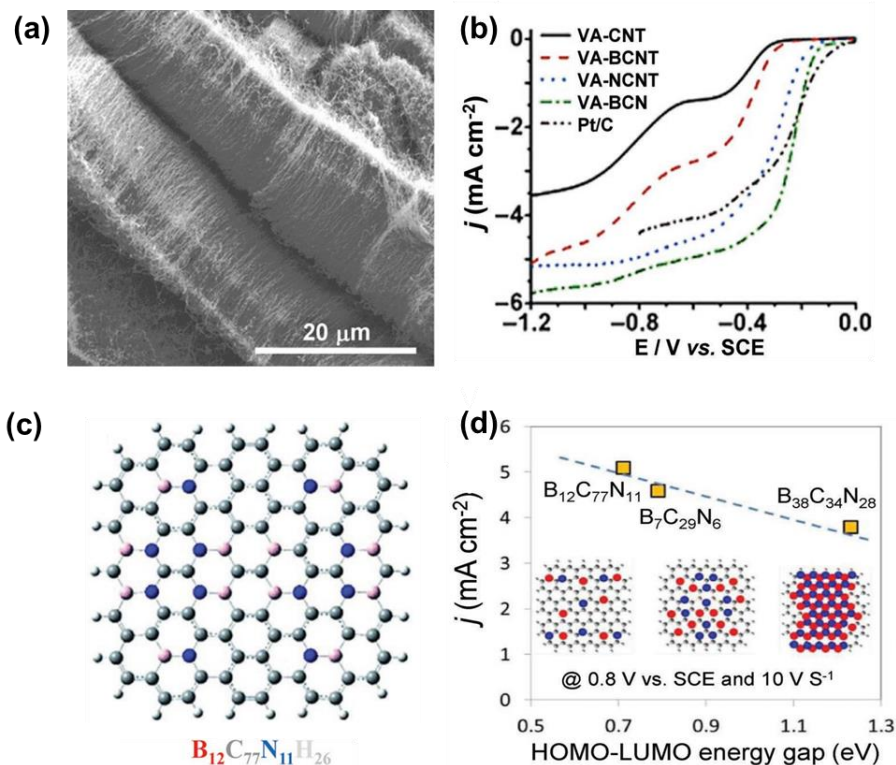


Figure 1.5 a) Scanning electron microscope (SEM) image of B, N-codoped vertically aligned carbon nanotubes (VA-BCN). b) LSVs of various electrodes in O₂-saturated 0.1 m KOH electrolyte. c) B, N-codoped graphene (BCN) model of B₁₂C₇₇N₁₁H₂₆. Gray ball: C, White ball: H, Pink ball: B, Blue ball: N. d) Experiment ORR current density versus HOMO–LUMO energy gap (from DFT calculation) for BCN. Adapted from ref.[24, 25]

Furthermore, the introduction of different heteroatoms endows carbon materials with multiple catalytic active sites capable of catalyzing ORR, OER, and HER simultaneously, appealing to application in rechargeable metal-air batteries and water-splitting systems. Qiao and co-workers reported an effective strategy for preparing N,S-codoping carbon nanotubes from CNTs and polydopamine precursors (**Figure 1.6 (a)**).[27] It was found that N,S-CNT can be applied as the HER and OER electrocatalysts simultaneously, due to delicate effects of the secondary heteroatom-doping on electronic structures of the catalytic active sites (**Figure 1.6 (b) – (c)**). Zhang et al. reported the first N-P-codoped

mesoporous nanocarbon foams as efficient bifunctional catalysts for ORR and OER in high-performance primary and rechargeable Zn–air batteries.[28]

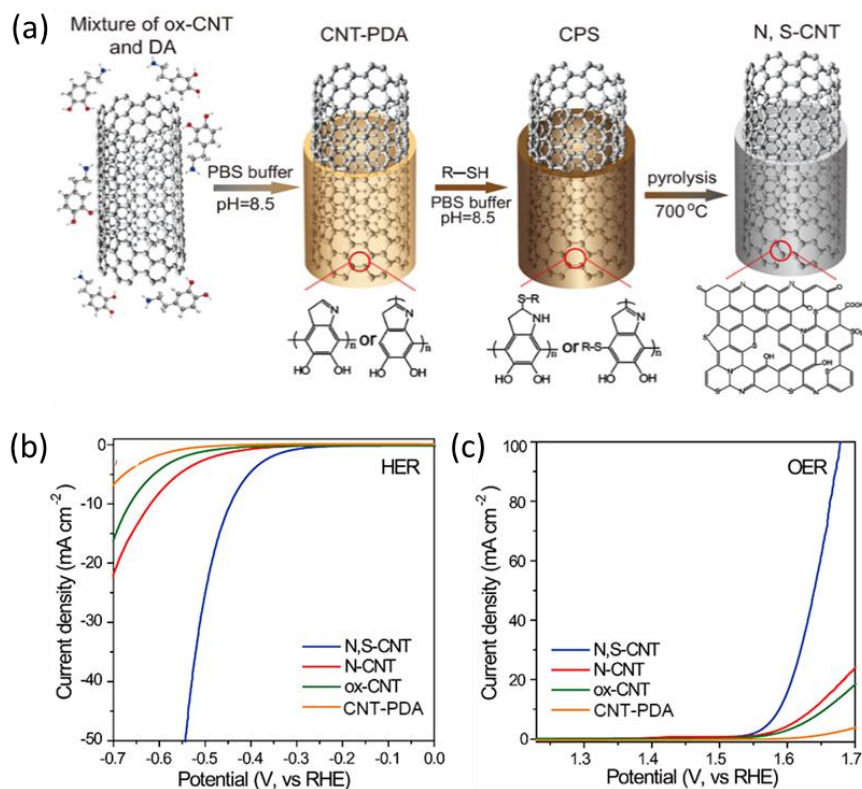


Figure 1.6 a) Fabrication of the N, S-CNT following a two-step “graft-and-pyrolyze” route, b) The HER polarization curves, c) The OER polarization curves. Adapted from ref.[27]

1.2.1.2. Intrinsic Defective Carbon-Based ORR Electrocatalysts

Like hetero-atom doping, augmenting intrinsic carbon defects such as edges, vacancies, and holes is another essential strategy to break the integrity of π -conjugation and make the adjacent carbon atoms active for the ORR.[29-31] Divacancy G585 defect (topological defect contains two pentagons and one octagonal), as a representative defect, has been widely studied as a model to probe the ORR mechanism of defective carbons (**Figure 1.7 (a)**). With theoretical DFT calculation and experimental results, Yao’s group found that graphene with G585 defects could facilitate oxygen adsorption and lower

the energy barrier for the intermediate reactions(**Figure 1.7 (b)**).[32] Wang's group compared the activity of carbon atoms on basal plane and edge defects in the carbon network by using a micro apparatus on a highly oriented pyrolytic graphite (HOPG) platform (**Figure 1.7 (c) – (d)**). It revealed that the higher ORR activity of the HOPG edges was attributed to the higher charge densities.[33]

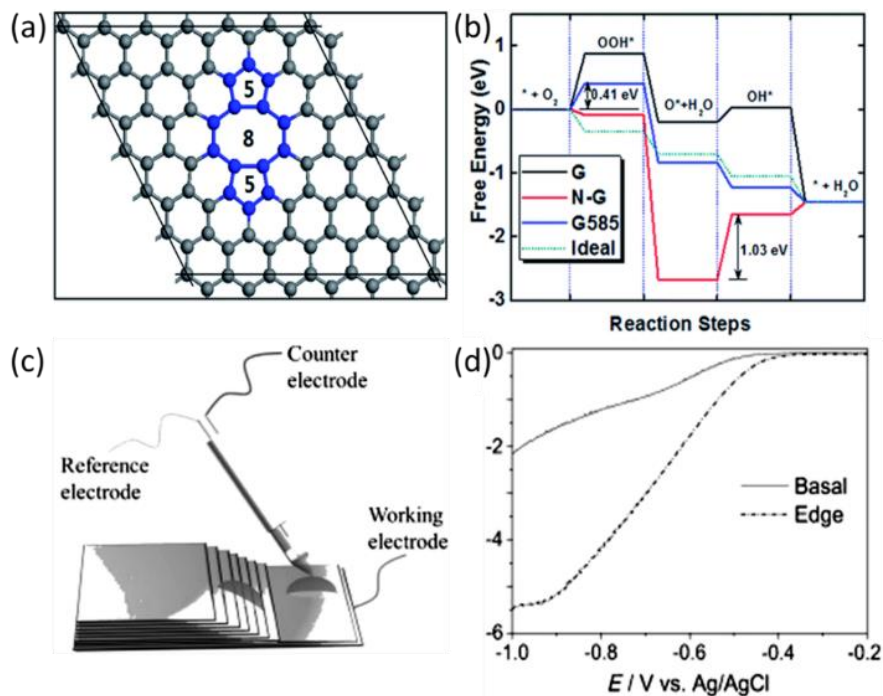


Figure 1.7 a) The topology of G585 defects in graphene, b) calculated free energy diagram of perfect monolayer graphene (G), N-doped graphene (N-G), graphene with G585 defects (G585) and an ideal catalyst (Ideal) for the ORR at the equilibrium potentials, [32] c) Micro apparatus for the ORR electrochemical experiment, d) LSV curves of the ORR tested for a droplet located either on edge or on the basal plane of the HOPG. Adapted from ref.[33]

In spite of the great advances in non-metallic carbon-based materials, there are still deficiencies in understanding the doping effects considering the various dopant types, locations, and distribution in diverse carbon catalysts. Moreover, the comprehensive

electrocatalytic performance of current non-metallic carbon-based catalysts is unable to meet the expectations of the clean energy conversion devices in realistic scenario.

1.2.2. Transition Metal Carbon-Based ORR Electrocatalysts

In 1964, Jasinski first reported that phthalocyanine cobalt could reduce oxygen in an alkaline environment.[34] This discovery has sparked studies about different phthalocyanine complexes with different central atoms (Fe, Co, Ni, Cu) and distinct metal-chelating structures (M-N₄, M-N₂O₂, M-N₂S₂, M-O₄, M-S₄). However, these phthalocyanine complexes exhibit inferior activity and stability than Pt-base catalysts, especially in acidic electrolytes. In 1976, Jahnke made a breakthrough about phthalocyanine compounds and found (1) the activity of phthalocyanine complexes is higher than their macrocycles; (2) combining phthalocyanine complexes with carbon can increase the ORR activity; (3) the heat treatment is crucial to improve the electrocatalytic activity and stability in acidic solutions.[35, 36] But note that the original metal-coordination structures in the phthalocyanine macrocycles are demolished during pyrolysis, which results in poor electrocatalytic activity and stability. Moreover, the expensive phthalocyanine macrocycle precursors boost up the cost of catalyst synthesis. In 1989, Yeager's group found that highly active ORR catalysts can be fabricated through the pyrolysis of the transition metal salts, nitrogen sources and carbon precursors, which essentially replaced the expensive macrocycle precursors.[37, 38] Later, a Fe-based nitrogen-doped carbon (Fe-N-C) catalyst was developed by Dodelet's group, which exhibited a remarkable volumetric activity of 230 A cm⁻³ (at 0.80 V vs. RHE) in PEMFC testing.[39]

Hence the transition metal and nitrogen co-doped carbon composite materials have been recognized as the most promising candidates for ORR in both acidic and alkaline electrolytes. In the following parts, reviews on the recent advancements will focus on the two main categories: (I) atomic structured transition metal-nitrogen-carbon (M-N_x-C) catalysts; (II) transition metal compound (metal oxides, chalcogenides, nitrides and oxynitrides) embedded with N-doped carbon materials.

1.2.2.1. M-N_x-C

The M-N_x-C-type catalysts are the most promising alternative non-noble metal catalysts with outstanding ORR activity in both acidic and alkaline electrolytes. The M-N_x (M = Fe, Co, Mn, Ni, Cu, Zn, etc.) coordinated sites are regarded as the main active centers in the M-N_x-C catalyst, in which the transition metal is coordinated with the surrounding nitrogen atoms. The coordinated nitrogen atoms are mainly pyridinic or pyrrolic nitrogen, and the variable coordination number *x* leads to the different M-N_x chemical configuration with varied activity in ORR electrocatalysis.

To date, great progress has been made in identifying and elucidating the precise chemistry of the active sites and their catalytic mechanism of ORR with the help of sophisticated in situ and ex situ characterization techniques in combination with theoretical calculations.[40] Dodelet et al. prepared Fe\N\C catalysts using two metal precursors (iron acetate and iron porphyrin) and analyzed the composition of the catalyst activity sites with a time-of-flight secondary ion mass spectrometer (TOF-SIMS).[41] By tracking the FeN_xC_y species evolution process, they found that FeN₄C_y⁺, FeN₃C_y⁺, and FeN₁C_y⁺ came from FeN₄/C, while FeN₂C_y⁺ came from FeN₂/C, demonstrating the co-existence of FeN₄/C and FeN₂/C active sites in the Fe\N\C catalyst. Ten years later, they

distinguished three different spin states at FeN₄ sites of Fe (II)-centered moieties by the Fe Mössbauer spectroscopy. As shown in **Figure 1.8**, only FeN₄/C in the low-spin state and N-FeN₂₊₂/C in the high-spin exhibited activity for ORR and resistance to acid in acidic media, while FeN₂₊₂/C in the medium-spin state was inactive. Among different species, the combination of high-spin state N-FeN₂₊₂/C and adjacent protonated alkaline nitrogen (N-FeN₂₊₂...NH⁺) showed the highest catalytic activity towards ORR.[42] Zitolo et al. employed X-ray absorption near-edge spectroscopy (XANES) spectra to study the active site structure of amorphous Fe-N-C catalysts which are quasi-free of crystallographic iron. It was uncovered that two planar FeN₄ porphyrinic structures integrated into graphene sheets (FeN₄C₁₂) could absorb oxygen in the side-on or end-on modes, which facilitate O₂ adsorption.[43] In addition, Li et al. utilized ex-situ and in-situ XAFS spectroscopy to detect the local structure and oxidative valence at Fe-N₄ sites in the ORR process. The results showed that the non-planar Fe-N₄ moiety could reversibly transform to a planar ferric Fe-N₄ moiety under the Fe^{2+/3+} redox potential, which attracts oxygen adsorbates.[44] This research provided strong evidence for the dynamic changes of the catalyst in the ORR process and promoted an in-depth understanding of the active structure.

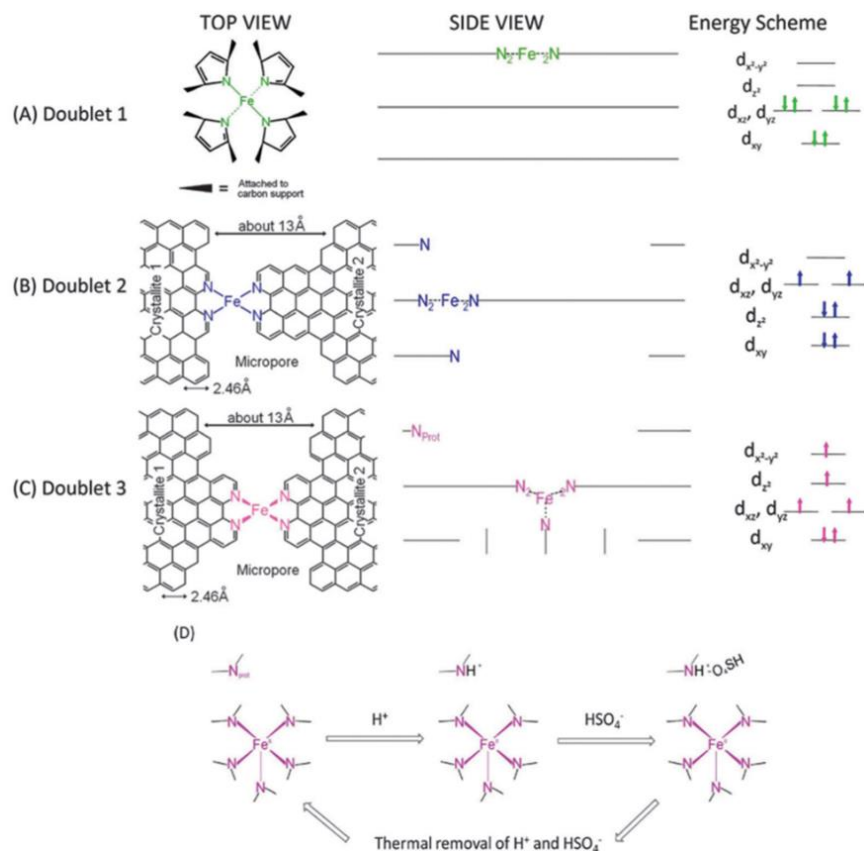


Figure 1.8 Schematic of the proposed active structures. Adapted from ref.[42]

According to the Sabatier principle, the high activity of the M-N_x sites would be attributed to the moderate adsorption energy adsorption to bind the ORR intermediate not too weakly so that it can activate the reactants and not too strongly to desorb the intermediate/final products.[6, 45] Extensive research works have proven that the Fe-N₄ structure embedded in the carbon matrix is one of the most common ORR active sites.[46-49] Zelenay's team used DFT to calculate the reaction path and thermodynamic limiting potential of Fe-N₄ sites located at two different positions in bulk and zigzag edges. They found that Fe-N₄ sites at different positions follow different ORR reaction pathways, where the edge-based Fe-N₄ sites can absorb OH⁻ spontaneously, which facilitates ORR process.[50]

Besides the iron-based catalysts, the active sites of other transition metal-based catalysts, such as Co,[51, 52] Mn,[53, 54] Cu,[55, 56] Ni,[57, 58] Zn,[59, 60] etc., have also been extensively investigated and the M-N₄ site is generally recognized as the main active sites for ORR. Although the M-N₄ site has been proven to be highly ORR active, there is controversy over the coordination number of Nitrogen atoms.[61] Some studies suggest that the M-N₂ site exhibits better catalytic activity than the M-N₄ site.[62] Shen et al. found that the Fe-N₂ site exhibited significantly higher ORR catalysis than the Fe-N₄ site due to the weak interaction of the Fe-N₂ site with the O₂^{*} and OH^{*} intermediates, which accelerated the electron transfer.[63] In addition, some studies have also suggested that the Co-N₃C₁ sites are more favorable for the ORR process compared with the Co-N₂C₂ and Co-N₄ sites. The near-Fermi electronic state of the Co-N₃C₁ structure promotes the electronic hybridization with O₂ and the protonation of the subsequently adsorbed O₂^{*} to form OOH^{*}, which is beneficial to the subsequent ORR process.[64] Overall, some of the controversies over the coordination of N have not yet reached a consensus. Therefore, further research and exploration are still needed in the future.

1.2.2.2. Transition Metal Compounds Embedded in Nitrogen-Doped Carbon

In addition to the M-N_x species, metal particles, [65] [66] metal carbides, [67] and metal nitrides [68] which are encapsulated by carbon layers, are thought to contribute to ORR activity and stability. Unlike the metal centers in the M-N_x sites, which are directly involved in the electrocatalytic process, the carbon-coated metal compounds are not in direct contact with the electrolyte, leading to different catalytic mechanisms from the M-N_x structures.

In previous study of the metal carbides, particularly Fe_3C encapsulated in carbon, has been proven to influence the outer carbon shell to enhance the ORR activity. [69] Li's group synthesized $\text{Fe}_3\text{C}/\text{C}$ catalysts by a one-step high-pressure pyrolysis method using ferrocene and cyanimide as precursors. **(Figure 1.9 (a))**The Fe_3C nanoparticles were wrapped by 4 to 9 layers of graphitic carbon and this structure exhibited great activity and stability in acidic and alkaline medium. It was believed that Fe_3C nanoparticles can catalyze ORR by activating the surrounding carbon layer without direct contact with the electrolyte.[70] Hu et al. employed ball milling and hot acid pickling to remove the carbon-coated Fe_3C particles. [67] They found a notable decline in the ORR activity after eliminating Fe_3C particles, indicating that the encapsulated Fe_3C particles play a vital role in the ORR process, even if they are not in direct contact with the electrolyte. Deng et al. reported a pod-like carbon nanotube with encapsulated iron nanoparticle (Pod-Fe) as a highly efficient ORR catalyst and elucidated the ORR active source by DFT calculations. In the **Figure 1.9 (b)**, it was showed that the electrons transferred from iron particles to carbon nanotubes lowered the local work function of the carbon surface, which could enhance the chemical activity.[71] The results indicated that the outer layer of graphitic carbon could protect and stabilize Fe_3C nanoparticles from acid etching and in return the internal core of Fe_3C nanoparticles could activate the graphitic carbon layer on the surface. This synergistic effect between the encapsulated Fe_3C nanoparticles and the graphitic carbon layer greatly enhances ORR catalytic activity and stability. And it is worth noting that the catalytic activity of the catalyst also depends on the thickness of the graphitic carbon layer outside the coated metal-containing species, which reasonably explains the

wide variations in the catalytic activity of various metal-containing species encapsulated with carbon synthesized through different methods. [72]

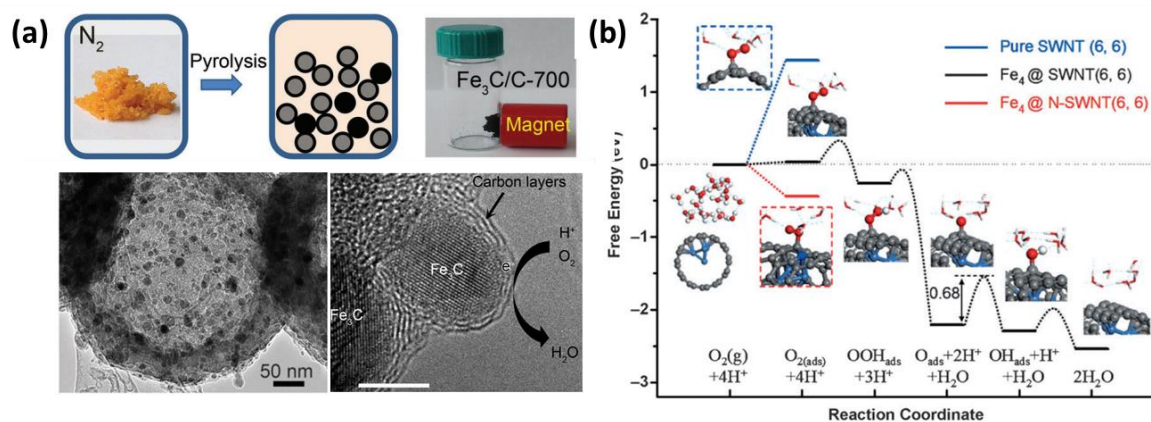


Figure 1.9 a) Synthesis and morphology of $\text{Fe}_3\text{C}/\text{C}$ hollow spheres, b) Free-energy diagram of ORR on $\text{Fe}_4@\text{SWNT}$ in water (black line) under experimental conditions. Adapted from ref. [70, 71]

Additionally, it has been reported that M-N_x sites can work synergistically with carbon-coated metal-containing species to increase the ORR activity. [73] Jiang et al. prepared a highly active Fe-N-C catalyst containing Fe-N_x sites and graphene-coated $\text{Fe}/\text{Fe}_3\text{C}$ nanocrystals ($\text{Fe}@\text{C}$) for ORR in an acidic environment. [74] The experimental results showed that the N-C structure, $\text{Fe}@\text{C}$, and Fe-N_x sites alone did not show high catalytic activity. In contrast, the Fe-N_x sites showed higher ORR activity coexisting with $\text{Fe}@\text{C}$. Subsequent DFT calculations further demonstrated that the interaction between $\text{Fe}@\text{C}$ and the Fe-N_4 site could synergistically promote the adsorption of O_2 .

Although it has been proven that carbon-coated metal species exhibit ORR activity, there is some controversy about this phenomenon. As most of the synthesis processes involved high-temperature pyrolysis, it is almost impossible to eliminate the M-N_x sites when attempting to obtain the catalyst containing only carbon-coated metal. To this end, Chen et al. adopted a novel low-temperature ($350\text{ }^\circ\text{C}$) treatment strategy with ammonium chloride, which can remove the metal-containing nanoparticles in the carbon matrix and

retain the original M-N_x site while avoiding the rearrangement of the carbon skeleton structure.[75] The study found that the contribution of carbon-coated metal-containing nanoparticles to ORR in the acidic electrolyte was negligible and the ORR activity can be enhanced to a large extent after removing these nanoparticles. As a result, they argued that the carbon-coated metal species play a "bystander" role in the ORR process. There is still controversy on the role of carbon-coated metal-containing species in the ORR process, which requires more detailed research in the future. In addition, most transition metal compounds have the problems of low electrical conductivity and lack of active sites for oxygen species. Moreover, transition metal compound in the acidic electrolyte under long operation constrains its application in acidic PEMFCs, further undermining its long-term practical prospects.

Anyway, great progress has been made in identifying and elucidating the precise chemistry of the active sites and their catalytic mechanism of ORR with the help of sophisticated in situ and ex situ characterization techniques in combination with theoretical calculations.[40] The reaction mechanism remains elusive in regards to active site formation in the heat treatment process and reaction path in the electrocatalytic ORR process, which pose a significant challenge in the rational design and synthesis of high-performance ORR catalysts.

1.3. Ionic Liquid-Derived Carbon-Based ORR Electrocatalyst

Ionic liquids (ILs) are molten salts typically containing organic cations and anions with melting points usually lower than 100 °C.[76] The coulombic interactions between the cation and anion bestow a series of excellent physical and chemical properties, such as low volatility, low toxicity, good ionic conductivity and high thermal stability, etc., which

make them potential candidates for carbonaceous precursors. In particular, most of ILs are organic salts that can tailor their structure on molecular scales and their chemical composition with specific elements.[77]

In recent years, ionic liquids have been extensively studied in the synthesis, modification and functionalization of carbon materials. Compared to conventional precursors, ionic liquids have certain advantages: First, the structure and composition of ILs are tunable so that heteroatom (e.g., N, S, P, B) can be easily incorporated into the cationic or anionic backbone before heat treatment and consequently modify the electrical conductivity, oxidation stability, and catalytic activity of the final carbon materials.[78] Secondly, the liquid form of ionic liquids facilitate carbon films or carbon coatings processing due to their good wettability with the carbons.[79] Thirdly, the cation or anion of ILs can serve as templates for generating porosity in resultant carbon materials. [80-83] These unique features make the IL-derived carbon materials highly promising for applications in electrochemical energy conversion and storage, especially as electrocatalysts for oxygen reduction reaction (ORR).

Table 1.3 Typical Cations and Anions Comprising ILs. Adapted from ref.[76]

Cation		
[C _n mim]	[C _n mpyr]	[C _n mpip]
[DEME]	[Nabcd]	[Pabcd]
[C _n dmim]	[dema]	[DBU]
Anion		
[TFSA]	[FSA]	[FTA]
[BETA]	[TSAC]	[FAP]
[TfO]	[MS]	[DFOB]
CF_3SO_3^-	CH_3SO_3^-	
[DCA]		

1.3.1. Metal-Free Carbon-Based ORR Electrocatalysts

As shown in **Figure 1.10**, the direct carbonization of ILs is one of the most straightforward approaches to synthesizing heteroatom-doped carbons. [77, 84, 85] In

2009, Dai et al. first employed imidazolium ILs as the direct precursor for synthesizing nitrogen-rich carbon materials from an inert-atmospheric pyrolysis approach.[86] As the ionic liquids are the only precursor, it is believed that nitrogen atom could be homogeneously incorporated into the carbon materials. The highly nitrogen-doped carbons derived from IL precursors are promising metal-free electrocatalysts for ORR electrocatalysis.

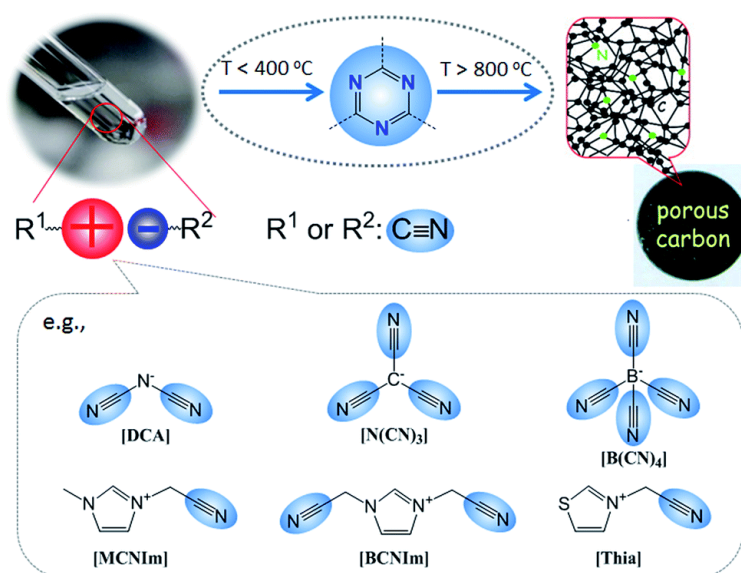


Figure 1.10 Direct synthesis of nitrogen-doped carbon from specific nitrile/cyano-containing IL precursors under ambient pressure. Adapted from ref.[77]

A number of IL-derived NDCs have exhibited excellent activity, long-term stability and great resistance to cross-over effects in ORR electrocatalysis.[87-95] Markus et al. synthesized highly mesoporous carbon materials with nitrogen contents of up to 12.0 wt% via direct carbonization of nucleobases in [emim][DCA] with the LUDOX®HS-40 as a template, and the resultant carbon materials exhibited high ORR activities and durability in the alkaline electrolyte which is comparable to commercial Pt/C catalysts. [89]

Apart from NDCs, dual- or multidoped carbons can be realized by carbonization of ILs which contain heteroatoms such as N, S, P, B, F, etc. in the cationic or anionic

backbone. [87, 93, 96, 97] Cui et al. utilized the eutectic salt mixture of KCl-ZnCl₂ and ionic liquid to prepare heteroatom (N, S) co-doped carbons with a hierarchical porous structure. The obtained catalyst material exhibited enhanced activity, long-term operational stability, and methanol tolerance compared to commercial Pt in the same alkaline environment, which was ascribed to N/S co-doping effects that enriched active site sites and boosted electron transfer.[91]

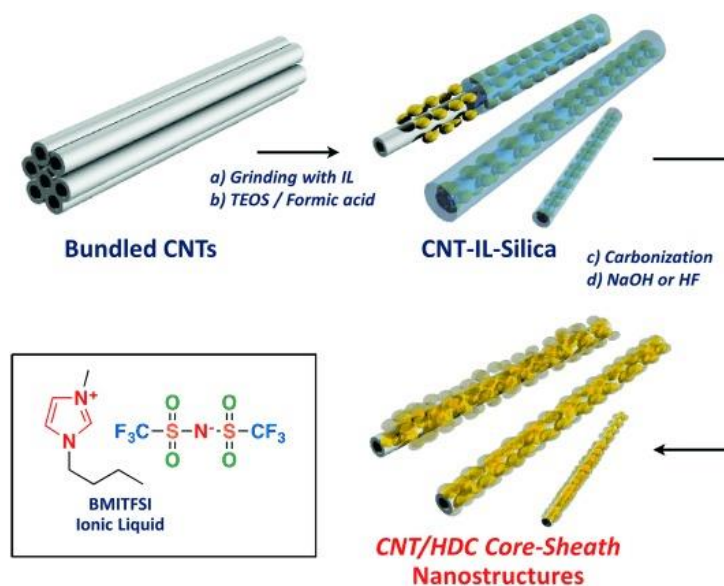


Figure 1.11 Synthesis of the CNT/HDC core–sheath nanostructures. Adapted from ref. [98]

Besides being used as carbon precursors, ILs can be surface-coating agents or N-containing dopants, which vastly reduce costs and increase utilization. The thin layer of IL-derived NDCs does not only introduce heteroatoms but also modulates the electronic structure of the carbon surface. Joo et al. developed a facile, scalable approach to prepare core-sheath nanostructured CNT/ heteroatom-doped carbon (HDC) composites selecting IL [1-butyl-3-methylimidazolium bis(trifluoromethylsulfonyl)imide (BMITFSI)] as the precursors for the hetero-atom doped shell. [98] As illustrated in **Figure 1.11**, the nitrogen, sulfur, and fluorine-containing IL (BMITFSI) can serve as heteroatom sources

to coat CNTs with the HDC sheath layer. The heteroatom-containing sheath layers significantly enhanced the catalytic performance of CNTs due to the synergistic electronic regulation with more than one heteroatom.

1.3.2. Transition Metal/Carbon-Based ORR Electrocatalysts

Ionic liquids are relatively polar solvents, ensuring reasonably good solubility of metal salts. During pyrolysis, the high content of nitrogen species in the IL-derived carbon provide a number of anchor sites to capture/trap transitional metals such as Fe, Co, Ni, etc., to form the M-N_x sites which is highly active for ORR. [57, 99, 100] In addition, the electronic interaction between metal species and nitrogen-doped support imparts the electrocatalyst materials with diverse active species, abundant active sites, improved conductivity, and higher corrosion-resistance during the electrochemical reactions.[101-106] Generally, there are two main ways to obtain these types of metal-containing catalysts: the carbonization of task-specific ILs containing metal ions in the cations [107] or anions [108] ; the other is the carbonization of ILs with metal-containing precursors. [109] As shown in **Figure 1.12**, Kim prepared a series of nitrogen-doped carbon materials containing different transition metals by pyrolysis of ionic liquids (i.e., 1-ethyl-3-methylimidazolium dicyanamide (C₈H₁₁N₅, [emim][DCA]) with metal salts and correlated the ORR activity of these catalysts with the nitrogen-doped structure and sp² degree of carbon network. [110] Other than single transition metals, multiple transition metals could be incorporated simultaneously, leading to other form of metal species such as alloys. Especially the Fe-based carbons alloyed with Co, Ni has been proven effective to compensate the adverse effect of hydroxyl oxidation by enhancing conductivity and protecting Fe sites.[111, 112] The ionic liquid strategy has great potential in the

preparation of multiple metal co-doping, taking advantage of the solvent capability of ILs .[113]

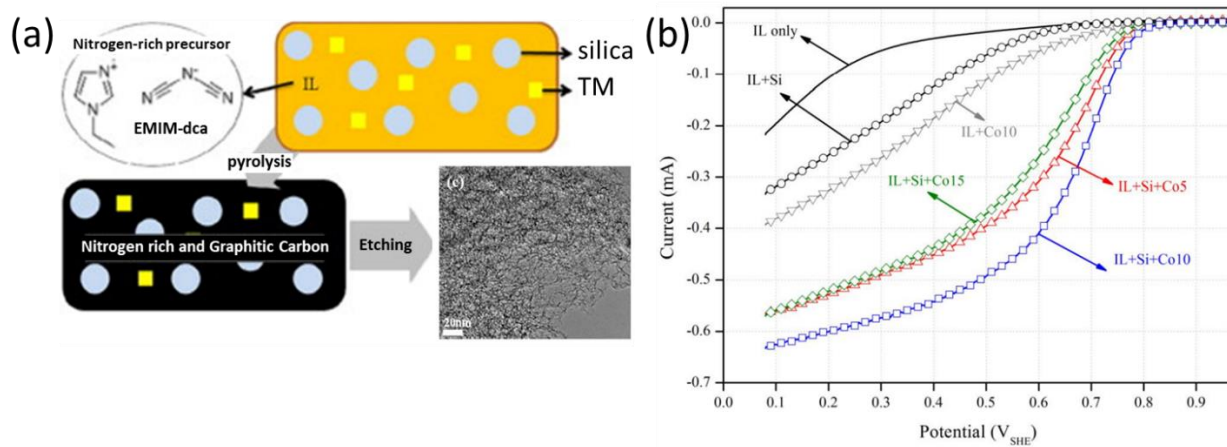


Figure 1.12 a) Nitrogen-doped carbon catalysts derived from ionic liquids in the presence of transition metals for the oxygen reduction reaction, b) Polarization curves for oxygen reduction on the nitrogen-doped carbon catalysts with different Co contents. Adapted from ref. [110]

1.3.3. Porous Structure Engineering

The microstructures of carbon materials play crucial and decisive roles in the surface-related electrocatalytic processes such as ORR. Different nanostructured IL-derived nitrogen-doped carbon materials such as spheres,[114] nanobubbles,[115] graphene,[116] nanosheets,[88] have been exploited in order to improve the ORR performance. Among them, porous structures attract great attentions since hierarchical porosity enables efficient mass transport and diffusion of intermediates, and a large amount of accessible active sites for electrocatalysis.

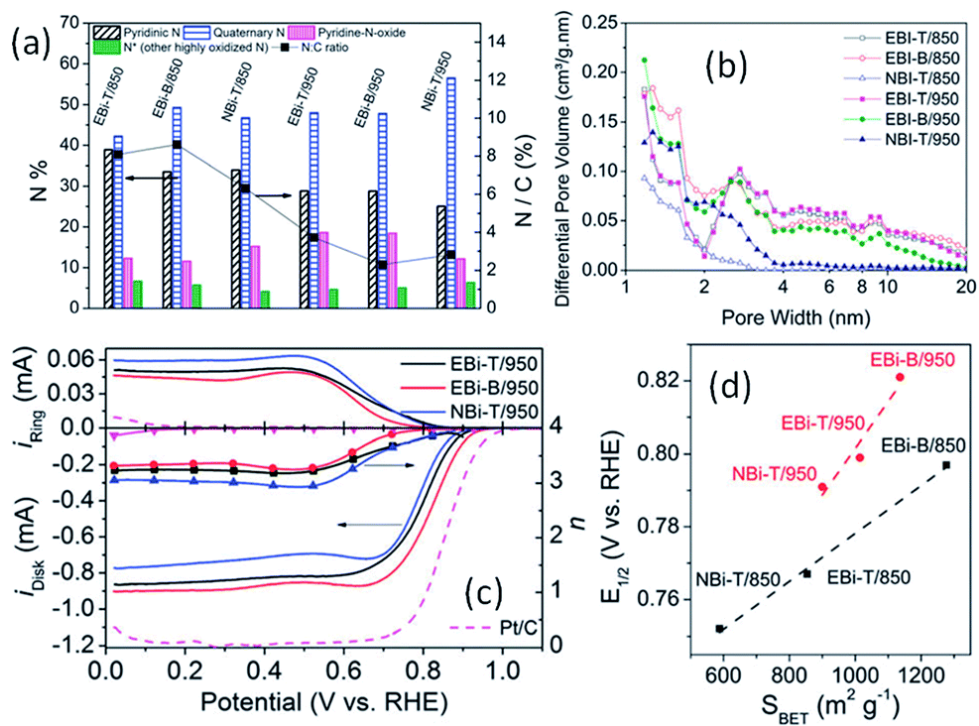


Figure 1.13 a) Nitrogen composition and (b) pore size distribution of different carbons derived from ILs containing a bis[N-(2-cyanoethyl)]imidazole core. (c) Disk (lower part) and ring current (upper part), and number of transferred electrons (n , symbol line) of IL-derived carbon catalysts. (d) Correlation between the half-wave potentials ($E_{1/2}$) and surface areas (S_{BET}) of different carbons. Adapted from ref. [77] [90]

Zhang et al. studied the effects of pore sizes distributions of carbon materials on the ORR kinetics with a series of nitrogen-doped carbons derived from a specific ILs comprised of a bis[N-(2-cyanoethyl)]imidazole core and bulky anions.[90] As shown in **Figure 1.13**, the nitrogen contents in the obtained catalysts were correlated with the calcination temperature. Furthermore, the resultant carbons possessed different types of porosity (i.e., micro- and/or mesopores) depending on the IL structure and their surface areas ranging from 588 to 1277 m² g⁻¹. The half-wave potentials ($E_{1/2}$) increase monotonically with the surface areas, indicating the crucial role of the porous structure in ORR kinetics.

There are two main strategies to build up the porous structures for IL-derived carbons: direct synthesis and template methods.

1.3.3.1. Direct Synthesis

It was found that well-designed anions and cations in the ionic liquid can act as self-porogen for mesoporous carbons. Previous work revealed that the carbonization of [N(Tf)₂]-containing IL yields higher surface areas than chloride.[86] For an example, the specific surface area of porous carbon derived from [MCNIm][Tf₂N] can be as high as 780.6 m²/g.[117] ILs contain anions such as [C(CN)₃]⁻ and [B(CN)₄]⁻ are more likely to form 2D- or 3D-connected carbon frameworks at elevated temperatures (**Figure 1.14**). Cations also have an impact on the surface areas such that long-chain imidazolium cations are more effective in promoting surface areas than the [emim]⁺ cation.[118] However, the mechanism for the generation of porosity on a molecular scale remains elusive.[119]

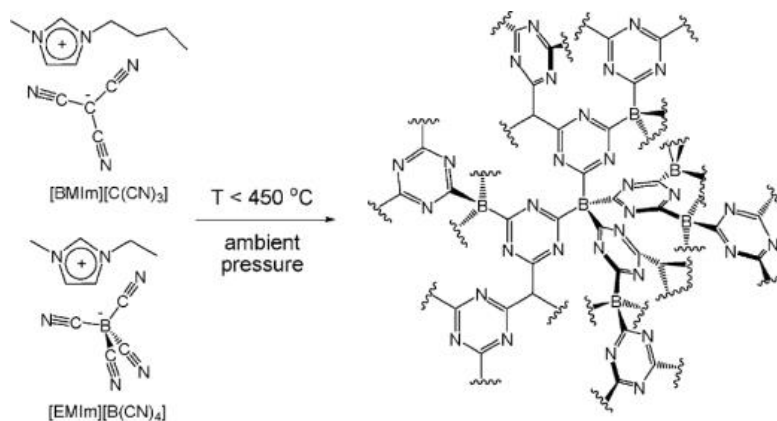


Figure 1.14 Carbon materials derived from ionic liquids containing anions of [C(CN)₃]⁻ and [B(CN)₄]⁻. Adapted from ref. [118]

1.3.3.2. Template Methods

Hard templates are solid compounds with pores or high surface areas, such as zeolites, mesoporous silica, and colloidal particles, and can be used to tailor the porosity of carbons from ILs.[119] Silica templates have great advantages of flexibility in shapes

which can be adopted directly into the morphology of carbons, as well as the ability to immobilize ionic liquids.[120] For example, Yang et al. developed a silica template method in the carbonization of [C₂mim][DCA] and produced mesoporous NDCs with large surface areas of up to 1553 m² g⁻¹. [89] Chen et al. took the advantage of the interaction of ionic liquids with silica spheres to prepare a series of nitrogen-doped hollow carbon spheres with uniform and tunable morphology. [121]

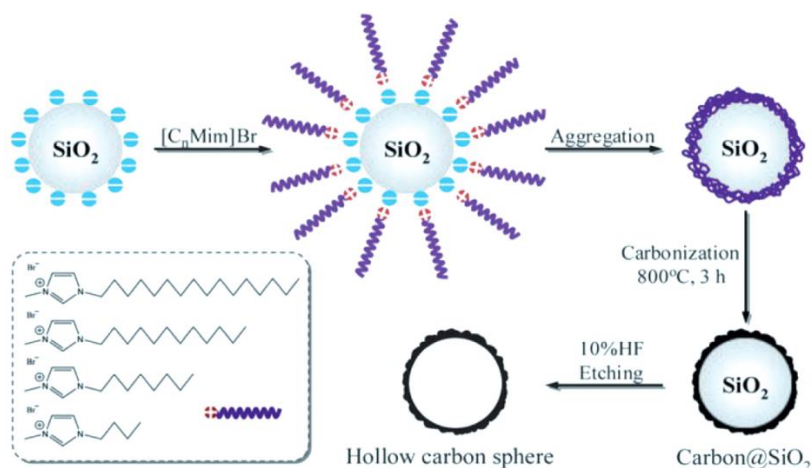


Figure 1.15 Hollow carbon spheres prepared by the carbonization of ionic liquids coated on silica microspheres. Adapted from ref. [121]

Although silica is a strong example of template, the removal of the silica templates requires the harsh cleansing with strong acid and alkali, such as the toxic HF acid. Eutectic salt mixtures are good candidates to replace silica which can be easily removed, simplifying the templating process. As shown in Figure 1.16, It was found the ionic liquid carbonization with eutectic salt mixture of NaCl/ZnCl₂ (denoted as NZ) as the template resulted in optimized pore transport system in the ionic liquid-derived carbons, resulting in favorably high electrocatalytic performance in oxygen reduction under alkaline and acidic conditions.[122]

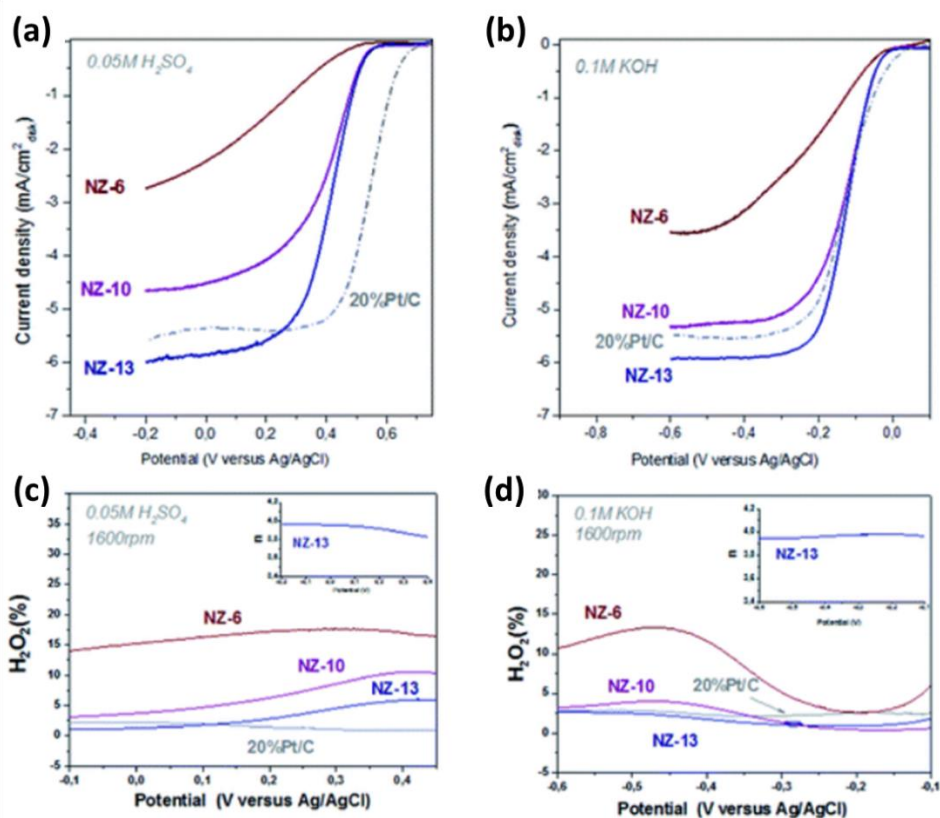


Figure 1.16 Electrocatalytic activity of NC-NZ catalysts: (a) ORR polarization curves in O₂ saturated 0.05 M H₂SO₄; (b) ORR polarization curves in O₂ saturated 0.1 M KOH; (c) and (d) hydrogen peroxide yield plots obtained in O₂ saturated 0.05 M H₂SO₄ and 0.1 M KOH, respectively. Inserts – electron transferred number of NC-NZ-13 at different potentials determined from the corresponding RRDE data. Adapted from ref. [122]

1.4. Motivation and Scope of This Thesis

In response to the energy crisis and environmental issues, clean energy conversion technologies such as fuel cells and metal-air batteries have attracted extensive attention. However, the noble metal-based ORR catalysts used in these technologies hinder their comprehensive implementation. Carbon-based catalysts have been regarded as promising alternatives to noble metals. Various strategies have been proposed to improve the activity and stability of carbon-based catalysts, such as doping heteroatoms, building highly active sites (M-N_x, etc.), and constructing porous microstructures. Ionic liquids can

be efficient carbonaceous precursors to harness the strategy mentioned above in preparing carbon-based catalysts, with the advantage of low volatility, high solubility, and tunable composition, which greatly simplify processing. However, it remains a significant challenge to control the fine microstructures during ionic liquid pyrolysis, which is crucial to the catalytic performances. Therefore, carbon-based electrocatalysts with different microstructures were prepared from an ionic liquids strategy to better understand this method. The fundamentals of ORR catalysts and endeavors to enhance the activity and stability of the catalysts was summarized in **Chapter 1**. Also, the advantages of the ionic liquid and state-of-art ionic liquid-derived carbon-based catalysts were introduced. The physicochemical characterization methods and the electrochemical measurements used for evaluating the ORR performances will be discussed in **Chapter 2**. And In **Chapter 3**, N-CNTs composite prepared from [emim][DCA] with the assistance of silica templates will be presented. The effects of silica template on the formation of N-CNTs, as well as the composition and morphology, were studied. Moreover, the correlation between the obtained N-CNTs catalysts and ORR catalytic activity were also investigated to gain further insights into the structure–property correlation. In **Chapter 4**, FeCo alloy nanoparticles coupled NC with a core-shell structure were prepared from [emim][DCA]/metal salts. The benefits of the core-shell structure were studied regarding the improved bifunctional catalytic activity (ORR and OER) and stability. And the performances of the obtained bifunctional electrocatalysts in the rechargeable Zn-air battery were displayed.

Chapter 2

2. Characterization Methods

2.1. Physicochemical Characterization

(1) Scanning Electron Microscope (FESEM)

In this paper, the SEM (model JSM-7100F) was used to obtain the topographical and elemental information at magnifications of 10x to 300,000x. Test sample preparation method: take a small amount of catalyst sample powder and paste it directly on the conductive glue on the copper plate for testing.

(2) Transmission Electron Microscope (TEM)

TEM is mainly aimed at the observation of the morphology, internal structure and crystal defects of solid materials. In this paper, TEM and high-resolution TEM (HR-TEM) images were collected on a Tecnai G2 F30 (FEI, American) electron microscope with an acceleration voltage of 200 kV.

(3) X-Ray Diffraction

The crystal structure and phase of the samples were analyzed with XRD patterns. The XRD patterns were collected by an Empyrean X-ray diffractometer (PANalytical,

Holland) using Cu K α radiation with a wavelength $\lambda = 1.540598 \text{ \AA}/1.54184 \text{ \AA}$, in the 2θ range between 10° and 90° at a scan speed of 5° min^{-1} .

(4) X-Ray Photoelectron Spectroscopy (XPS)

XPS can identify the chemical composition, chemical valence state and content of each element of a few atomic layers on the solid surface (i.e., the surface layer of tens of angstroms). In the experiment, XPS was performed on an ESCALAB 250XI (Thermo, American) X-ray photoelectron spectrometer with a monochromatized aluminum source Al K α ($E = 1486.6 \text{ eV}$), and then Avantage software was used for peak fitting and data analysis.

(5) CHON analysis

The contents of C, H, O, N element were measured with CHNO Vario EL cube (Elementar, Germany) instrument using the combustion method. The samples were sealed and combusted in a pure oxygen atmosphere and were analyzed by TCD (thermal conductivity detection) analysis with respect to emitted gaseous NO $_2$, CO $_2$ and H $_2$ O.

(6) Raman Spectroscopy (Raman)

Raman is based on the Raman scattering effect, and provides molecular vibration and rotation information by analyzing the scattering spectrum with different frequencies from the incident light which gives information about the molecular structure, chemical bonds, etc. Raman spectroscopy is one of the most commonly used and effective means to analyze the structural and electronic structure information of carbon materials. In this paper, the Raman spectra were collected by Renishaw Raman microscope (InVia) using an excitation wavelength of 633 nm, in the spectral range $500 - 3200 \text{ cm}^{-1}$.

(7) Inductively Coupled Plasma Optical Emission Spectrometer (ICP-OES)

ICP-OES is a spectroscopic analysis method using inductively coupled plasma as the excitation light source, with high accuracy, precision, and low detection limit. It has the advantages of rapid determination, wide linear range, and simultaneous determination of multiple elements. In this paper, ICP-OES (Prodigy7 model, LEEMAN LABS) was used to test the metal content in catalyst samples.

(8) Multi-point specific surface area test

Brunauer-Emmett-Teller (BET) method based on the N₂ adsorption–desorption isotherms were used with the Belsorp-max (MicrotracBEL, Japan) analysis instrument to assess the specific surface area and particle size of the materials. The samples were first heated under vacuum at 350 °C for 5 h, and high-purity N₂ was used as the adsorption-desorption gas.

(9) Thermogravimetric Analyzer

Synchronous thermal analyzers study mass (Thermogravimetric analysis (TGA)) and heat (differential scanning calorimetry (DSC)) changes caused by chemical reactions and physical changes during the temperature control process of the sample under exactly the same test conditions. It can determine the thermal decomposition temperature and content, phase transition temperature and phase change enthalpy of the substance, determine the composition of the material, reaction stage and reaction kinetics, etc. In this paper, synchronous thermal analyzer (STA449F3 model, NETZSCH, Germany) was used under consistent gas flow (O₂ or Ar on demand) and heat rate of 10 °C/min.

2.2. Electrocatalytic Measurements

2.2.1. Preparation of Working Electrode

To prepare the catalyst ink, 10 mg of the as-prepared catalyst were dispersed in a mixture solvent of 450 μL deionized water, 500 μL ethanol and 50 μL of 5 wt% Nafion (DE 521, DuPont). The mixture suspension was sonicated for at least 30 minutes to ensure the homogenous dispersion of catalyst ink. The working electrode was prepared by dripping catalyst ink onto the glassy carbon electrode and dried naturally in the air. The catalyst mass loading was estimated as 0.5 $\text{mg}\cdot\text{cm}^{-2}$ for ORR and 0.4 $\text{mg}\cdot\text{cm}^{-2}$ for OER, respectively.

2.2.2. ORR Measurement

The catalytic activity of ORR catalysts can be investigated by single-cell and half-cell tests. The single-cell test can reflect the overall performance of catalysts in a practical fuel cell system. And the half-cell test is fast and convenient for examining the catalysts' quality before being applied to practical devices.

Generally, half-cell testing is performed in a three-electrode system with an electrochemical workstation (**Figure 2.1**). In the three-electrode system, the working electrode is a rotating disk electrode (RDE) or a rotating ring disk electrode (RRDE) loaded with a certain amount of catalyst; the counter electrodes are platinum wire or graphite; the reference electrode is usually a normal hydrogen electrode (NHE). Other commercial reference electrodes such as Ag/AgCl and saturated calomel (Hg/HgO) electrodes are also used for experimental convenience. In a typical half-cell test, the three electrodes are placed in a four-port electrolytic cell filled with electrolytes, usually 0.1 M KOH solution, 0.1 M of HClO₄ solution, or 0.5 M of H₂SO₄ solution.

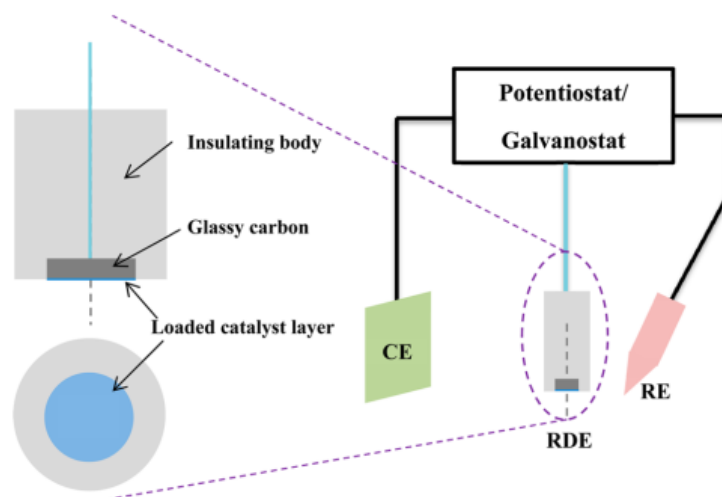


Figure 2.1 Schematic diagram of typical rotating-disk electrode (RDE) testing setup in three-electrode configuration. Adapted from ref. [123]

Linear sweep voltammetry (LSV) is performed by immersing the three electrodes in an oxygen-saturated electrolyte at room temperature with the RDE speed of 1600 rpm and a sweep rate of 10 mV/s. The scanning range in alkaline solution is 0.2 ~ -1.0V, and the scanning range in acidic solution is 0.9 ~ -0.2 V. After the scanning is completed, the curve segment swept from high potential to low potential is taken as the ORR polarization curve. As illustrated in **Figure 2.2**, a series of important parameters about the catalytic activity can be attained, including the onset potential (E_{onset}), half-wave potential ($E_{1/2}$), diffusion-limiting current density (j_L), overpotential under a specific current density (η_j), etc. The E_{onset} refers to the overpotential when the current density reaches 5% j_L , indicating the intrinsic activity of the catalyst. The $E_{1/2}$ refers to the overpotential when the current density reaches 50% j_L . Furthermore, the j_L reflects the mass transfer efficiency in the catalyst and has a theoretical value of 6 mA cm⁻² at 1600 rpm. In a standard test, the larger values of these three parameters suggest better ORR activity of the measured catalyst. [124] Cyclic voltammetry curves in nitrogen-saturated and oxygen-saturated

electrolytes at zero rotational speed were also used to evaluate the ORR catalytic performance of the catalysts.

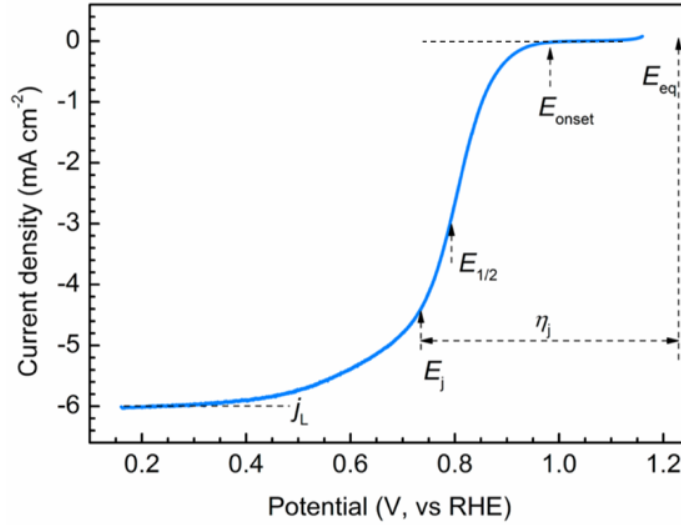


Figure 2.2 The ORR polarization curve collected from RDE in O₂-saturated electrolyte. Adapted with permission from respective publisher. Adapted from ref. [123]

The ORR polarization curves at different rotational speeds can also be used to study the kinetics of electrocatalytic reactions. The kinetic current density and the number of transferred electrons can be obtained based on the Koutecky-Levich equation, which is calculated as follows:

$$j^{-1} = j_L^{-1} + j_K^{-1} = (B\omega^{1/2})^{-1} + j_K^{-1} \quad (1-1)$$

$$B = 0.62n_eFC_0(D_0)^{2/3}\nu^{1/6} \quad (1-2)$$

$$j_K = n_eFkC_0 \quad (1-3)$$

In Equation 1-1, j is the measured current density, j_L is the diffusion-limiting current density, and j_K is the kinetic current density. In Equation 1-2, n_e is the number of transferred electrons, F is the Faraday constant ($F=96485 \text{ C mol}^{-1}$), C_0 is the saturated concentration of oxygen in the reaction solution (in acidic conditions (0.1 M HClO₄): $1.26 \times 10^{-3} \text{ mol L}^{-1}$, in alkaline conditions (0.1 M KOH): $1.2 \times 10^{-3} \text{ mol L}^{-1}$). And D_0 is the

diffusion coefficient of O₂ in the electrolyte (in acidic conditions (0.1 M HClO₄): 1.93 × 10⁻⁵ cm² s⁻¹, in alkaline conditions: 1.9 × 10⁻⁵ cm² s⁻¹). ν is the kinematic viscosity of the electrolyte (in both acid and alkali conditions: 1.0×10⁻² cm² s⁻¹); ω is the angular velocity of the working electrode rotation ($\omega = 2\pi\nu$, ν is the linear velocity). In Equation 1-3, k is the electron transfer rate constant. The number of transfer electrons in oxygen reduction can be calculated from the Koutecky-Levich equations (1-1) and (1-2). [124]

The rotating ring-disk electrode (RRDE) technique which has a coaxial ring electrode can be used to collect the disc current (I_d) generated by the ORR process and the ring current (I_r) generated by the H₂O₂ decomposition process. The H₂O₂ yield (H₂O₂%) can be calculated using the fraction of I_d and I_r and the corresponding electron transfer numbers (n) during ORR, as follows:

$$H_2O_2\% = 200 \times \frac{\frac{I_r}{N}}{\frac{I_r}{N} + I_d} \quad (1-4)$$

$$n = \frac{4I_d}{I_d + \frac{I_r}{N}} \quad (1-5)$$

, where N is the collection efficiency of the Pt ring electrode ranging from 0.24-0.5. The collection efficiency was 37%, giving the parameters (Ring-Disk Gap = 320 μm; Disk outer diameter = 5.61 mm; Ring outer diameter = 7.92 mm; Ring inner diameter = 6.25 mm)

The Tafel slope is an important indicator reflecting the kinetics of ORR catalytic reaction. The value of Tafel slope can be obtained based on the Tafel equation (which is conducted from the Butler-Volmer formula):

$$\eta_a = (RT/nF\alpha_a)\ln j - (RT/nF\alpha_c)\ln j_0 = b\ln j - a \quad (1-6)$$

$$\eta_c = (RT/nF\alpha_c)\ln j_0 - (RT/nF\alpha_a)\ln j = a - b\ln j \quad (1-7)$$

Where R is the gas constant, T is the temperature (Kelvin), n is the number of transfer electrons, F is the Faraday constant, α_c is the cathodic charge transfer coefficient, α_a is the anodic charge transfer coefficient, j_0 is the exchange current density as the current density in both the cathodic and anodic directions at the equilibrium potential. The b is the Tafel slope.

2.2.3. Catalyst Stability Test

Two methods can be used to test the stability of the catalysts: (1) Amperometric i-t: the catalyst is kept at a certain potential and tested in a saturated oxygen solution with RDE rate of 1600 rpm, lasting 10 hrs. The ratio of the current after 10 hours to the initial current is the indicator of the stability of ORR; (2) Cyclic voltammetry acceleration method: The catalyst is repeatedly scanned within a certain potential range, and the ORR plan curve before and after scanning is measured. The stability was determined by the half-wave potential difference (ΔE) value of the ORR planning curve before and after scanning.

2.2.4. Catalyst Anti-poisoning Test

A good catalyst not only requires good activity and stability, but also should have excellent anti-poisoning ability. In this thesis, the resistance to methanol of the catalysts was tested. Chronoamperometry was used: the catalyst was kept at a certain potential, and the saturated oxygen solution was rotated at 1600 rpm. When the catalyst current was stable (about 100 s), methanol (1 M CH₃OH) was added, and the ratio of the current to the initial current value was calculated after 200 s. The higher the ratio, the better the anti-poisoning ability of the catalyst.

2.2.5. OER Measurement

Cyclic voltammetry (CV) tests were performed in 1 M KOH electrolyte until steady state under sustained O_2 to guarantee the O_2/H_2O equilibrium at 1.23 V vs. RHE at a scan rate of $10 \text{ mV}\cdot\text{s}^{-1}$. Then linear sweep voltammetry (LSV) were performed in 1 M KOH electrolyte at a scanning rate $5 \text{ mV}\cdot\text{s}^{-1}$ to obtain the polarization curves. Electrochemical impedance spectroscopy (EIS) was attained by applying an AC voltage with 5 mV amplitude in a frequency range from 10^5 to 0.01Hz and recorded at 1.55 V vs. RHE in the same conditions.

The double layer capacitance (C_{dl}) was obtained by recording the cyclic voltammetry curves within the nonreactive region, with the scan rate from 20 to $120 \text{ mV}\cdot\text{s}^{-1}$. The C_{dl} was calculated on the basis of the formula ($C_{dl} = \Delta J/2v$, ΔJ means the current density difference while the v represents the scan rate).

Electrochemical specific surface area (ECSA) was calculated according to the formula: $ECSA = C_{dl}/C_s$, where C_s signifies the specific capacitance for an ideal flat surface (real surface area is 1 cm^2). Here we adopt a general value of $60 \mu\text{F}\cdot\text{cm}^{-2}$ for C_s .

2.3. Zn-Air Batteries Assembly and Measurements

In a typical rechargeable battery, the zinc plate was polished as the anode, carbon paper ($1 \text{ cm} \times 1 \text{ cm}$) with gas diffusion layer (GDL) was coated with electrocatalyst on the reverse side as the cathode (loading mass is $1 \text{ mg}/\text{cm}^2$). The 6.0 M KOH and 0.2 M Zn (Ac)₂ solution was saturated with oxygen as the electrolyte.

In an all-solid-state Zn–air battery, the zinc foil with the 0.05 mm thickness was used as anode. The gel polymer electrolyte was prepared in the following process. The 45 ml solution containing 0.1M KOH and 0.02M Zn (Ac)₂ was stirred for 30 min under ambient

temperature until the homogeneous opaque lotion was obtained. Then polyvinyl alcohol (PVA, 4.5g) was added at 95 °C to form a homogeneous viscous solution, followed by casting on a watchglass with a diameter of 20 cm to form a thin polymer film (thickness about 1 mm). The film was then frozen in a freezer at -20 °C for about 2-4 h. Before use, the film was thawed and dried in an air-dry oven at 60°C. To assemble the all-solid-state Zn-air battery, PVA film was coated with the as-prepared catalysts and zinc foil was placed on the reverse side. Ni foam was pressed as the current collector on the catalyst side. At last, the components were firmly pressed together by roll-pressing.

All Zn-air batteries were evaluated under ambient conditions.

The specific capacity was calculated according the equation below:

current * service hours / weight of consumed zinc

The corresponding energy density was determined according to the equation below:

current * service hours * average discharge voltage / weight of consumed zinc

Chapter 3

3. Template-Promoted Synthesis of Nitrogen-Doped CNTs from Ionic Liquid for Enhanced ORR Activity

Abstract: Nitrogen-doped carbon nanotubes (N-CNTs) attract significant attention as oxygen reduction reaction (ORR) electrocatalysts due to their exceptional electronic, mechanical, and structural properties. However, high energy dissipation and complex synthetic process impede the actual applications of the N-CNTs. Herein, we propose a facile strategy to prepare the N-CNTs composites through an ionic liquid with the assistance of silica template. Using silica/(FeCo)/[emim] [DCA] as an example, we demonstrate that the presence of silica template promotes the growth of N-CNTs during the one-pot pyrolysis by preventing the face-to-face carbon stacking and downsizing the metal-catalysts particles. With structural and chemical characterizations, it was found that the template effects of silica led to high specific area and nitrogen doping which enhanced the ORR electrocatalytic activity in alkali conditions. This facile synthetic strategy is envisioned to pave a new pathway to N-CNTs materials synthesis in energy fields.

3.1. Introduction

The oxygen reduction reaction (ORR) is of paramount importance for new-generation energy conversion technologies such as fuel cells and metal-air batteries.[125, 126] Currently, most of the ORR catalysts in practice are platinum-based, subjected to inflated prices, low reserves, and poor stability.[127] Therefore, many efforts have been made to develop low-cost and highly efficient ORR catalyst substitutes for Platinum. In this scenario, nitrogen-doped carbon nanotubes (N-CNTs) have attracted enormous attention due to their exceptional electronic, mechanical, and structural properties.[128] Inherently, carbon nanotubes (CNTs) possess excellent electrical conductivity, large specific surface area, superb thermal and mechanical properties, etc. Moreover, nitrogen doping in the carbon skeleton has been demonstrated as an effective route to modulate the chemisorption energy of O_2 intermediates, improving the ORR efficiency to a great extent.[16]

Generally, N-CNTs can be prepared through either in-situ doping techniques such as chemical vapor deposition (CVD),[129] arc-discharge, laser ablation, and chemically solvothermal procedures (ca. 230–300 °C), or post-treatment doping with toxic N precursors (NH_3 , HNO_3 , and pyridine) under high temperature (above 800 °C).[130] However, these methods require harsh synthetic conditions and high energy dissipation that impede the broad application of N-CNTs. Among various techniques, direct pyrolysis of carbon precursor with metal catalysts (Fe, Co, Ni, etc.), which is relatively facile and cheap, has been deemed a promising pathway to synthesize N-CNTs. In direct pyrolysis preparation, the choice of carbon precursor is vital since it greatly influences the formation, morphology, and properties of N-CNTs.[131] Mai et al. exploited different MOFs to

prepare a series of N-CNTs. It was found that the obtained N-CNTs assembled into various nano-architectures and present distinct oxygen reduction activity depending on the corresponding MOF precursors.[132] Though these advances, employing ionic liquids as the precursor to synthesize N-CNTs have rarely been reported.

For some unique properties, ionic liquids (ILs) have attracted extensive attention as ideal carbonaceous precursors to synthesize porous carbon materials for application in ORR electrocatalysis.[76, 81-83, 133] ILs are molten salts containing organic cations and anions with melting points usually lower than 100 °C. [85] They are in the liquid states featured with low volatility, low toxicity, good solvent capacity, high thermal stability, etc., making them flexible in processing and calcination.[77] Most ILs can be tailored on the molecular scale with various heteroatoms (e.g., N, S, P, B), which offers the potential to regulate the electrical conductivity, oxidation stability, and ORR catalytic activity of the final carbon materials.[90] In addition, previous research has shown that the cation or anion of ILs can serve as self-porogen to promote the formation of porosity in carbon materials which would facilitate the mass transfer in the ORR process.[114] Different nanostructured IL-derived nitrogen-doped carbon materials such as spheres,[84] nanobubbles,[116] graphene,[134] nanosheets,[135] have been reported as efficient ORR electrocatalysts, yet the N-CNTs derived from the direct pyrolysis of ILs have hardly been investigated.

Herein, we have designed a template-assisted strategy to synthesize N-CNTs by direct carbonization of ILs under the catalysis of FeCo alloy nanoparticles. An imidazolium IL, 1-ethyl-3-methylimidazolium dicyanamide ([emim][DCA]), has been chosen as the nitrogen-doped carbon precursor because of its remarkably high nitrogen content. And

iron and cobalt salts have been used as FeCo alloy catalysts precursors in the carbonization process to promote the graphitization of carbon products. The dicyanamide anions can act as the metal-ligands to form dicyanamido-metallate, enabling the homogeneous dispersion of metal ions in the IL-precursor.[136] During the pyrolysis process, iron and cobalt ions are annealed into FeCo alloy nanoparticles under the reducing atmosphere of the carbothermal reaction; these FeCo alloy nanoparticles then catalyze the growth of N-CNTs from the volatile product of IL with the presence of silica template. [137] Our work has demonstrated that the silica template significantly impacts the formation of N-CNTs, as well as the composition and morphology of final catalysts. Moreover, the correlation between the obtained N-CNTs catalysts and ORR catalytic activity has also been investigated to gain further insights into the structure–property correlation.

3.2. Experimental Section

Cobalt (II) chloride hexahydrate ($\text{CoCl}_2 \cdot 6\text{H}_2\text{O}$, 99%, Shanghai Aladdin Biochemical Technology Co. Ltd), iron (III) chloride anhydrous (FeCl_3 , 99%, Shanghai Aladdin Biochemical Technology Co. Ltd), and 1-ethyl-3-methylimidazolium dicyanamide ([emim] [DCA], Sigma) were used as purchased without any further treatment. The $\text{CoCl}_2 \cdot 6\text{H}_2\text{O}$ and 0.5 mmol FeCl_3 were ultrasonic dissolved in [emim] [DCA] separately and then blended. The molar ratio of FeCl_3 , CoCl_2 , and [emim] [DCA] was fixed at 1000:1:1. Then, the silica nanospheres with a mean diameter of 30 nm were added into the mixture solution. And the mass ratio of silica nanoparticles varied from 0, 0.5, and 1. The mixture solution was transferred to an alumina crucible and annealed for two hours at 900 °C in an H_2/Ar atmosphere (5% H_2 and 95% Ar) at a heating rate of 10 °C/min. After natural

cooling to room temperature, the obtained carbon composites were noted as $\text{FeCo}(\text{SiO}_2)_x\text{-T}$, where x is the weight ratio of the silica and T is the calcination temperature. The $\text{FeCo}(\text{SiO}_2)_x\text{-T}$ samples were subsequently washed with 20 wt% hydrofluoric acid (HF) to remove the silica template. And the final materials were noted as $\text{FeCo}(\text{SiO}_2)_x\text{-T-HF}$, which applied in ORR electrocatalysis in this work.

3.3. Results and Discussion

3.3.1. N-CNTs Formation Mechanism

There are only two steps for the catalyst preparation: blending and pyrolyzing. As the dicyanamide anions are ligands characterized as strong Lewis bases with electron donor solvent properties, iron and cobalt ions can be separated and dispersed in the IL to form a homogeneous solution.[136] Then, silica nanospheres with a mean diameter of 30 nm were added to the mixture solution. The molar ratio of FeCl_3 , CoCl_2 , and $[\text{emim}][\text{DCA}]$ is fixed at 1000:1:1. The mass ratio of silica nanoparticles was varied from 0, 0.5, and 1 for investigating the silica template effect.

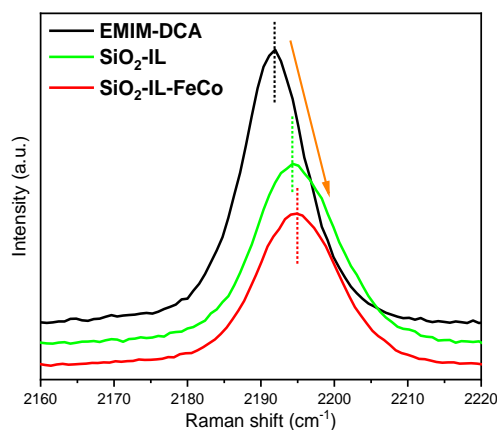


Figure 3.1 Raman spectra of $[\text{emim}][\text{DCA}]$ with SiO_2

As shown in the Raman spectra (**Figure 3.1**), the strong interaction between the negatively charged anions and polar hydroxy groups on the surface of SiO_2 nanoparticles

was evidenced by a blue shift from 2191 to 2194 cm^{-1} with the $\text{C}\equiv\text{N}$ stretching band.[138] As a result of the combined interaction, the mixture precursor formed a homogeneous gel. Then the gel-like precursors were heated to 900 °C under an H_2/Ar atmosphere.

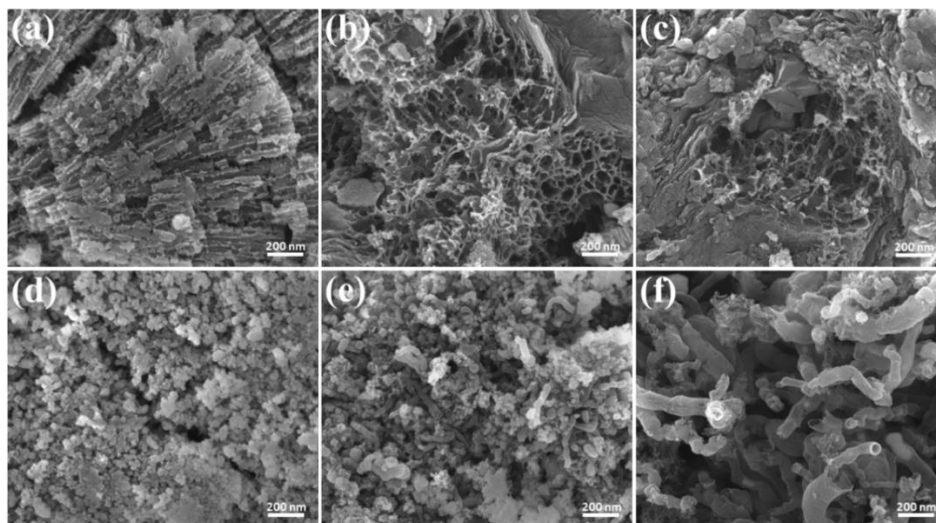


Figure 3.2 SEM images of the pyrolysis products at different calcination stages. (a) $\text{FeCo}(\text{SiO}_2)_0-500$, (b) $\text{FeCo}(\text{SiO}_2)_0-700$, (c) $\text{FeCo}(\text{SiO}_2)_0-900$, (d) $\text{FeCo}(\text{SiO}_2)_{0.5}-900$, (e) $\text{FeCo}(\text{SiO}_2)_{0.5}-900$, (f) $\text{FeCo}(\text{SiO}_2)_{0.5}-900$.

In order to investigate the carbonization of ionic liquid in the presence of silica templates during pyrolysis, the morphology of intermediate pyrolysis products at different calcination stages were analyzed with SEM. As shown in **Figure 3.2**, the distinct morphology between $\text{FeCo}(\text{SiO}_2)_0-900$ and $\text{FeCo}(\text{SiO}_2)_{0.5}-900$ sample implied the significant template effects of silica nanoparticles. Specifically, the tubular structures in the $\text{FeCo}(\text{SiO}_2)_{0.5}-900$ sample were not observed in the $\text{FeCo}(\text{SiO}_2)_0-900$ sample. **Figure 3.2 (a) - (c)** displayed that the precursors in the silica-free samples ($\text{FeCo}(\text{SiO}_2)_0\text{-T}$) transformed to the stacked lamellar structures at 500 °C. Then the lamellar structure evolved into a cellular network of carbon sheets at 700 °C. When the calcination temperature was increased to 900 °C, the cellular network collapsed along with the further decomposition of the intermediate carbons. However, the silica nanoparticles directed the

morphology transformation in the $\text{FeCo}(\text{SiO}_2)_{0.5}\text{-T}$ samples. As shown in **Figure 3.2 (d) - (f)**, unlike the lamellar structures in silica-free samples, the $\text{FeCo}(\text{SiO}_2)_{0.5}\text{-T}$ samples preserved the granular shape of silica and presented a porous bulk packed with granules in a semi-carbonized state at 500 °C, indicating the in-situ carbonization of ionic liquids on the surface of silica particles. Subsequently, further decomposition of the semi-carbonized intermediates left plenty of voids, and the preliminary tubular structure came into shape at 700 °C. Finally, most carbonaceous substance has transformed into bamboo-like tubular structured materials at 900 °C.

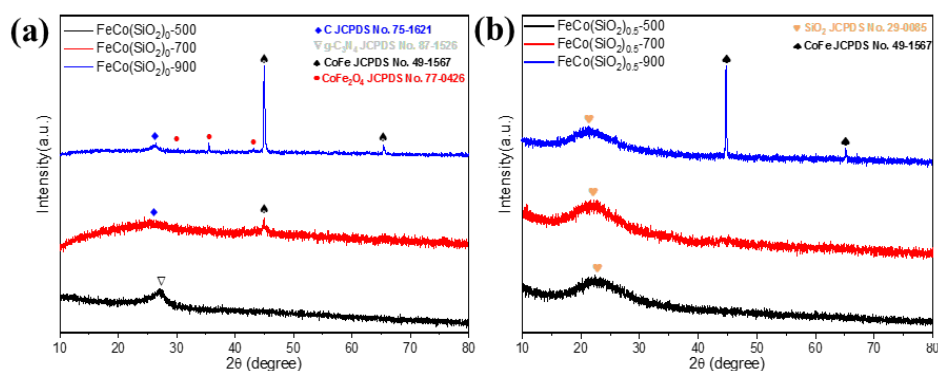


Figure 3.3 XRD patterns of pyrolysis products at different calcination stages (a) $\text{FeCo}(\text{SiO}_2)_0\text{-T}$, (b) $\text{FeCo}(\text{SiO}_2)_{0.5}\text{-T}$.

As demonstrated in the XRD diagrams in **Figure 3.3 (a) and (b)**, the lamellar structures observed at 500 °C in the control sample were attributed to $\text{g-C}_3\text{N}_4$. [112] Previous research of the carbonization of [DCA]-based ILs suggested the trimerization of cyano groups took place at approximately 500 °C, which might result in the $\text{g-C}_3\text{N}_4$. On further increasing the temperature to 900 °C, hydrogen and nitrogen in the precursor were eliminated, giving rise to the graphitic domains. [139] There were no obvious metal alloy peaks found in $\text{FeCo}(\text{SiO}_2)_0\text{-500}$, which were present in the $\text{FeCo}(\text{SiO}_2)_0\text{-700}$ and $\text{FeCo}(\text{SiO}_2)_0\text{-900}$. In the comparison of the sample with the SiO_2 template, the $\text{g-C}_3\text{N}_4$

peaks were not found, and the FeCo alloy peaks only appeared in the FeCo(SiO₂)₀-900. Since the FeCo alloys were formed at higher temperatures (900 °C versus 700 °C) when templates were involved, it was assumed that the template may hinder the incipient formation of the FeCo alloys and alleviate agglomeration at high temperature.

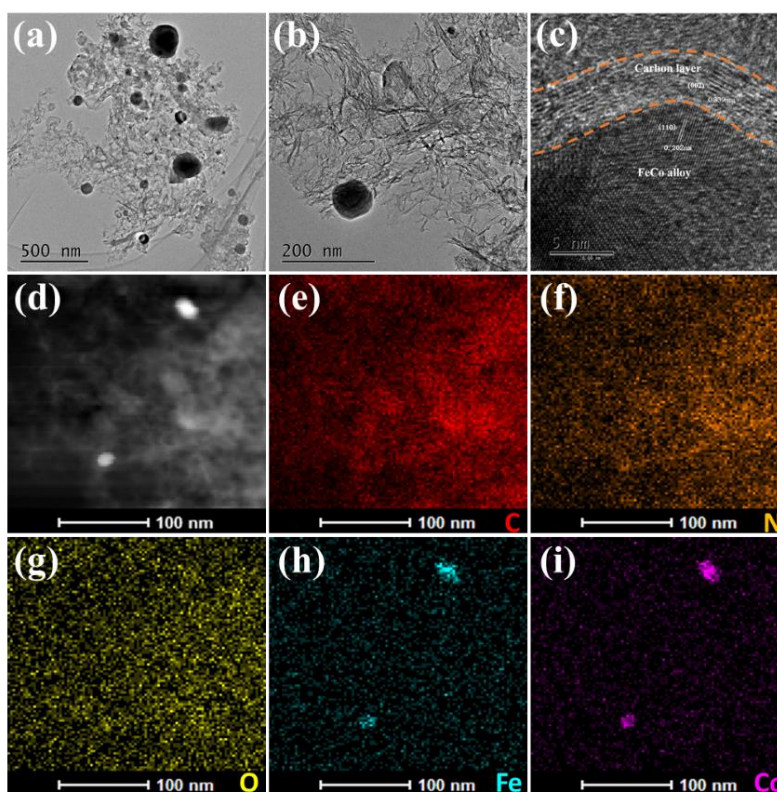


Figure 3.4 a, b, c) HRTEM image of FeCo(SiO₂)₀-900, d, e, f, g, h, i) the corresponding element mapping images of C, N, O, Fe, Co.

The morphologies and compositions of FeCo(SiO₂)₀-900 and FeCo(SiO₂)_{0.5}-900 were further investigated with HRTEM and EDS analysis, respectively. As shown in **Figure 3.4 (a) and (b)**, FeCo alloy nanoparticles between 50~ 250 nm were distributed throughout the carbon flakes. The HRTEM images showed that the FeCo alloy nanoparticles were encapsulated by carbon shells about ~5 nm thick (Figure 4.4c). The well-crystallized FeCo nanoparticles had a lattice fringe space of 2.02 Å to the (110) lattice

plane, and the carbon layer had a lattice fringe space of 3.39 Å corresponding to the (002) lattice plane of graphite, in agreement with the XRD results. Furthermore, the EDS mapping analysis was performed to probe the spatial distribution of the constituent elements (**Figure 3.4 (d) - (i)**). The uniform elemental distribution of C and N with overlapped Fe and Co mapping further verified that FeCo alloy nanoparticles were coupled with the N-doped carbon matrix. The unexpected presence of O could be the partial oxidation of FeCo nanoparticles uncovered with the carbon layer, surface oxygen, or water captured by the porous carbon in the air atmosphere. [139]

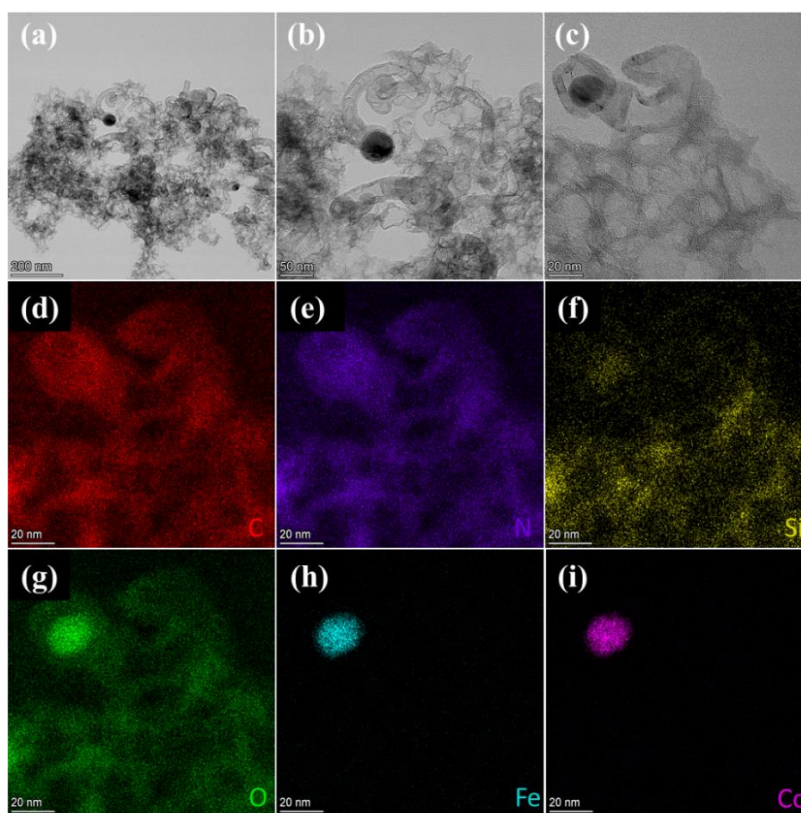


Figure 3.5 a,b,c) HRTEM image of FeCo(SiO₂)_{0.5}-900, d,e,f,g,h,i) the corresponding element mapping images of C, N, Si,O, Fe, Co.

From **Figure 3.5 (a) - (b)**, it can be observed in FeCo(SiO₂)_{0.5}-900 sample that the bamboo-like carbon nanotubes developed and extended from the fringe of the porous

carbon matrix. In **Figure 3.5 (c)**, the tubular structure was also evidenced by the open ends with wrapped alloy nanoparticles (~50 nm). The elemental mapping of the corresponding HRTEM images (**Figure 3.5 (d) – (i)**) showed that the FeCo alloy particles were rooted at the tip of CNTs, indicating a tip-growth mechanism of CNTs. The large amount of hydrocarbon volatiles generated from the decomposition of ionic liquids was catalyzed to CNTs during high-temperature pyrolysis.[69]

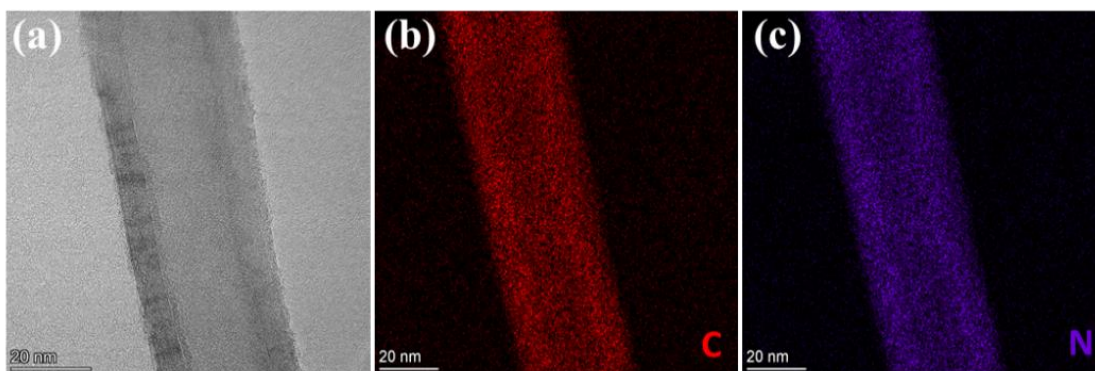


Figure 3.6 a) HRTEM image of N-CNTs in $\text{FeCo}(\text{SiO}_2)_{0.5-900}$, b,c) the corresponding element mapping images of C, N.

The obtained CNTs were further subjected to element mapping to confirm the doping of nitrogen. As shown in **Figure 3.6 (a)**, the diameters of the internodal regions of the CNTs are around ~25 nm and the wall thickness was about 5 nm. The successful doping of the nitrogen atom was evidenced by the uniform distribution of nitrogen atoms with the tubular structure, convincing that N-CNTs were formed.

With the structural characterization and composition analysis, the mechanism of template-assisted formation of carbon tubular structures was proposed as the result of the electrostatic interaction of ionic liquids and the physical segregation effects of silica nanospheres. When the pyrolysis temperature elevated, the dicyanamide condensed on the surface of silica spheres and transformed into $g\text{-C}_3\text{N}_4$, which was further catalyzed

into tubular structures by FeCo alloy catalysts.[140] Without the assistance of silica templates, carbon flakes tended to aggregate and stack face-to-face to form amorphous carbons. In sum, silica templates prevented face-to-face stacking and downsized the FeCo particle sizes, facilitating the formation of the CNTs.

3.3.2. Effects of Silica-Template on Catalyst Compositions and Structures

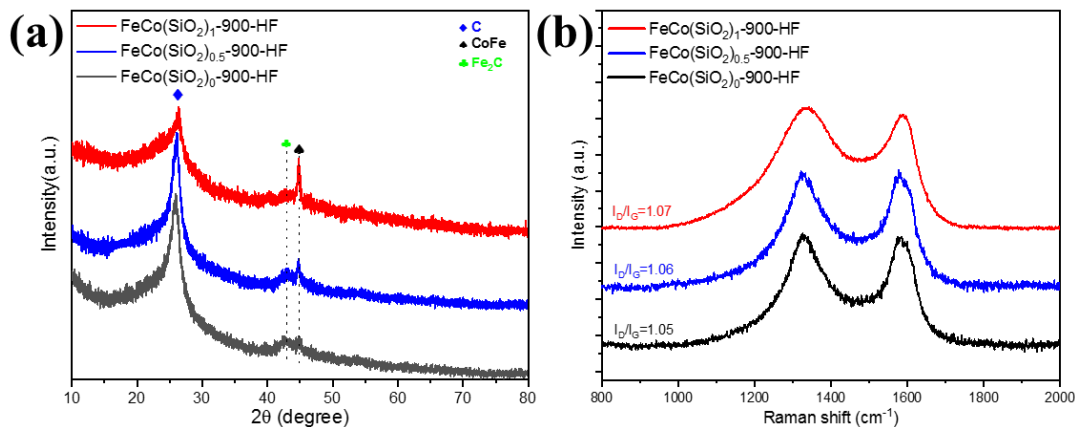


Figure 3.7 a) XRD patterns and b) Raman spectra of FeCo(SiO₂)₀-900-HF, FeCo(SiO₂)_{0.5}-900-HF and FeCo(SiO₂)_{0.5}-900-HF.

The effects of silica content on the composition and structure of catalysts were investigated by analyzing the catalysts after HF acid washing marked as FeCo(SiO₂)_x-T-HF sample series. The compositions of the samples were first determined by the XRD (**Figure 3.7 (a)**). The sharp peak at 26.3° was assigned to the (002) lattice planes of the graphitic carbon (JCPDS No. 75-1621). It can be observed that a substantial amount of metallic residuals (FeCo alloys and Fe₂C) remained after HF acid because of the shield effects of the carbon layer. The amount of encapsulated FeCo alloy particles increased as the silica content rose, demonstrating the silica template's significant influence on promoting the encapsulation of FeCo alloy particles. In addition, the increased silica content also led to more defective structures and less graphitization in carbon-based

catalysts, given that widened graphitic peak in XRD patterns and increasing defective degree in Raman spectra (**Figure 3.7 (b)**).

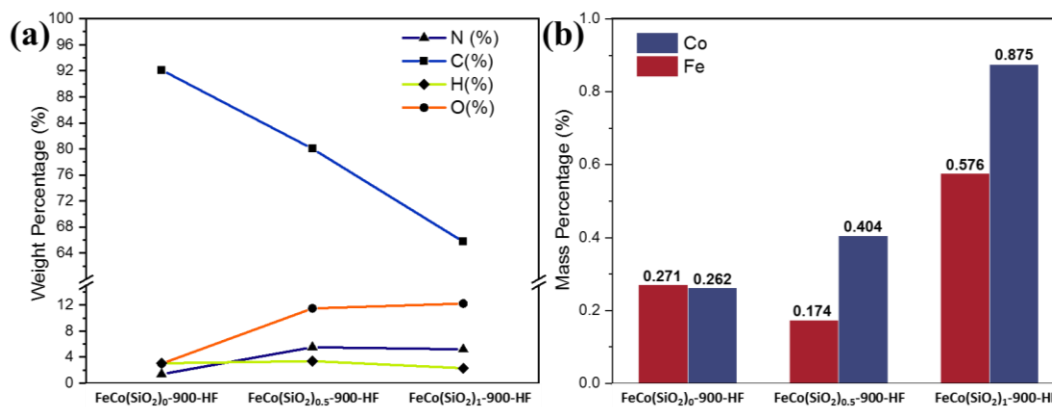


Figure 3.8 a) CHON and b) ICP-OES element analysis of FeCo(SiO₂)₀-900-HF, FeCo(SiO₂)_{0.5}-900-HF and FeCo(SiO₂)₁-900-HF, respectively.

Table 3.1 CHON element analysis of samples.

Element (wt%)	N	C	H	O
FeCo(SiO ₂) ₀ -900-HF	1.38	92.13	3.062	2.987
FeCo(SiO ₂) _{0.5} -900-HF	5.53	80.04	3.394	11.479
FeCo(SiO ₂) ₁ -900-HF	5.20	65.76	2.298	12.234

Furthermore, the compositions of the samples were determined with CHON and ICP-OES element analysis. As shown in **Figure 3.8 (a)**, the amount of nitrogen dopant in silica-assisted samples increased from 1.38 w% in FeCo(SiO₂)₀-900-HF to 5.53 w% and 5.20 w% in the FeCo(SiO₂)_{0.5}-900-HF and FeCo(SiO₂)₁-900-HF. The metal contents were quantified with ICP-OES and shown in **Figure 3.8 (b)**. The overall metal content increased with the increment of silica used in the pyrolysis. Specifically, the content of cobalt exceeded iron and aggrandized from 0.26 w% to 0.40 w% and 0.88 w%, approximating an exponential growth. In contrast, iron content decreased from 0.27 w%

to 0.17 w% and then increased to 0.58 w%. The CHON and ICP-OES element analysis convinced that the silica template significantly promoted metal encapsulation.

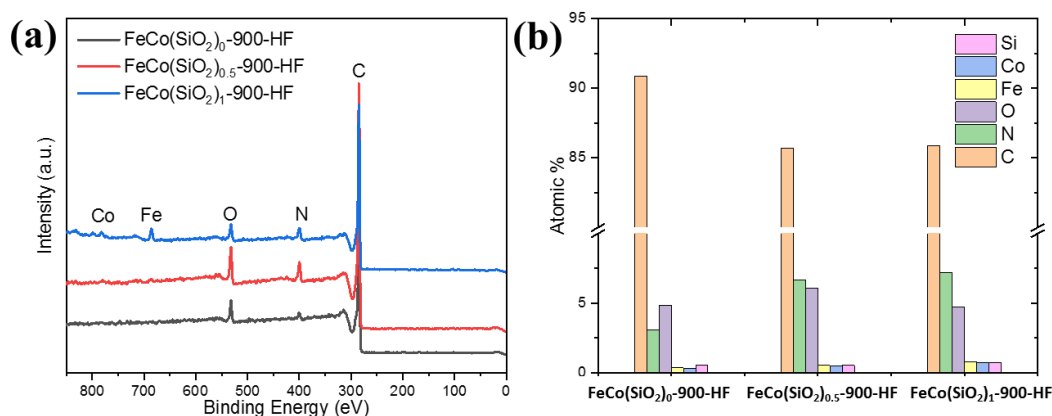


Figure 3.9 a) XPS full survey spectra, b) Atomic percentage (atom %) plots of elements as measured by XPS of FeCo(SiO₂)₀-900-HF, FeCo(SiO₂)_{0.5}-900-HF and FeCo(SiO₂)₁-900-HF.

Table 3.2 Atomic percentage (atom %) of elements as measured by XPS.

Atomic percentage (atom %)	C	N	O	Fe	Co	Si
FeCo(SiO ₂) ₀ -HF	90.9	3.05	4.85	0.36	0.31	0.53
FeCo(SiO ₂) _{0.5} -HF	85.69	6.65	6.1	0.53	0.49	0.54
FeCo(SiO ₂) ₁ -HF	85.87	7.19	4.73	0.76	0.72	0.73

The effects of different amounts of silica on the chemical state of each element in the catalysts were analyzed with XPS spectra. The full XPS survey spectra shown in **Figure 3.9 (a)** demonstrated that the nitrogen and metal dopants were enlarged with the assistance of silica, evidenced by the relatively more visible peaks. The detailed compositions on the catalyst surface were further quantified to atomic percentages and plotted in **Figure 3.9 (b)**. Interestingly, the silica exerted more influence on metal encapsulation than nitrogen doping. The nitrogen content rose 10% while the metal increased 50% in comparing FeCo(SiO₂)₁-HF with FeCo(SiO₂)_{0.5}-HF.

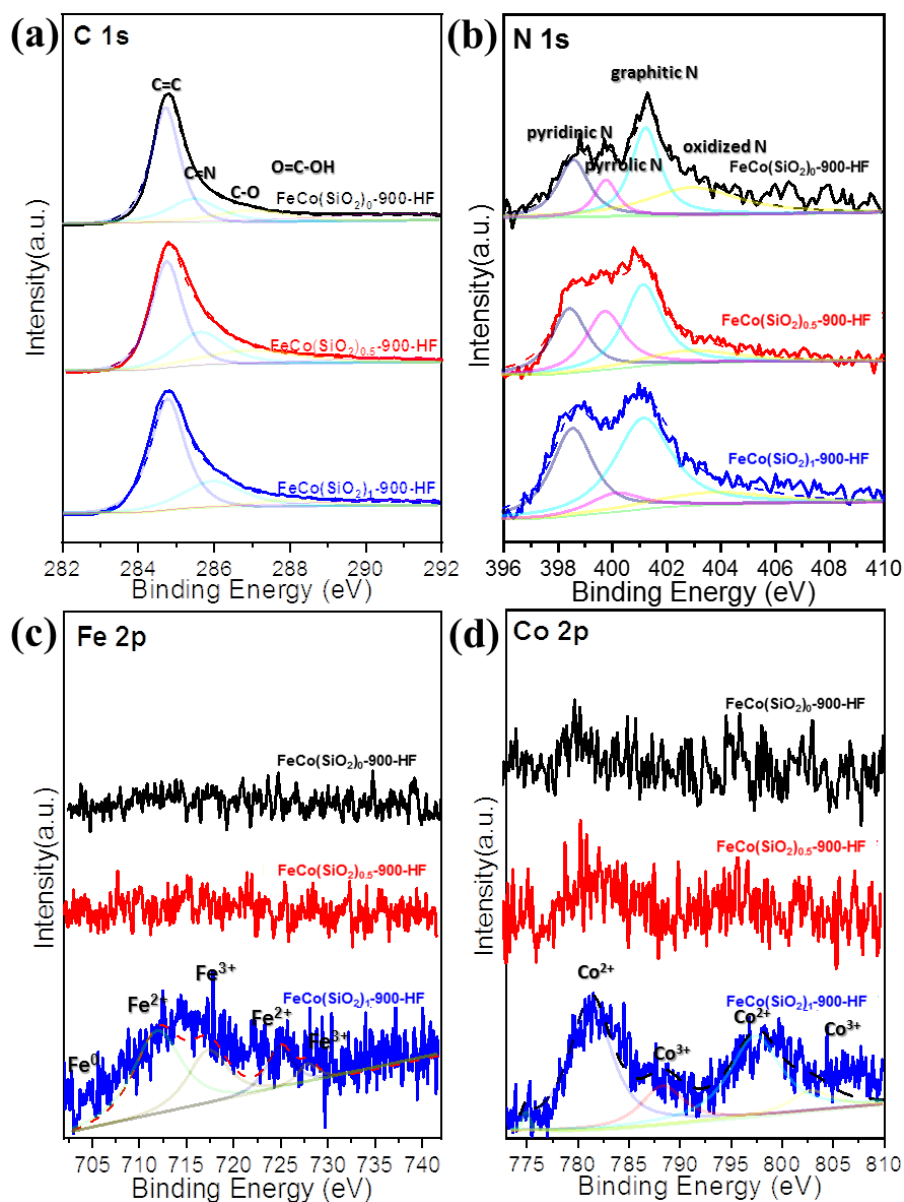


Figure 3.10 XPS spectra of $\text{FeCo}(\text{SiO}_2)_0\text{-900-HF}$, $\text{FeCo}(\text{SiO}_2)_{0.5}\text{-900-HF}$ and $\text{FeCo}(\text{SiO}_2)_1\text{-900-HF}$. a) C 1s, b) N 1s, c) Fe 2p, d) Co 2p.

As displayed in **Figure 3.10 (a)**, the C 1s spectra of samples were deconvoluted into four peaks referring to C=C, C=N, C-O, and O=C-OH, respectively. The central peak at 284.6 eV is the typical peak for sp^2 bonding of carbon atoms. The peak at 285.3 eV is related to carbon atoms bonded to more electronegative dopant atoms such as nitrogen-bonded (C=N) carbons. The presence of C=N bonding indicated that nitrogen atoms were

successfully doped into the graphitic structure. [141, 142] The broad satellite peaks in the higher binding energy region are assigned to carbon oxidizing species, such as C-O and O=C-OH, as oxidation is unavoidable when processing carbon materials in an air atmosphere. Previous works have established that the different nitrogen species have distinct impacts on the activity and selectivity of ORR electrocatalysts due to different electronic structures. The pyridinic N and graphitic N are among the most critical nitrogen species because graphitic N enhances electron transfer and the pyridinic N improves ORR activity. [143] In addition, the pyridinic N has a great metal-coordination capability which can be anchoring sites for metal atoms. **Figure 3.10 (b)** showed the four characteristic peaks of the N 1s spectrum as pyridinic N, pyrrolic N, graphitic N, and oxidized N, respectively.[142, 144] It can be observed that the pyridinic N content among N-species increased significantly by comparing FeCo(SiO₂)₁-900-HF with FeCo(SiO₂)₀-900-HF.

As mentioned above, silica improved the encapsulation of metal nanoparticles so that the peaks in Fe 2p and Co 2p spectra of the FeCo(SiO₂)₁-900-HF were more detectable than FeCo(SiO₂)₀-900-HF. In the Fe 2p spectrum, the two peaks at 712 and 726 eV were attributed to Fe 2p 3/2 and Fe 2p 1/2 of Fe²⁺/Fe³⁺ with the corresponding satellite peaks of Fe 2p 1/2 at 728 eV and Fe 2p 3/2 at 717 eV, respectively. In the Co 2p spectrum, the two peaks at 797 eV and 781 eV were assigned to Co 2p 1/2 and Co 2p 3/2 of Co²⁺/Co³⁺, respectively. And the two corresponding satellite peaks at 801 and 786 eV were assigned to Co 2p 1/2 and Co 2p 3/2, respectively. Because nano-scaled metal particles are highly susceptible to oxygen in the air and the limited permeability of X-rays, it is hard to detect the zero-valent peaks of Fe and Co by XPS. [10, 31]

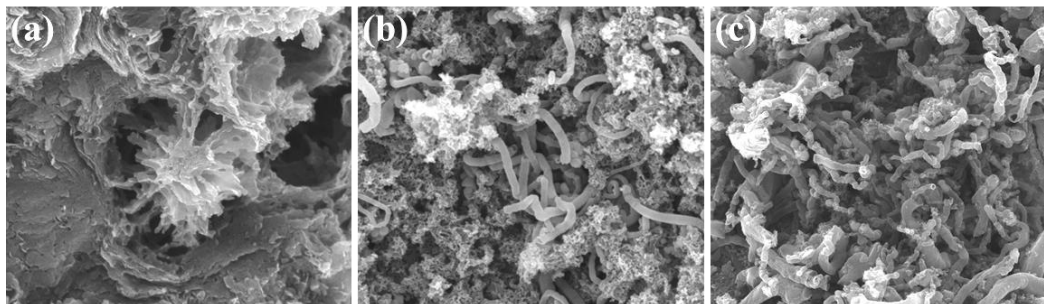


Figure 3.11 SEM images of the pyrolysis products with different silica contents. a) $\text{FeCo}(\text{SiO}_2)_0\text{-900-HF}$, b) $\text{FeCo}(\text{SiO}_2)_{0.5}\text{-900-HF}$, c) $\text{FeCo}(\text{SiO}_2)_1\text{-900-HF}$.

The remarkable effects of different silica contents on morphology were displayed in **Figure 3.11** with SEM images. It clearly showed that samples prepared in the presence of silica presented porous structure with large numbers of CNTs. In contrast, samples prepared without silica were shown as lamellar structured amorphous carbon, implying a considerable difference in specific surface area, which were validated by BET surface area analysis.

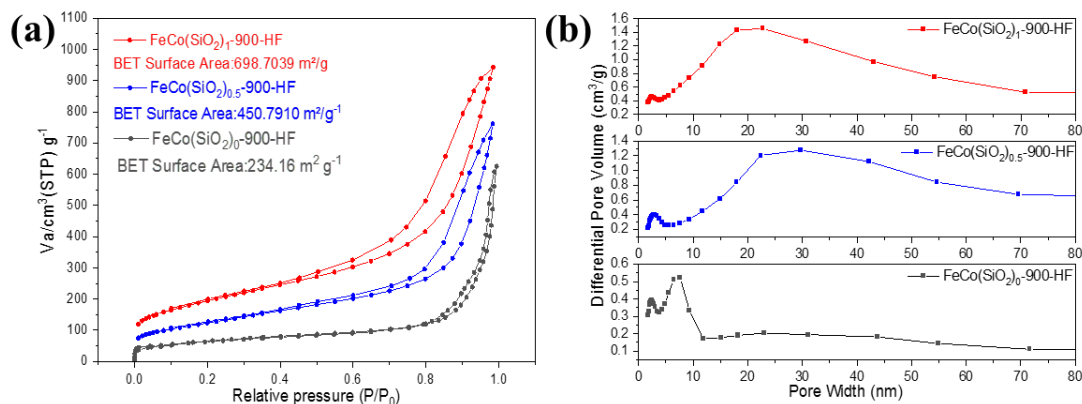


Figure 3.12 a) nitrogen adsorption isotherms, and b) pore-size distribution of $\text{FeCo}(\text{SiO}_2)_0\text{-900-HF}$, $\text{FeCo}(\text{SiO}_2)_{0.5}\text{-900-HF}$ and $\text{FeCo}(\text{SiO}_2)_1\text{-900-HF}$, respectively.

The pore structure was further studied by the N_2 -sorption at 77 K, as shown in **Figure 3.12 (a)**, all three isotherms bore the shape of type IV (a) according to the IUPAC classification, which illustrates the micro-mesoporous feature. Then the BET surface area

determination was performed following the IUPAC criteria. The surface area increased from $234.2 \text{ m}^2\text{g}^{-1}$, $450.8 \text{ m}^2\text{g}^{-1}$ to $698.7 \text{ m}^2\text{g}^{-1}$ as the silica content increased in the samples of $\text{FeCo}(\text{SiO}_2)_0$ -900-HF, $\text{FeCo}(\text{SiO}_2)_{0.5}$ -900-HF and $\text{FeCo}(\text{SiO}_2)_{0.5}$ -900-HF, respectively. The pore distribution plots in **Figure 3.12 (b)** showed the formation of mesopores in silica-assisted samples such as $\text{FeCo}(\text{SiO}_2)_{0.5}$ -900-HF and $\text{FeCo}(\text{SiO}_2)_1$ -900-HF while only micropores were found in $\text{FeCo}(\text{SiO}_2)_0$ -900-HF. [145, 146]

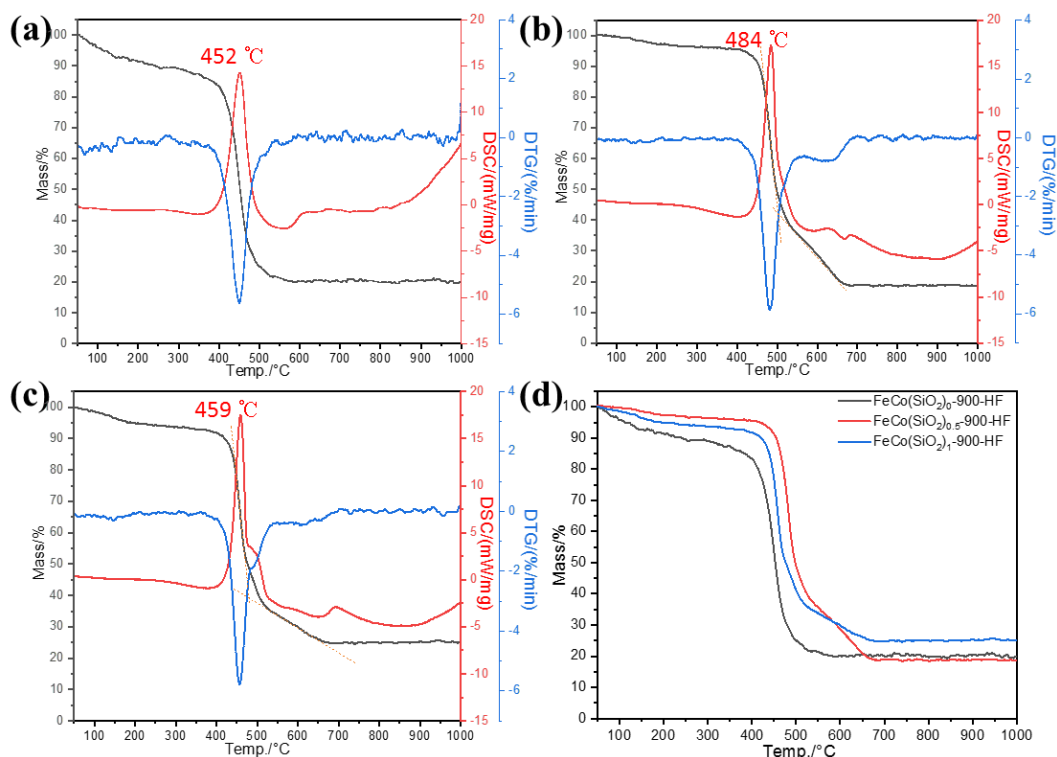


Figure 3.13 a-c) TGA and DSC curves of $\text{FeCo}(\text{SiO}_2)_0$ -900-HF, $\text{FeCo}(\text{SiO}_2)_{0.5}$ -900-HF and $\text{FeCo}(\text{SiO}_2)_1$ -900-HF, respectively. d) Enlarged image of partial TGA.

As different types of carbon materials possess different thermal-decomposition features, thermogravimetric analysis can be used to quantify the percentage of amorphous carbon, metal particles, and graphitic structured carbons such as CNTs in the $\text{FeCo}(\text{SiO}_2)_x$ -900-HF samples. The decomposition temperature of amorphous carbon ranging from 200 to 500 °C is lower than that of CNTs at or above 500 °C. [147] As shown

in **Figure 3.13 (a) - (c)**, the decomposition of $\text{FeCo}(\text{SiO}_2)_0\text{-900-HF}$ was in a one-step fashion. In contrast, the $\text{FeCo}(\text{SiO}_2)_{0.5}\text{-900-HF}$ and $\text{FeCo}(\text{SiO}_2)_1\text{-900-HF}$ decomposed in a two-step fashion, which indicated the presence of both amorphous carbons and CNTs. The primary oxidation temperature was defined as the peak temperature of DSC curves which can evaluate the thermal stability of the catalyst materials. For these catalyst materials, the oxidation temperature was 452 °C for $\text{FeCo}(\text{SiO}_2)_0\text{-900-HF}$, 484 °C for $\text{FeCo}(\text{SiO}_2)_{0.5}\text{-900-HF}$ and 459 °C for $\text{FeCo}(\text{SiO}_2)_1\text{-900-HF}$, respectively. The major mass loss (~50 %) occurred at the oxidation temperatures during the first stage which was attributed to the combustion of amorphous carbon. The second stage was ascribed to the oxidation of CNTs which can be used to assess the CNT fractions in each sample, giving an estimated 22.5 w% for $\text{FeCo}(\text{SiO}_2)_{0.5}\text{-900-HF}$ and 15.0 w% for $\text{FeCo}(\text{SiO}_2)_1\text{-900-HF}$, respectively. The weight reached a plateau after heated to 700 °C, indicating the carbon-containing constituents decomposed thoroughly and only catalytic metals and their oxidation products were left.[148]

3.3.3. Electrocatalytic ORR Performance of Catalysts

To investigate the effect of the CNTs on the ORR kinetics of the as-obtained materials, multiple electrochemical tests including cyclic voltammetry (CV) and linear sweep voltammetry (LSV) coupled with rotating disk electrode (RDE)/rotating ring-disk electrode (RRDE) were employed to evaluate the ORR performance.

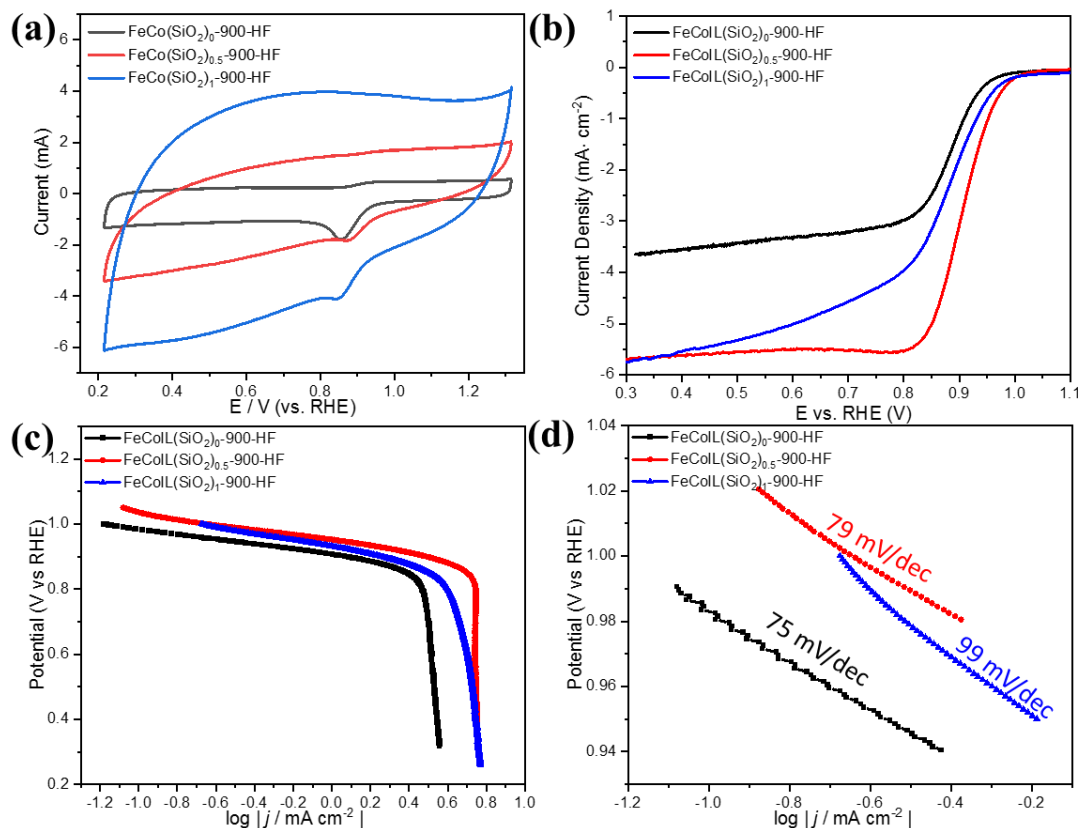


Figure 3.14 ORR performances of FeCo(SiO₂)₀-900-HF, FeCo(SiO₂)_{0.5}-900-HF and FeCo(SiO₂)₁-900-HF in O₂-saturated 0.1 m KOH. a) CV curves, b) ORR polarization curves, c) Corresponding Tafel plot of ORR polarization curves, d) Enlarged Tafel plot in kinetic control region.

As shown in **Figure 3.14 (a)**, the CV curves of FeCo(SiO₂)₀-900-HF, FeCo(SiO₂)_{0.5}-900-HF and FeCo(SiO₂)₁-900-HF in the O₂-saturated electrolyte exhibit well-defined cathodic oxygen reduction peaks. The peak potential are at 0.85 V for FeCo(SiO₂)₀-900-HF, 0.87 V for FeCo(SiO₂)_{0.5}-900-HF and 0.84 V for FeCo(SiO₂)₁-900-HF, respectively. Accordingly, the FeCo(SiO₂)_{0.5}-900-HF is most effective at facilitating ORR followed by FeCo(SiO₂)₀-900-HF and FeCo(SiO₂)₁-900-HF. In addition, the CV areas of the FeCo(SiO₂)₀-900-HF, FeCo(SiO₂)_{0.5}-900-HF and FeCo(SiO₂)₁-900-HF increase incrementally, indicating a moderate amount of silica in catalyst preparation can greatly enlarge the electroactive area and improve the ORR activity.[149] The ORR polarization

curves in **Figure 3.14 (b)** showed that $\text{FeCo}(\text{SiO}_2)_{0.5}\text{-900-HF}$ outperforms other samples with a half-wave potential of 0.87 V vs. RHE and a high diffusion-limited current density of $5.7 \text{ mA}\cdot\text{cm}^{-2}$. Though $\text{FeCo}(\text{SiO}_2)_{0.5}\text{-900-HF}$ and $\text{FeCo}(\text{SiO}_2)_1\text{-900-HF}$ have similar onset potentials, an indication of identical intrinsic activity, the lower half-wave potential and higher diffusion-limited current suggest the superior conductivity and abundant electroactive sites of $\text{FeCo}(\text{SiO}_2)_{0.5}\text{-900-HF}$ which can be attributed to the extrinsic properties of the electrocatalysts. [144, 150] The kinetic activity was evaluated with Tafel plots derived from the ORR polarization curves in kinetic-control regions. As can be seen from **Figure 3.14 (c)**, the Tafel plots with different potentials presented the proper overpotential ranges of each sample which were identified as kinetic-control regions. Accordingly, $\text{FeCo}(\text{SiO}_2)_0\text{-900-HF}$, $\text{FeCo}(\text{SiO}_2)_{0.5}\text{-900-HF}$ and $\text{FeCo}(\text{SiO}_2)_1\text{-900-HF}$ exhibits Tafel slopes of 75 mV/dec, 79 mV/dec, 99 mV/dec, respectively in **Figure 3.14 (d)**. The region of the Tafel slope between 60 and 120 mV/dec suggests an oxygen reduction mechanism that is limited by the initial electron transfer of O_2 reduction.[151]

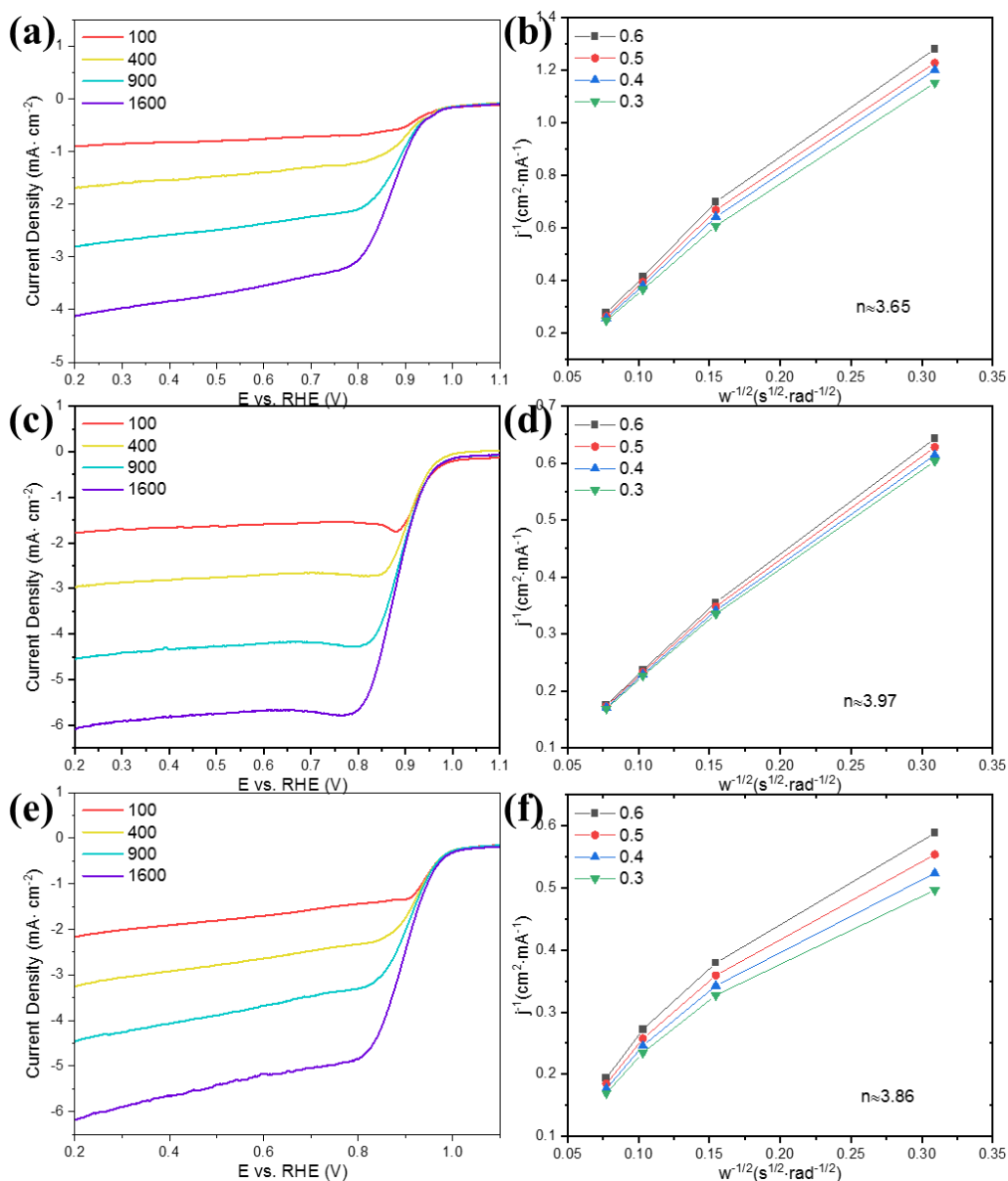


Figure 3.15 ORR polarization curves at various rotation rates in rpm and the corresponding K–L plots: a-b) FeCo(SiO₂)₀-900-HF, d-c) FeCo(SiO₂)_{0.5}-900-HF and e-f) FeCo(SiO₂)₁-900-HF.

The number of transferred electrons per oxygen molecule in ORR was calculated from K-L plots to evaluate the efficiency of catalysts. As shown in **Figure 3.15**, the ORR polarization curves under different rotation speeds were collected and the corresponding K-L slopes were obtained from the plot of the inverse of the current density ($1/j$) against the inverse of the square root of the angular velocity ($w^{-1/2}$). The electron-transfer number

(n) calculated from the K-L slopes were 3.65, 3.97, 3.86 for FeCo(SiO₂)₀-900-HF, FeCo(SiO₂)_{0.5}-900-HF and FeCo(SiO₂)₁-900-HF, respectively, suggesting an approximate four-electron pathway for ORR.

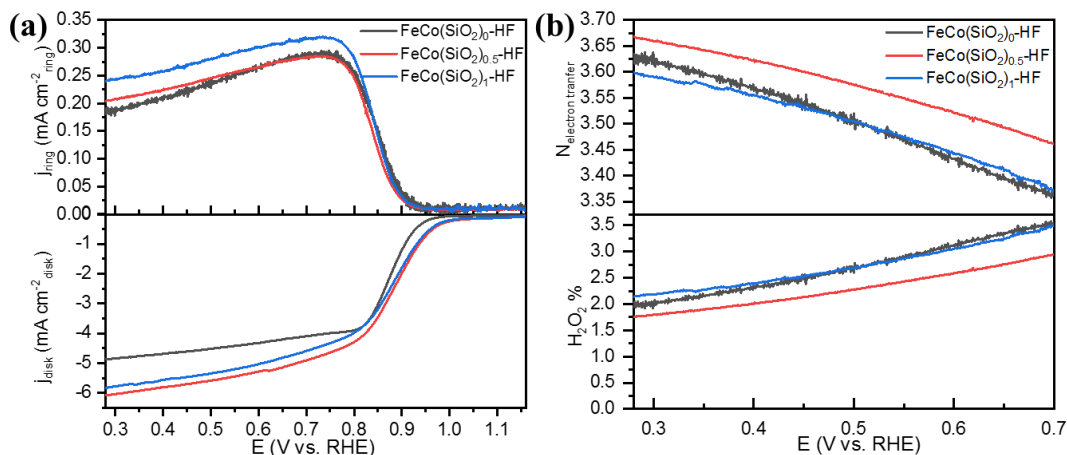


Figure 3.16 a) H₂O₂% yield and b) electron transfer number calculated from RRDE results of FeCo(SiO₂)₀-900-HF, FeCo(SiO₂)_{0.5}-900-HF and FeCo(SiO₂)₁-900-HF.

Furthermore, the rotation ring and disk electrode (RRDE) measurements were performed to investigate the efficiency of oxygen conversion. [152] As shown in **Figure 3.16 (a)**, the H₂O₂ yield of the obtained catalysts at the ring electrode is below 3.5%, indicating that the majority of oxygen undergoes an approximate four-electron transfer during reduction. Among the FeCo(SiO₂)_x-900-HF samples, FeCo(SiO₂)₀-900-HF produces more H₂O₂ intermediates than FeCo(SiO₂)_{0.5}-900-HF and FeCo(SiO₂)₁-900-HF, suggesting lesser efficiency in oxygen reduction. As shown in **Figure 3.16 (b)**, the FeCo(SiO₂)₀-900-HF catalyst demonstrates the best electrocatalytic activity and selectivity with less H₂O₂ yield and more transferred electrons.

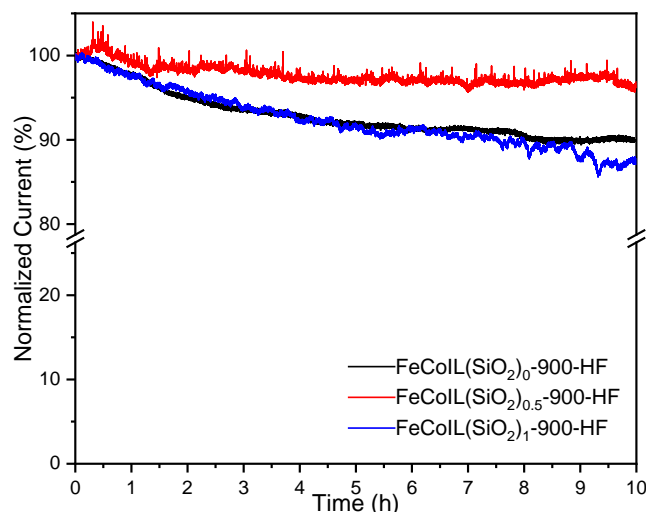


Figure 3.17 Amperometric i-t curve of FeCo(SiO₂)₀-900-HF, FeCo(SiO₂)_{0.5}-900-HF and FeCo(SiO₂)₁-900-HF in 0.1 M KOH with 1600 rpm rotation rate.

The durability test of FeCo(SiO₂)_x-900-HF catalysts were studied by the time-dependent current density curves collected at the static potential of 0.7 V vs. RHE. As shown in **Figure 3.17**, the FeCo(SiO₂)_{0.5}-900-HF catalyst demonstrates the most stable catalytic activity with only 3.6 % current loss after continuous working for 10 hrs. In comparison, the FeCo(SiO₂)₀-900-HF and FeCo(SiO₂)₁-900-HF exhibit similar current degradation with 10.0 % and 12.3 % loss.

3.4. Conclusion

In this chapter, we have demonstrated a facile strategy to prepare N-CNTs from the metal salts/ionic liquids precursor with the assistance of silica template as highly efficient ORR electrocatalysts. It was shown that the silica template promoted the formation of N-CNTs by preventing the face-face stacking of the formed carbon materials and downsizing the FeCo alloy nanoparticles during the ionic liquid pyrolysis. The involvement of silica rendered the carbon-based electrocatalysts with a large specific surface area, proper pore size distribution, and effective doping, facilitating mass transport and electron

transfer in the electrochemical reaction. In our metal salts/ionic liquids system, the N content increased from 1.38 w% to about 5.53 w%, and the surface area increased from 234.2 m²/g to 698.7 m²/g. The template-assisted electrocatalysts possessed higher onset and half-wave potential and better durability. Our work presents a new approach toward the synthesis of N-CNTs, which will have broad applications in fuel cells and metal-air batteries.

Chapter 4

4. Ionic Liquid-Derived FeCo Alloys Encapsulated in Nitrogen-Doped Carbon Framework as Advanced Bifunctional Catalysts for Zn-Air Batteries

Portions of this work have been published:

Zhenzhen Wang, Xiaozhuang Zhou, Huihui Jin, Ding Chen, Jiawei Zhu, Rolf Hempelmann, Lei Chen, and Shichun Mu. "Ionic liquid-derived FeCo alloys encapsulated in nitrogen-doped carbon framework as advanced bifunctional catalysts for rechargeable Zn-air batteries." *Journal of Alloys and Compounds* 908 (2022): 164565. DOI: 10.1016/j.jallcom.2022.164565

Abstract: Developing bifunctional ORR&OER electrocatalysts with high activity and stability is challenging for practical application of rechargeable Zinc air batteries. Herein, an ionic liquid strategy is proposed for construction of FeCo alloys encapsulated in nitrogen-doped carbon as bifunctional electrocatalyst for oxygen reduction reaction (ORR) and oxygen evolution reaction (OER). By taking advantages of the unique properties such as solvent effect and low volatility, ionic liquid serves as solvent to disperse metal ions in the precursor preparation and nitrogen-containing carbon source during pyrolysis. The

FeCo alloy nanoparticles encapsulated in the N-doped carbon matrix show a homogeneous distribution with average sizes of 50-100 nm. Such a core-shell structure endows the catalyst with both high ORR and OER activity and robust stability in alkaline environments. Especially, the half-wave potential ($E_{1/2}$) for ORR is 0.86V and the overpotential (E_{over}) for OER to reach the $10 \text{ mA}\cdot\text{cm}^{-2}$ current density is only 280 mV. Furthermore, the obtained bifunctional electrocatalyst also displays high efficiency and great durability when applied in the rechargeable Zn-air battery. The specific capacity and energy density at the discharge current density of $10 \text{ mA}\cdot\text{cm}^{-2}$ reach up to $741.5 \text{ mAh}\cdot\text{g}^{-1}$ and 830.1 Wh kg^{-1} , respectively. It's envisioned that this ultra-facile method would be applicable to synthesize highly efficient catalysts for other energy conversion systems.

4.1. Introduction

With growing awareness of energy shortage and environment pollution caused by depletion of traditional fossil fuels, the pursuit for alternative energy and corresponding energy conversion devices have been gaining great momentums. Rechargeable zinc-air batteries (ZABs) stand out as one of the most promising candidates for future electric vehicles and other energy-consumption devices by virtue of their high theoretical energy density ($1086 \text{ Wh}\cdot\text{kg}^{-1}$), low price ($<10\$$ per kWh estimated) and good safety.[153-156] The oxygen reduction reaction (ORR) and oxygen evolution reaction (OER), which are two pivotal reactions on the oxygen electrode of ZABs, usually demand highly active electrocatalysts to overcome their large activation barrier and sluggish kinetics. Noble metals (Pt-based) and their metal oxides (Ru/Ir-based) have been acknowledged as the state-of-the-art catalysts for ORR and OER, respectively. However, their prohibitive cost, scarce reserve and poor durability significantly hamper widespread applications.

Moreover, none of these noble-based catalysts are capable of providing satisfactory activities in ORR and OER simultaneously. Therefore, in order to reduce the cost and complexity for the implementation of rechargeable ZABs, a burgeoning effort has been made to develop cheap yet highly active bifunctional electrocatalysts for ORR and OER.

Numerous studies have highlighted the excellent ORR catalytic activities of iron-nitrogen-carbon (Fe-N-C) materials, which is even superior to commercial Pt/C.[157-159] However, the practical application of Fe–N–C materials in rechargeable ZABs is restrained by its inferior OER activity, as high anodization voltage under alkaline environment stimulate the generation of semi-conductive oxyhydroxide species that hamper electron transfer.[160] Transitional metal (TM) alloying especially those with Co, Ni has been proven feasible to offset the adverse effect of hydroxyl oxidation by way of enhancing conductivity and protecting Fe sites.[111, 112] In essence, the electronic interaction between TM alloys and nitrogen-doped support imparts the electrocatalyst materials with diverse active species, abundant active sites, improved conductivity, and higher corrosion-resistance during the electrochemical reactions.[101-106] Among various combinations of TM alloys and NC, encapsulation or immobilization of TM alloy nanoparticles with thin NC shells (TM alloy@NC) is attracting special attention as this unique structure could enhance electrocatalytic activity and stability of electrocatalysts. [110, 161-164] Given all that, different approaches such as template methods, CVD methods, and calcination of solid-state precursors have been exploited to prepare the TM alloy@NC bifunctional electrocatalysts.[112, 163, 165-169] Though the advances, these conventional methods which involve predefined structured precursors are process trivial, complex and difficult to ensure the homogeneity of catalysts. [140, 170, 171] It remains a

challenge to prepare homogeneous TM alloy@NC bifunctional catalysts from a simple route.

Herein, we put forward a simple blending-annealing two-step strategy for fabricating the highly efficient TMs alloy@NC bifunctional electrocatalysts by employing ionic liquid (IL). In this work, ILs whose ligand have Lewis basic properties serve as the solvents for metal ions ,[85] and as the NC precursors with a high carbon yield after pyrolysis. [172] It is believed that the solvation interaction between metal ions and the ILs improves the dispersion of metal ions in precursor as well as the homogeneity of the catalysts materials after annealing.[170] Distinct from the calcination of the solid-state powders, the decomposition of ionic liquids mixtures remained in the liquid state. Notably, in our method, not only metal inorganic salts, but metal organic salts could be used for preparation of the catalysts. Apart from that, the structures and the components of the ILs-derived carbon materials could be manipulated via adopting different ILs .[85] By simply annealing the mixture of metal salts and ILs, we expect to obtain the homogeneously dispersed TM alloy encapsulated with NC as bifunctional electrocatalysts. In order to demonstrate our concept, we employed FeCl_3 and CoCl_2 and 1-ethyl-3-methylimidazolium dicyanamide ([emim] [DCA]) to prepare the FeCo@NC catalysts. As anticipated, the obtained FeCo@NC displays typical core-shell structures and superior catalytic performance toward ORR and OER in an alkaline electrolyte. Impressively, the assembled rechargeable Zn-air battery device exhibit great specific capacity and cycling performance in liquid and all-solid-state zinc-air batteries. This work provides an ultra-facile approach for the fabrication of TM alloy/NC bifunctional electrocatalysts and

demonstrates its great potential to synthesize highly efficient catalysts for other energy conversion systems.

4.2. Experimental Section

Cobalt (II) chloride hexahydrate ($\text{CoCl}_2 \cdot 6\text{H}_2\text{O}$, 99%, Shanghai Aladdin Biochemical Technology Co. Ltd), iron (III) chloride anhydrous (FeCl_3 , 99%, Shanghai Aladdin Biochemical Technology Co. Ltd) and 1-ethyl-3-methylimidazolium dicyanamide ([emim] [DCA], Sigma) were used as purchased without any further treatment. 0.5 mmol $\text{CoCl}_2 \cdot 6\text{H}_2\text{O}$ and 0.5 mmol FeCl_3 were ultrasonically dissolved in each 1 mL [emim] [DCA] separately and then blended together. The obtained mixture solution was transferred to an alumina crucible and annealed for 2 hrs at 900 °C in Argon atmosphere (99% purity) at a heating rate of 10 °C/min. After natural cooling to room temperature, the final product was ground and denoted as FeCo@NC. For comparison, Fe@NC, Co@NC, and NC were synthesized following the same procedure by varying the addition of FeCl_3 or CoCl_2 . In order to investigate the effects of acid wash, FeCo@NC catalysts was purified by overnight refluxing in 100 mL sulfuric acid solution (2 M) in air at 110 °C to remove any metallic particles produced during pyrolysis.

4.3. Results and Discussion

4.3.1. Material Characterization Results



Figure 4.1 Synthesis process of FeCo@NC,

As illustrated in **Figure 4.1**, the preparation of precursors is a typical dissolution-solvation process where ionic liquid serves as solvent.

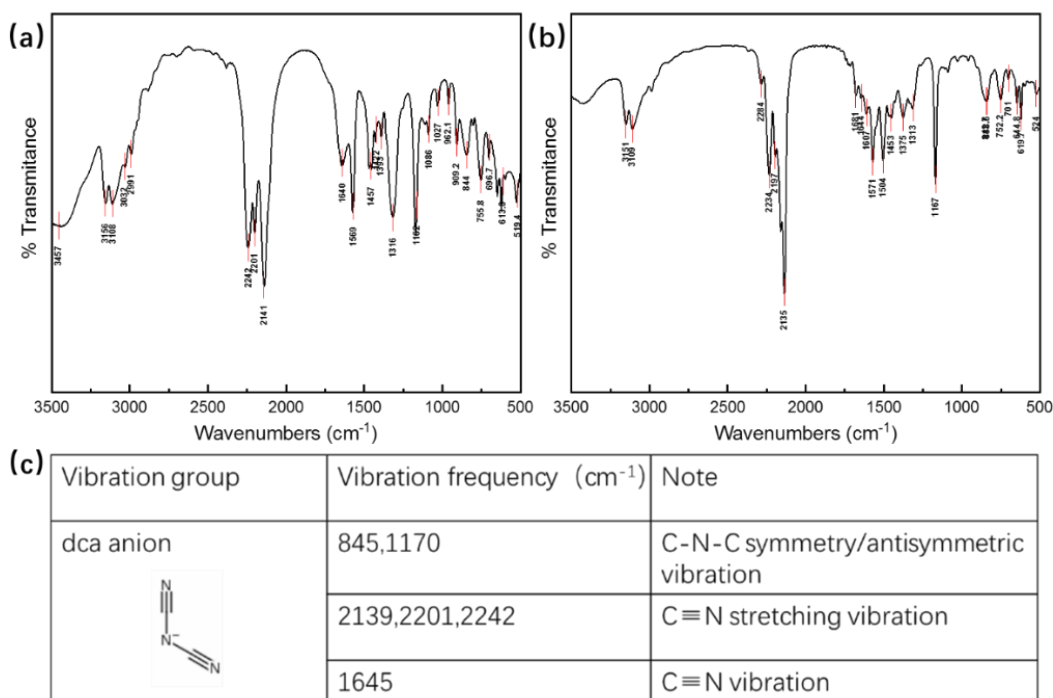


Figure 4.2 a) FT-IR spectrum of pure [emim][DCA], b) FT-IR spectrum of [emim][DCA] and FeCl₃&CoCl₂ mixture, c) Vibration frequency list of dca anion.

The strong interaction between dicyanamide anions and metal ions can be proved by the FT-IR spectra that the absorption peak of C≡N group vibration shift to low

wavenumber domain (**Figure 4.2**). The dicyanamide anions can act as the metal-ligands to form dicyanamido-metallate, enabling the homogeneous dispersion of metal ions in the IL-precursor.[135]

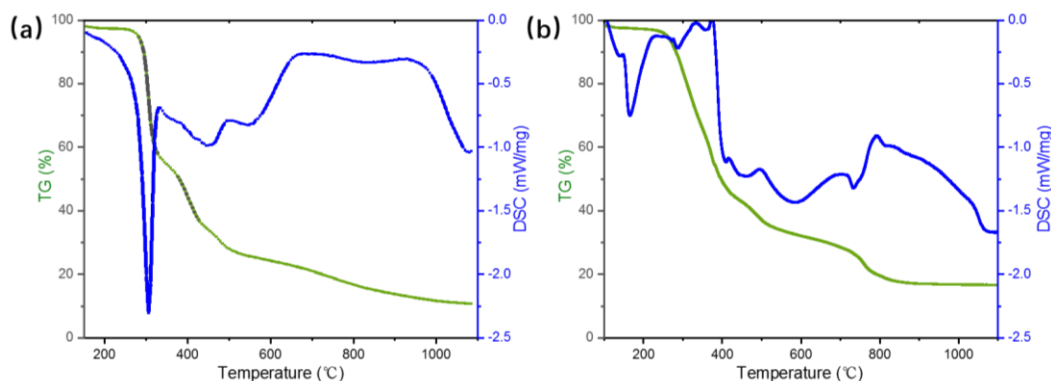


Figure 4.3 DSC and TG curves of a) pure [emim][DCA], b) [emim][DCA] and FeCl₃&CoCl₂ mixture, at heating rate of 5 °C/min in argon atmosphere.

The thermogravimetric analysis (TG) and differential scanning calorimetry (DSC) show that the annealing [emim] [DCA] and the mixture of [emim] [DCA]/FeCl₃/CoCl₂ reach to a plateau phase until heated to 900 °C (**Figure 4.3**). Thus, all the catalysts were annealed at 900 °C to ensure no phase transformation would occur.

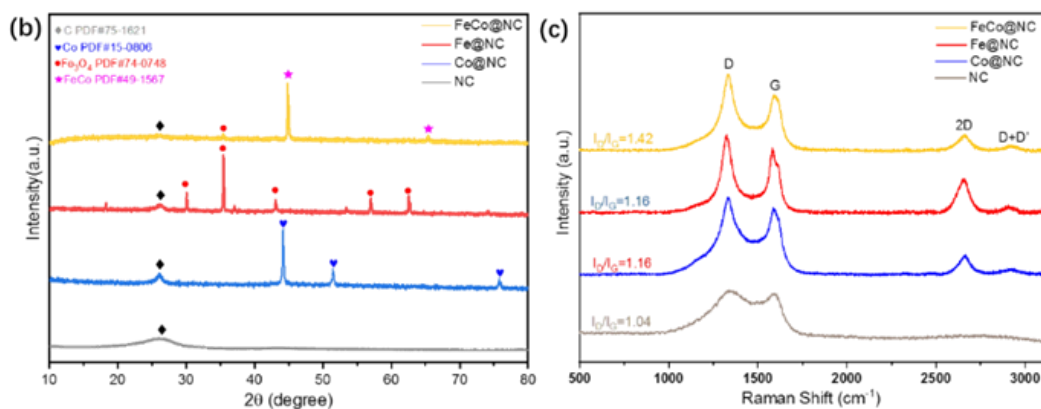


Figure 4.4 a) XRD patterns and b) Raman spectra of FeCo@NC, Fe@NC, Co@NC and NC.

As demonstrated in the XRD patterns (**Figure 4.4 (a)**), the sharp peaks at 44.8° and 65.3° are assigned to the (110) and (200) facets of cubic bimetal FeCo alloy (JCPDS No.

49-1567), indicating the formation of crystalline FeCo alloy. The slight peak at 26.3° is attributed to the (002) lattice planes of the hexagonal graphitic carbon domains (JCPDS No. 75-1621). In contrast, the Fe@NC and Co@NC tend to form Fe_3O_4 (JCPDS No. 74-0748) and Co (JCPDS No. 18-0805), respectively. In addition, the defect structure of the carbon matrix was investigated by Raman spectra. As seen in **Figure 4.4 (b)**, the two dominant bands were assigned to graphene edges or defects (D band, 1330 cm^{-1}) and characteristic graphitic lattice (G, 1588 cm^{-1}).^[173] Note that, FeCo@NC possesses the highest I_D/I_G values of 1.42 compared with that of Fe@NC (1.16), Co@NC (1.16) and NC (1.04), indicating higher density of defects or edges in the carbon framework. The other two visible band peaks at 2659 cm^{-1} and 2910 cm^{-1} are assigned as 2D and D+D' band, respectively. The broad 2D band peak evinces the multi-layer stacked graphene structure in carbon. And the evident D+D' bands in the spectra of metal-containing samples indicate the vital role of the Fe and Co metal in generating defects in carbon.^[174]

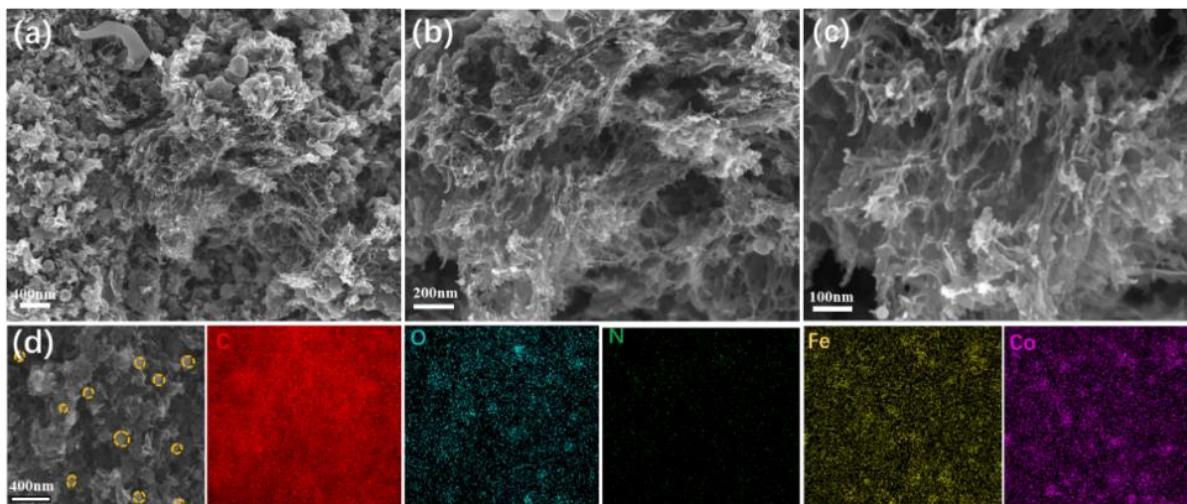


Figure 4.5 a-c) SEM images of FeCo@NC, d) Corresponding EDS elemental mapping

Scanning electron microscope (SEM) images in **Figure 4.5 (a)-(c)** display the highly porous morphology of the carbon matrix with distributed FeCo alloy nanoparticles for the

obtained FeCo@NC. The FeCo nanoparticles in the range from 50 nm to 100 nm are circled by orange marks in **Figure 4.5 (d)**. The composition of these nanoparticles was further confirmed by Energy Dispersive Spectrometry (EDS) mapping where the dots of Co and Fe share the overlapped area.

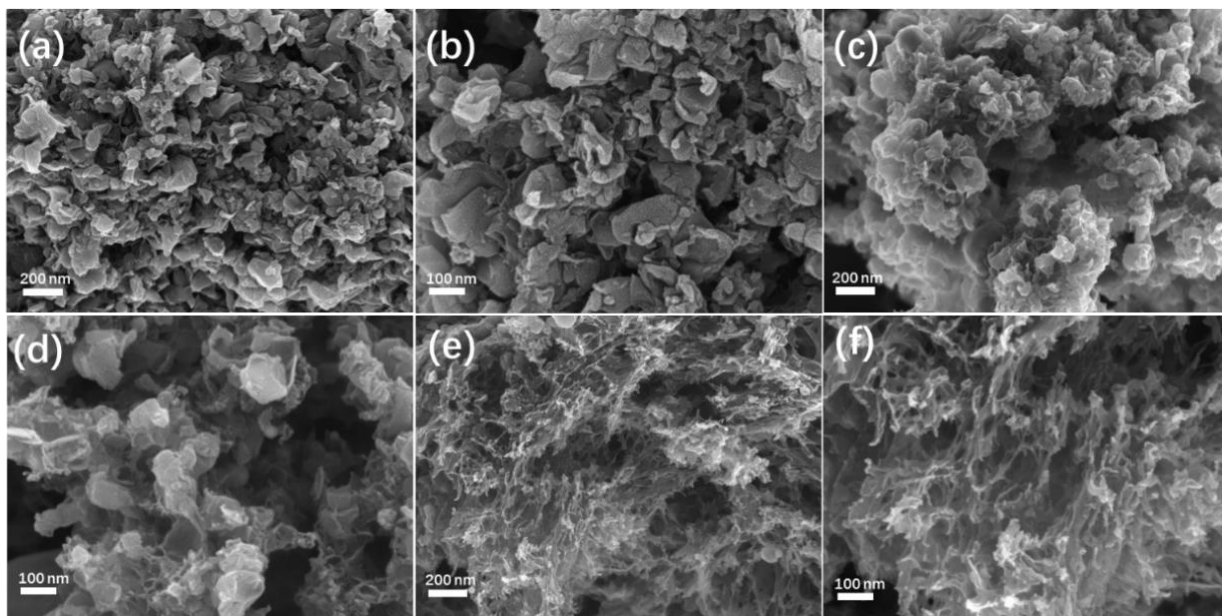


Figure 4.6 SEM images of a, b) Fe@NC, c, d) Co@NC e, f) FeCo@NC.

In comparison with Fe@NC, samples containing Co such as Co@NC and FeCo@NC are inclined to establish a highly porous network of carbon (**Figure 4.6**). This phenomenon manifests the key role of Co in promoting the formation of a highly porous carbon network. Previous work has proposed that elemental Fe and Co can serve as the catalysts for the growth of porous carbon network, which facilitates the mass transfer and electron transfer during catalysis process. [111, 175]

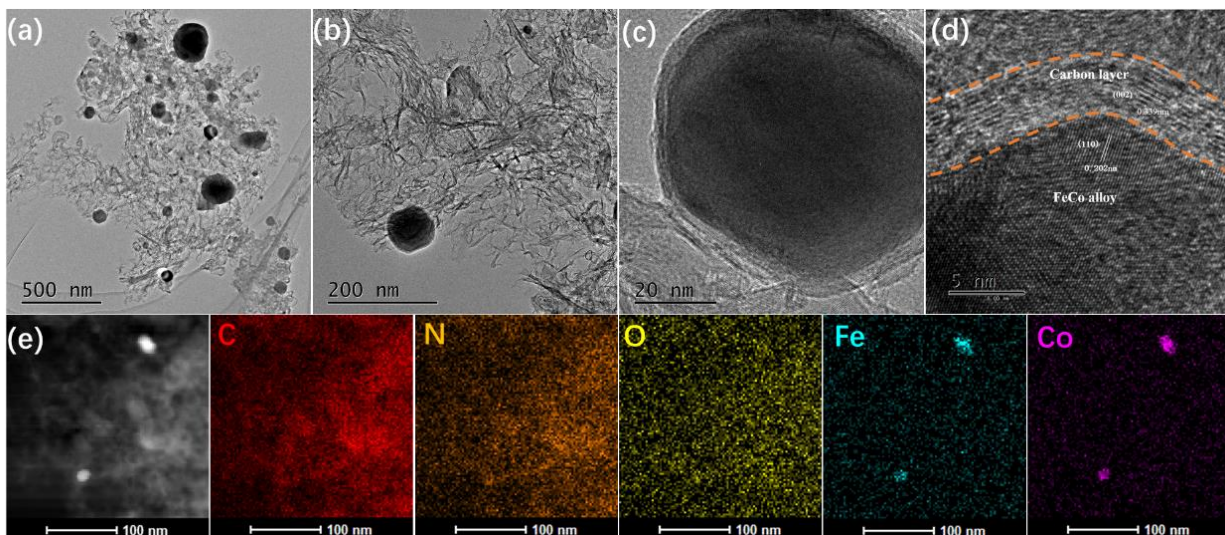


Figure 4.7 a, b) HRTEM image, c) the corresponding element mapping images of C, N, O, Fe, Co.

Transmission emission microscopy (HRTEM) was used to further investigate the microstructure of FeCo@NC. As seen from **Figure 4.7 (a) - (b)**, FeCo nanoparticles embedded in the carbon matrix. The HRTEM images manifest that the FeCo alloy nanoparticles are encapsulated by carbon shells about ~5 nm thickness (**Figure 4.7 (c) - (d)**). The well-crystallized FeCo nanoparticles have a lattice fringe space of 2.02 Å to the (110) lattice plane, and the carbon layer has a lattice fringe space of 3.39 Å corresponding to the (002) lattice plane of graphite, in agreement with the XRD results. These results clearly demonstrate the successful encapsulation and immobilization of FeCo alloy nanoparticles in the porous carbon matrix. Furthermore, the EDS mapping analysis was performed to probe the spatial distribution of the constituent elements (**Figure 4.7 (e)**). The uniform elemental distribution of C and N with overlapped Fe and Co further verifies that FeCo alloy nanoparticles are coupled with the N-doped carbon matrix in FeCo@NC. The unexpected presence of O could be the partial oxidation of FeCo nanoparticles uncovered with carbon layer or the surface oxygen or water captured by the porous carbon in the air atmosphere. [139]

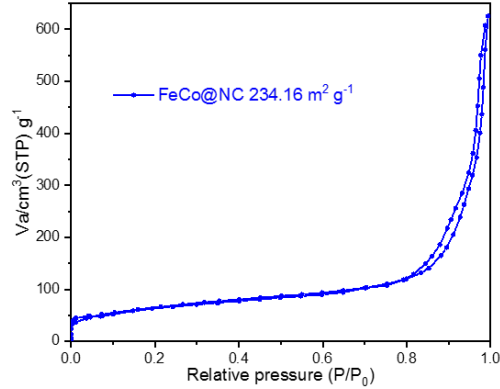


Figure 4.8 N₂ adsorption–desorption isotherm of FeCo@NC.

As shown in **Figure 4.8**, the porous structure was further studied by the N₂ adsorption measurements. The isotherm shape belongs to the type IV (a) according to the IUPAC classification which illustrates a distinct micro-mesoporous character. And the BET surface area determination was performed following the IUPAC criteria and gave the value of 234 m²·g⁻¹. [145]

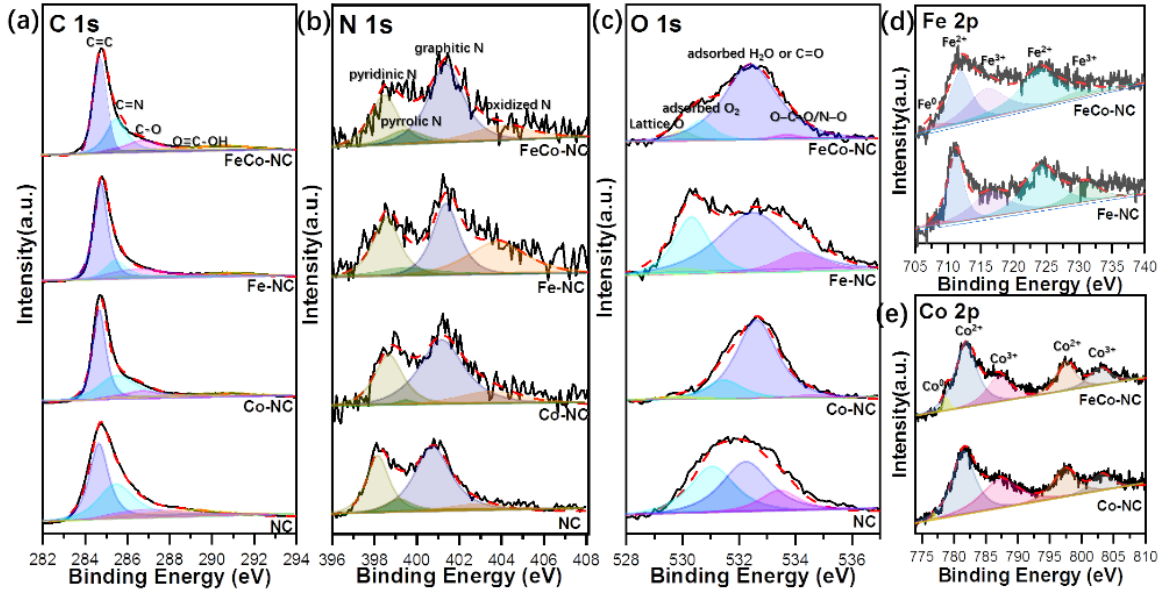


Figure 4.9 XPS spectra of FeCo@NC, Fe@NC, Co@NC and NC. a) C 1s, b) N 1s, c) O 1s, d) Fe 2p, e) Co 2p.

The high-resolution X-ray photoelectron spectra (XPS) of C 1s, N 1s, O 1s, Fe 2p and Co 2p of each sample are presented in **Figure 4.9**. As displayed in **Figure 4.9 (a)**, the C

1s spectra of samples can be deconvoluted into four peaks centered at 284.6 eV, 285.3 eV, 286.5 eV, and 290 eV. The broad satellite peaks at 286.5 and 290 eV in the higher binding energy region could be ascribed to the oxidized carbon species such as C-O and O=C-OH, seeing that the oxidation of carbon materials is inevitable when handled in an air atmosphere. The dominant peak at 284.6 eV is typical for sp^2 binding of carbon atoms and the peak at 285.3 eV is related to the carbon atoms binding to more electronegative dopant atoms such as nitrogen-bonded (C=N) carbon in this work. The presence of C=N bond suggests the successful incorporation of nitrogen into the carbon skeleton.[141, 142]

Figure 4.9 (b) presents four characteristic peaks of the N 1s spectrum corresponding to pyridinic N, pyrrolic N, graphitic N, and oxidized N, respectively.[142, 144] Previous studies have demonstrated that the pyridinic N and graphitic N are two of the most important N-species synergistically regulating the activity and selectivity of ORR electrocatalysts, [176] and pyridinic N has great electron-donating ability and metal-coordination capability. [102] Therefore, the large proportion of pyridinic N and graphitic N species in the [emim][DCA] ionic liquid derived samples is beneficial for achieving great catalytic activity towards ORR. After the introduction of metal atom, the peaks of pyridinic N and graphitic N shifted to higher binding energy area because of the metal-N bonding, [177] implying the strong electronic coupling between Fe, Co and N atoms in the carbon matrix. In conclusion, the introduction of nitrogen optimizes the chemical/electronic environment of carbon framework, possibly leading to enhanced catalytic activities of FeCo@NC in ORR/OER processes.[160] The O 1s spectrum fitting curves shown in **Figure 4.9 (c)** present four peaks at 530.0, 531, 532.5, and 533 eV, ascribing to the lattice O (Fe/Co oxide), adsorbed O_2 , adsorbed H_2O or C=O, and O-C-O/N-O, respectively.

Compared with monometallic samples, the content of lattice O in FeCo@NC is much lower which is attributed to the formation of FeCo alloy other than metal oxide.[112]

The Fe 2p and Co 2p spectra (**Figure 4.9 (d), (e)**) are highly complex and show that the metals are in the combination of oxidation state and zero valence. The high susceptibility of metal nanoparticles to oxygen in air atmosphere and low permeability of the X-ray, make it difficult to detect the zero valent Fe and Co in the bulk samples by XPS. [101, 175] In the Fe 2p spectrum, the two peaks at 712 and 725 eV can be assigned to Fe 2p 3/2 and Fe 2p 1/2 of Fe²⁺/Fe³⁺ with the relative satellite peaks of Fe 2p 1/2 at 730 eV and Fe 2p 3/2 at 717 eV, respectively. The proportion of ferrous Fe (Fe²⁺) is relatively increased in FeCo@NC compared with Fe@NC. This observation is significant as it is known that only ferrous iron sites are active sites for ORR, and ferric iron are not.[48] The slight peaks at 708 and 722 eV are evidence for the existence of zero valent Fe in Fe@NC and FeCo@NC. It can be observed that the zero-valence peak of Fe 2p is more intense in FeCo@NC than in Fe@NC, suggesting that Co plays a key role in promoting the transition of oxidative Fe to zero-valent Fe. The Co 2p spectrum displays two peaks at 797 eV and 782 eV, assignable to Co 2p 1/2 and Co 2p 3/2 of Co²⁺/Co³⁺, respectively. And the two satellite peaks at 803 and 787 eV, are assigned to Co 2p 1/2 and Co 2p 3/2, respectively. The peaks at 778 and 793 eV illustrate the presence of the zero-valent Co in the Co@NC and FeCo@NC.

4.3.2. Electrocatalytic Performance toward ORR&OER

To investigate the ORR electrocatalytic activity of the as-obtained FeCo@NC and the control samples of Fe@NC, Co@NC and NC, cyclic voltammetry (CV) and linear sweep

voltammetry (LSV) with rotating disk electrode (RDE) were carried out in alkaline solution (0.1 M KOH).

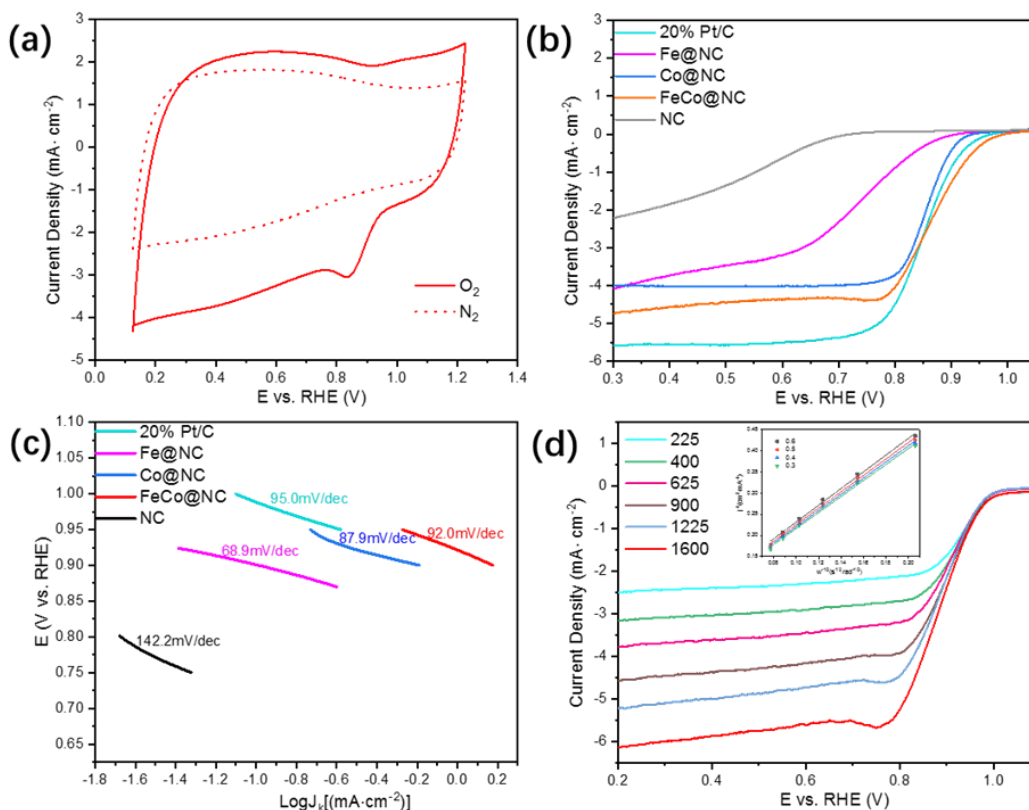


Figure 4.10 ORR performances of FeCo@NC, Fe@NC, Co@NC, NC and 20% Pt/C in O₂-saturated 0.1 m KOH. a) CV curves (solid lines: in O₂-saturated 0.1 m KOH, dashed lines: in N₂-saturated 0.1 M KOH), b) ORR polarization curves, c) corresponding Tafel plot, d) ORR polarization curves of FeCo@NC at various rotation rates in rpm (The inset image is the K–L plots).

As shown in **Figure 4.10 (a)**, the CV curves of FeCo@NC in the O₂-saturated electrolyte exhibits a well-defined cathodic oxygen reduction peak centered at 0.82 V (vs. RHE) whereas no visible peak can be observed in N₂-saturated electrolyte, pronouncing its good ORR catalytic activities. The ORR polarization curves in **Figure 4.10 (b)** shows that FeCo@NC exhibits a dramatically enhanced catalytic activity compared with other samples. It has an onset potential of 0.96 V vs. RHE, a half-wave potential of 0.86 V vs. RHE and a high diffusion-limited current density like the commercial 20%Pt/C. These

values are even superior to the commercial 20% Pt/C ($E_{\text{onset}}=0.94$ V, $E_{1/2}=0.85$ V, $J_{\text{lim}}=5.9$ mA cm⁻²). The well-defined plateau of the diffusion-limiting currents in the ORR polarization curves of FeCo@NC indicates an efficient 4e⁻ dominant ORR catalytic process.[144, 150] The Tafel plots shown in **Figure 4.10 (c)** demonstrate that FeCo@NC has a smaller Tafel slope (92 mV dec⁻¹) than 20% Pt/C (95 mV dec⁻¹), which indicates the fast ORR kinetics of FeCo@NC. The LSV curves of the FeCo@NC were recorded at different rotation speeds to estimate the electron transfer number by using K-L equation (**Figure 4.10 (d)**). The linear K-L plots with parallel fitting lines represent the first-order reaction kinetics subjected to the dissolved oxygen concentration and similar electron-transfer number (n) at various potentials for FeCo@NC electrodes.[162, 178-180] The average electron-transfer number (n) is determined to be 3.95, suggesting a four-electron pathway for ORR.

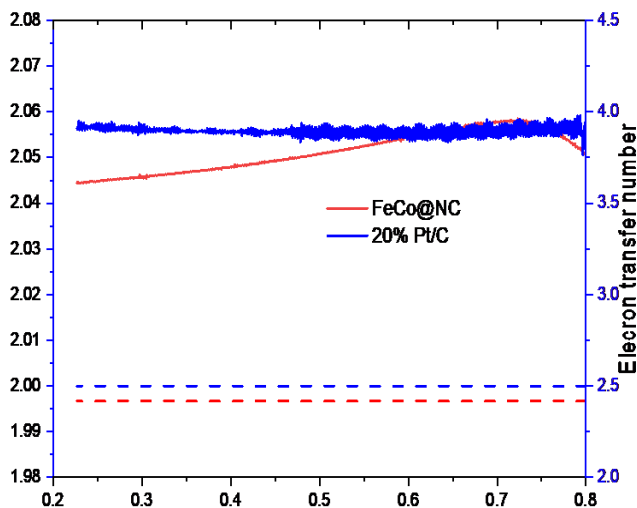


Figure 4.11 H₂O₂% and electron transfer number calculated from RRDE results for comparison of FeCo@NC and 20% Pt/C.

Furthermore, the rotation ring and disk electrode (RRDE) measurements were performed to investigate the H₂O₂ yield and electron transfer number and shown in **Figure**

4.11. The calculated electron transfer number of FeCo@NC varies within a small range of 3.6–4 and yield about 2% H₂O₂ intermediate, compared with both of Pt/C (3.7–3.9, ~2%), respectively. This high electron transfer number and rather low H₂O₂ yield demonstrate the superior electrocatalytic activity and selectivity of FeCo@NC.

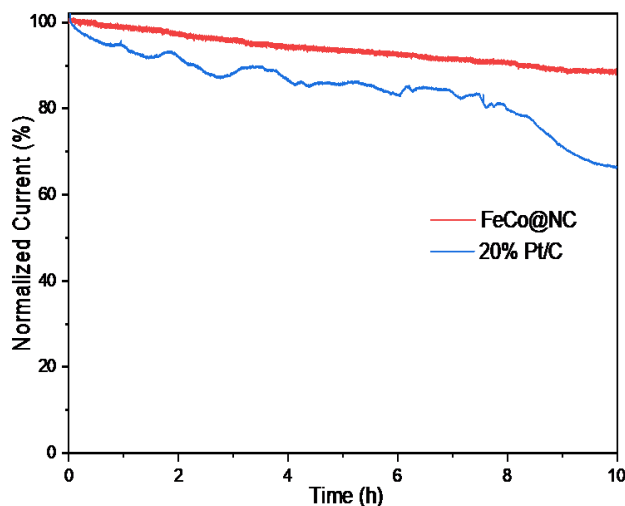


Figure 4.12 Amperometric *i*-*t* curve of FeCo@NC and 20% Pt/C in 0.1 M KOH with 1600 rpm rotation rate.

As shown in **Figure 4.12**, the durability test of FeCo@NC and 20%Pt/C was studied by recording the time-dependent current density curves at the static potential of 0.7 V vs. RHE in O₂ saturated 0.1 M KOH. The FeCo@NC catalyst can maintain its high catalytic activity for the ORR with only 11.8% loss of its initial current after 10 h continuous working, much better than the 33% current loss using the commercial 20% Pt/C catalyst.

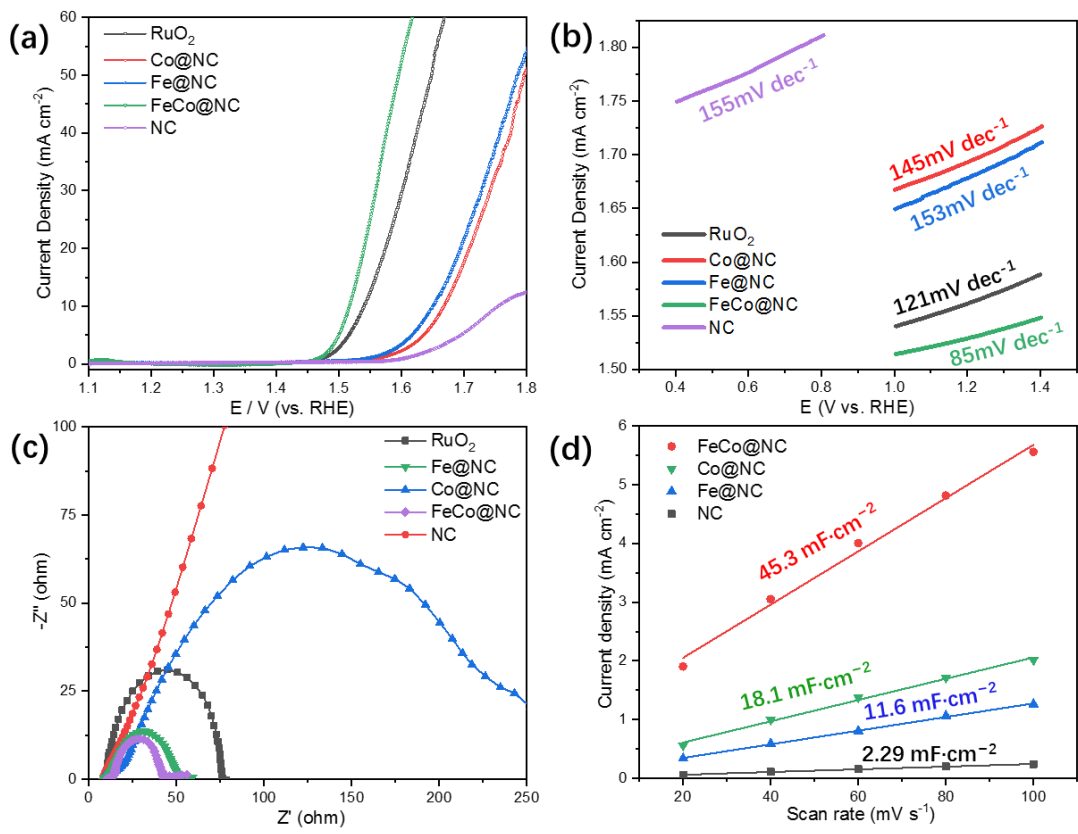


Figure 4.13 OER performance of FeCo@NC, Fe@NC, Co@NC, NC and RuO₂ in 1 M KOH. a) OER polarization curves, b) Tafel plots, c) EIS Nyquist plots, d) Estimation of C_{dl} by plotting the non-faradic capacitance current density variation ($\Delta j = (j_a - j_c)/2$).

The OER catalytic activity of FeCo@NC was investigated by the LSV curves in the alkaline medium of pH = 14 (1 M KOH). For comparison, the OER performance of Fe@NC, Co@NC, NC and commercial RuO₂ were also evaluated by polarization curves under the same conditions. As shown in **Figure 4.13 (a)**, the overpotential of OER at 10 mA·cm⁻² ($\Delta E_{\text{OER}} = E_{j=10 \text{ mA}\cdot\text{cm}^{-2}} - 1.23 \text{ V}$) increases as follows: FeCo@NC (280 mV) < RuO₂ (310 mV) < Fe@NC (410 mV) < Co@NC (430 mV) < NC (520 mV). FeCo@NC exhibits a smaller OER overpotential of 280 mV than commercial RuO₂ (310 mV), indicating the excellent electrocatalytic activity of FeCo@NC for OER. The Tafel plots in **Figure 4.13 (b)** shows faster OER kinetics at the FeCo@NC electrode as indicated by the smaller Tafel slopes

of $85 \text{ mV}\cdot\text{dec}^{-1}$ than that of RuO_2 ($121 \text{ mV}\cdot\text{dec}^{-1}$), Fe@NC ($153 \text{ mV}\cdot\text{dec}^{-1}$), Co@NC ($145 \text{ mV}\cdot\text{dec}^{-1}$), and NC ($155 \text{ mV}\cdot\text{dec}^{-1}$). This agrees with the results shown by the electrochemical impedance spectra (EIS) depicted in **Figure 4.13 (c)** as FeCo@NC has the lowest charge transfer resistance (R_{ct}). As shown in **Figure 4.13 (d)**, the capacitance values of FeCo@NC , Co@NC , Fe@NC and NC were calculated to be 45.3, 18.1, 11.6, and $2.29 \text{ mF}\cdot\text{cm}^{-2}$, showing that FeCo@NC has the highest ECSA value of 755.0 cm^{-2} which vastly exceeds Co@NC (301.7 cm^{-2}), Fe@NC (193.3 cm^{-2}) and NC (38.2 cm^{-2}). This large ECSA implies that FeCo@NC bears the highest active site density for the electrocatalytic OER process.

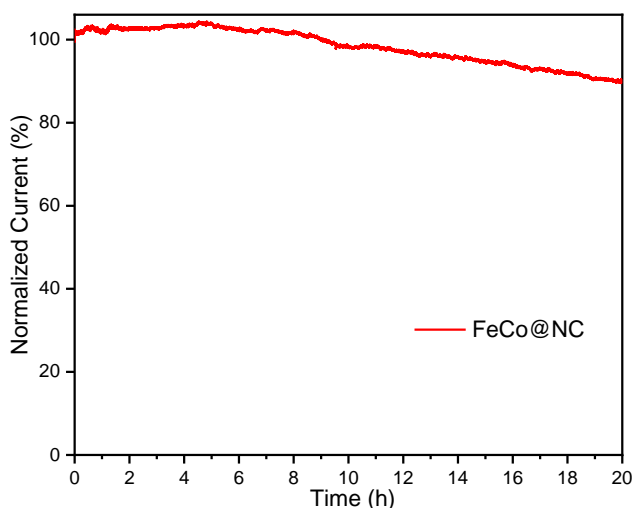


Figure 4.14 Amperometric i-t curve of FeCo@NC holding at 10 mA cm^{-2} .

In addition, the electrochemical stability of the FeCo@NC for OER was evaluated by recording the amperometric i-t curve at 1.53 V vs. RHE. As demonstrated in **Figure 4.14**, FeCo@NC exhibits great durability as it could maintain 90% electrocatalytic activity after 20 h galvanization.

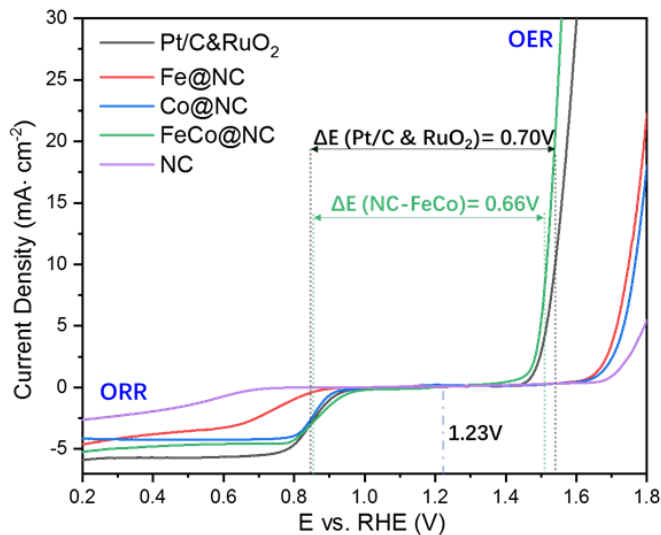


Figure 4.15 Overall polarization curves within the ORR and OER potential window: the value of ΔE for FeCo@NC and 20%Pt/C + RuO₂ ($\Delta E = E_{\text{OER}, j_{10}} - E_{\text{ORR}, j_{-3}}$).

To predict the application of as-prepared electrocatalysts in rechargeable Zn-air batteries, the overall bifunctional catalytic performance was assessed by the potential difference of ΔE ($\Delta E = E_{\text{OER}, j_{10}} - E_{\text{ORR}, j_{-3}}$, where $E_{\text{OER}, j_{10}}$ and $E_{\text{ORR}, j_{-3}}$ are the potentials of OER and ORR at the current densities of 10 and -3 mA·cm⁻², respectively). Theoretically, the smaller ΔE is, the better the comprehensive performance of rechargeable Zn-air batteries. As shown in **Figure 4.15**, FeCo@NC exhibits the smallest ΔE value of 0.66 V among the catalysts reported in this work. Remarkably, this value is smaller than those of the 20% Pt/C + RuO₂ (the weight ratio is 1: 1) with ΔE of 0.70 V, indicates that FeCo@NC can be a promising bifunctional electrocatalysts for rechargeable Zn-air batteries.

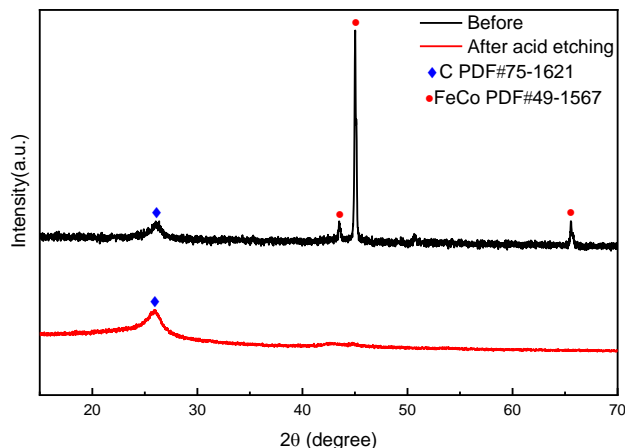


Figure 4.16 XRD patterns of FeCo@NC before and after acid etching.

At last, the origin of active sites in the FeCo@NC was explored by means of acid etching by overnight refluxing in H₂SO₄ solution to remove exposed metallic particles.

As shown in **Figure 4.16**, the XRD pattern of FeCo@NC after acid etching highlights the disappearance of the crystal diffraction peak of FeCo alloy. In addition, ICP-OES (in **Table 4.1**) shows that the content of Fe, Co metal reduce from 26.87% and 28.53% to 0.271% and 0.262%, respectively. These results suggest that FeCo alloy nanoparticles have been eliminated by acid etching.

Table 4.1 ICP-OES elemental analysis of FeCo@NC before and after acid etching.

Sample No.	Fe weight %	Co weight %
FeCo@NC	26.868	28.527
FeCo@NC after acid wash	0.271	0.262

Subsequently, the effects of acid etching over the ORR and OER electrocatalytic activity were investigated by means of LSV and presented in **Figure 4.17**. In contrast to FeCo@NC before acid etching, the loss of FeCo alloy nanoparticles results in largely deteriorated OER performance with 100 mV degradation to reach the current density of 10 mA·cm⁻². However, the acid etching exerts much less influence on the ORR

performance of FeCo@NC due to the small changes of the onset potential and half-wave potential. These results imply that the OER activity vastly depends on FeCo nanoparticles dispersed on carbon matrix, while the unchanged metal-N_x sites and nitrogen-doped carbon that are stably embedded and bonded in carbon matrix are responsible for the ORR activity.

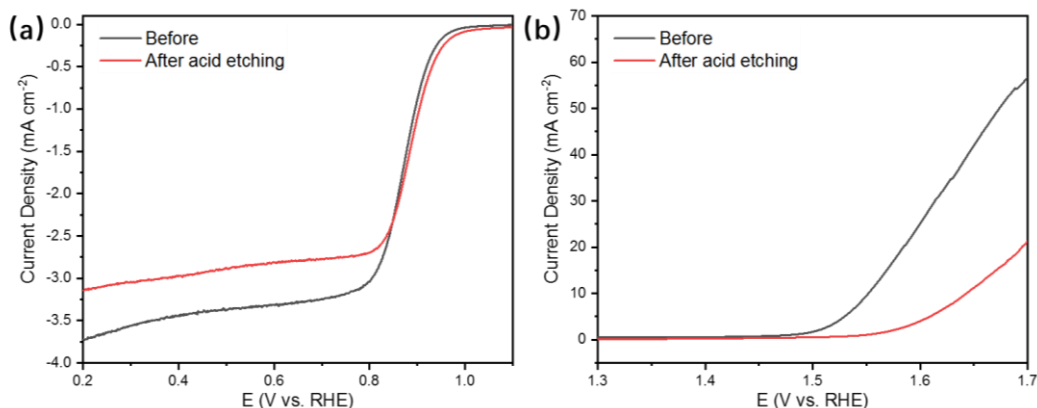


Figure 4.17 The comparisons of (a) ORR polarization curves and (b) OER polarization curves before and after acid wash.

In sum, the physical characterization and the electrochemical tests demonstrate that FeCo@NC represents a highly efficient and stable bifunctional electrocatalyst for the ORR/OER. The superiority of FeCo@NC mainly originates from the following factors: (i) the embedded FeCo alloy nanoparticles have intense coupling effects with the nitrogen-doped carbon which generates rich active sites such as alloy, metal-N_x coordination sites, various nitrogen species and electrical structure modulated carbon atom for catalyzing ORR and OER separately or jointly;[103] (ii) the introduction of FeCo alloys improves the conductivity and crystallinity of the carbon matrix by catalytic graphitization upon high temperature pyrolysis which facilitates the electron transfer in ORR/OER processes;[181] (iii) the highly porous structure of the obtained FeCo@NC provides fast mass transfer in catalytic reaction; (iv) the formation of outer carbon shell efficiently encapsulates the

FeCo alloy nanoparticles in limited space to avoid aggregation and corrosion during the electrochemical reactions, leading to enhanced stability.[101]

4.3.3. Liquid and All-Solid-State Zinc–Air Batteries Performance

Home-made rechargeable liquid ZABs with FeCo@NC as the air electrode were assembled to verify its excellent bifunctional catalytic activities toward OER and ORR in practical applications.

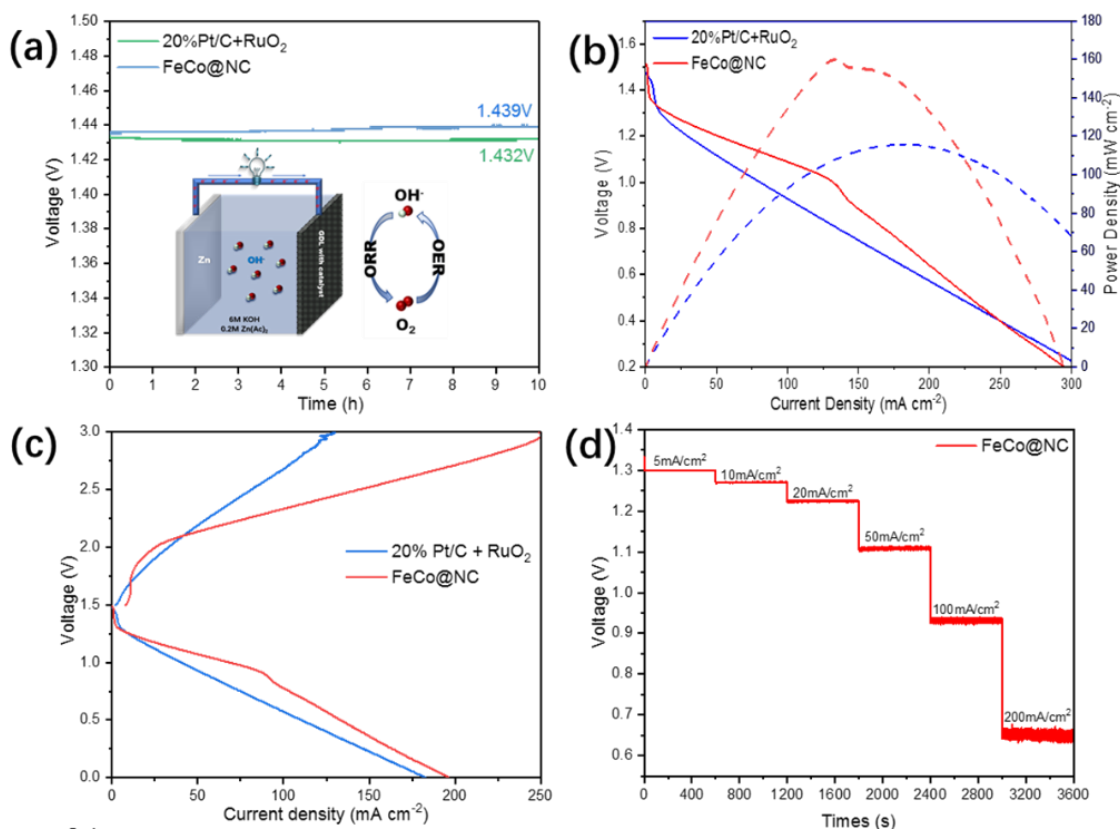


Figure 4.18 a) schematic illustration of the zinc–air battery configuration and OCP measurement of assembled ZAB with FeCo@NC as the air electrodes, b) The discharge polarization curves and power density curves of the ZAB using the FeCo@NC and 20%Pt/C + RuO₂(weight ratio 1:1) air electrodes, c) Charge and discharge polarization curves of FeCo@NC and 20% Pt/C + RuO₂ ZABs. d) Rate capability behaviors of FeCo@NC ZABs ramping from 5 to 200 mA cm⁻²,

The configuration of rechargeable liquid ZABs consists of zinc foil as the anode, alkaline solution containing zinc acetate as the electrolyte, and carbon paper coated with

electrocatalyst as the air electrode (as illustrated in **Figure 4.18 (a)**). For comparison, 20%Pt/C and RuO₂ with weight ratio of 1:1 was employed as the benchmark for accessing the performance of FeCo@NC electrocatalyst. As shown in **Figure 4.18 (a)**, the open-circuit potential (OCP) of the FeCo@NC ZAB is 1.439 V, higher than the 20% Pt/C + RuO₂ ZAB ((OCP=1.432 V). **Figure 4.18 (b)** displays the discharge polarization and power density curves of the ZABs with FeCo@NC and 20%Pt/C + RuO₂. The FeCo@NC ZAB possesses a maximum power density of 160.1 mW · cm⁻² at 179.7 mA·cm⁻², which exceeds the 115.8 mW·cm⁻² at 177.6 mA·cm⁻² of 20%Pt/C + RuO₂ ZAB with the same catalyst loading. **Figure 4.18 (c)** presents the charge and discharge polarization curves of the ZABs with FeCo@NC and 20%Pt/C + RuO₂, respectively. The FeCo@NC ZAB exhibits smaller charging and discharging potential gap than 20%Pt/C + RuO₂ ZAB, suggesting the superior battery reversibility. Apart from that, the FeCo@NC ZAB demonstrates superb rate capability as shown in **Figure 4.18 (d)**. The FeCo@NC ZAB could afford a considerable output voltage of 0.65 V even at the discharge current density as high as 200 mA/cm².

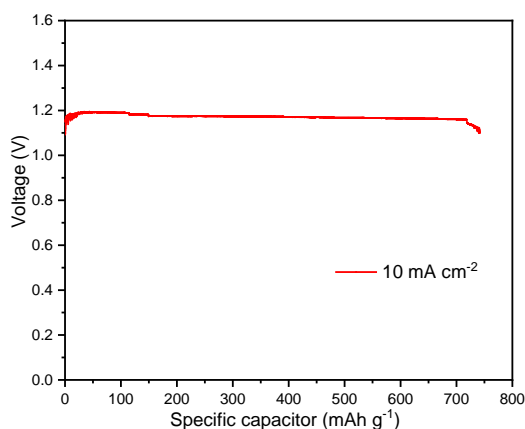


Figure 4.19 Specific capacities of the primary Zn-air battery with FeCo@NC as catalyst.

The specific capacity and corresponding energy density of FeCo@NC ZAB were estimated from the normalized weight of zinc consumption at the discharge current

density of $10 \text{ mA}\cdot\text{cm}^{-2}$ (**Figure 4.19**), which reach up to $741.5 \text{ mAh}\cdot\text{g}^{-1}$ and $830.1 \text{ Wh}\cdot\text{kg}^{-1}$, respectively.

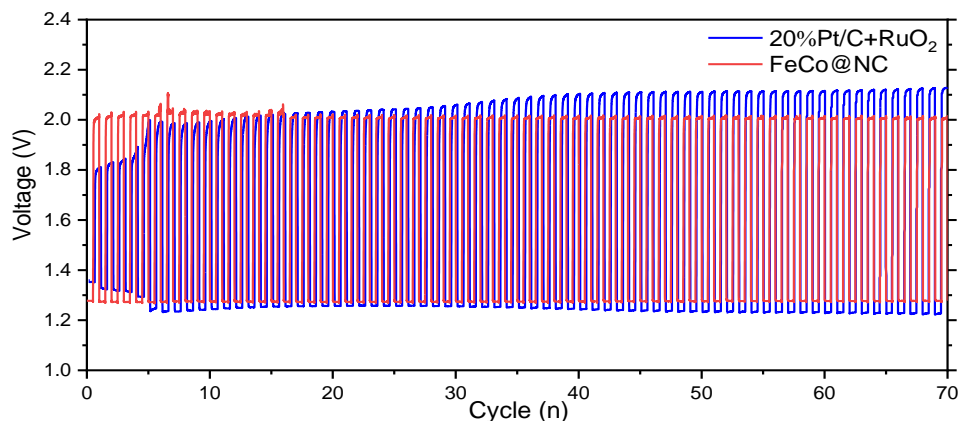


Figure 4.20 The Galvanostatic charge and discharge cycling curves of FeCo@NC and 20% Pt/C + RuO₂ ZABs at $10 \text{ mA}\cdot\text{cm}^{-2}$,

The long life galvanostatic measurements were conducted with the fabricated ZAB by testing the charge and discharge cycling (30 mins charging and 30 mins discharge) at current density of $10 \text{ mA}\cdot\text{cm}^{-2}$ (**Figure 4.20**). It can be observed that the charge and discharge potential gap of FeCo@NC ZAB remained smaller than 20% Pt/C + RuO₂ ZAB after 70 cycles, indicating better degradation tolerance.

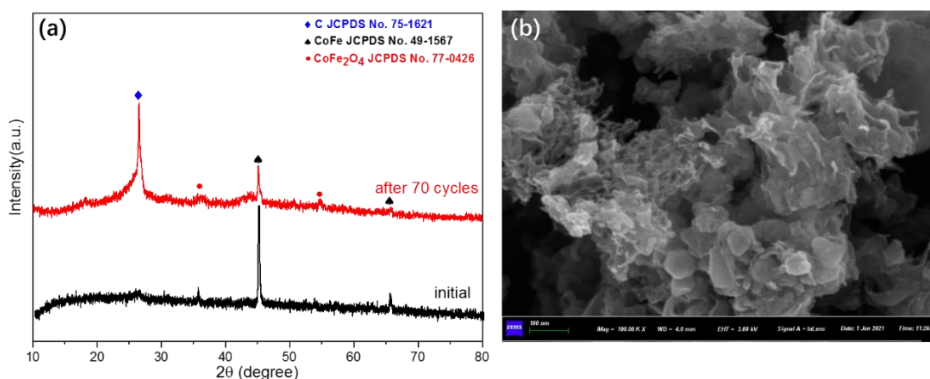


Figure 4.21 a) XRD patterns, b) SEM image of FeCo@NC after 70 galvanostatic recharge cycles.

Only minor changes was observed with composition and morphology of FeCo@NC after long time cycling as shown in **Figure 4.21**, indicating excellent long-term recharge capacity and durability.

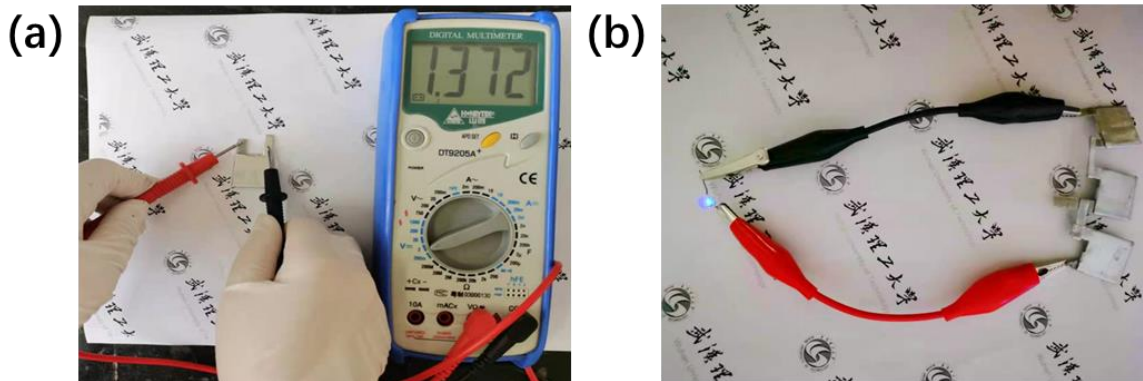


Figure 4.22 a) Photo display of the all-solid-state Zinc–air battery, b) Demonstration of a glowing LED powered by three all-solid-state Zn–air batteries.

The all-solid-state battery was assembled to further examine the performance of the FeCo@NC ZAB. As shown in **Figure 4.22 (a)**, it exhibits an appreciable OCV of 1.372 V. When three FeCo@NC ZABs are connected in series, as exhibited in **Figure 4.22 (b)**, they can lighten a blue light-emitting-diode (LED) lamp bead. These results demonstrate the great potential of FeCo@NC bifunctional electrocatalyst in the high-performance rechargeable Zinc-air battery.

4.4. Conclusion

In this chapter, a facile approach of employing ionic liquids as precursor to in-situ encapsulate FeCo alloy nanoparticles within nitrogen-doped porous carbon framework is proposed, as bifunctional electrocatalyst for ORR and OER. Specifically, the [emim][DCA] was used to promote the dispersion of Fe³⁺ and Co²⁺ ions in precursors, and the co-decomposition during pyrolysis leads to the in-situ formation of FeCo alloy nanoparticles encapsulated within thin shell of nitrogen-doped carbon. Such a core-shell structure promotes the synergistic electronic coupling effect between the FeCo alloy nanoparticles and nitrogen-doped carbon, resulting in improved bifunctional catalytic activity and stability. In addition, the FeCo alloy plays vital role to establish the porous carbon

framework which facilitates the mass transfer in electrochemical process. Consequently, FeCo@NC exhibits high-efficiency electrocatalytic activity for both ORR and OER and robust stability in alkaline environments. Especially, the half-wave potential ($E_{1/2}$) for ORR is 0.86 V, superior to commercial 20%Pt/C catalysts, and the overpotential (E_{over}) for OER is only 280 mV to reach the current density of $10 \text{ mA} \cdot \text{cm}^{-2}$. As a result, the ΔE ($\Delta E = E_{\text{OER}, j_{10}} - E_{\text{ORR}, j_{-3}}$) is calculated to be an impressive value of 0.66 V that surpasses 20% Pt/C-RuO₂ noble metal ($\Delta E = 0.70 \text{ V}$) as benchmark. Furthermore, FeCo@NC also displays high efficiency with great durability when applied in liquid and all-solid-state zinc–air batteries. The peak power density of a FeCo@NC-based rechargeable Zn-air battery reaches values as high as $160 \text{ mW} \cdot \text{cm}^{-2}$ at $180 \text{ mA} \cdot \text{cm}^{-2}$. The specific capacity and corresponding energy density at the discharge current density of $10 \text{ mA} \cdot \text{cm}^{-2}$ reach up to $741.5 \text{ mAh} \cdot \text{g}^{-1}$ and $830.1 \text{ Wh} \cdot \text{kg}^{-1}$, respectively. The excellent Zn-air battery performance may hold the promise for large-scale application. Last, it is anticipated that this facile and scalable strategy may open up a new avenue to develop alloy coupled with heteroatom-doped porous carbon as multi-functional electrocatalyst for other energy conversion systems.

Chapter 5

5. Conclusions and Outlooks

5.1. Conclusions

Developing non-noble metal-based catalysts with low cost, high activity, and good stability is one of the top priorities to hasten the wide application of fuel cells and metal-air batteries. In this thesis, an ionic-liquids strategy was employed to synthesize highly efficient carbon-based electrocatalysts for ORR, highlighting the regulation of active sites density, construction of hierarchical porous structures, and design of bimetallic active centers. With physicochemical characterization and electrochemical measurements, the following conclusions were obtained:

- ❖ We have employed [emim][DCA] as precursor to prepare N-CNTs composite materials as highly efficient ORR electrocatalysts. Iron and cobalt salts have been adopted as FeCo alloy catalyst precursors in the carbonization process to promote the graphitization of carbon products. During the pyrolysis process, iron and cobalt ions are annealed into FeCo alloy nanoparticles under the reducing atmosphere of the carbothermal reaction; these FeCo alloy nanoparticles then catalyze the growth of N-CNTs from the volatile product of IL in the presence of silica template.

It was found that the silica template prevented the face-face stacking of the formed carbon materials and downsized the FeCo alloy nanoparticles, which promoted the growth of N-CNTs. Moreover, the involvement of silica rendered the carbon-based electrocatalysts with a large specific surface area, proper pore size distribution, and effective doping, facilitating mass transport and electron transfer in the electrochemical reaction. This work demonstrates that the presence of silica template can promote the formation of N-CNTs in ionic liquids carbonization, which inspires a new approach for N-CNTs preparation.

- ❖ We have proposed [emim][DCA] as precursor to in-situ encapsulate FeCo alloy nanoparticles within nitrogen-doped porous carbon framework, as bifunctional electrocatalyst for ORR and OER. The co-decomposition of [emim][DCA] and metal salts during pyrolysis leads to the in-situ formation of FeCo alloy nanoparticles encapsulated within thin shell of nitrogen-doped carbon. Such a core-shell structure promotes the synergistic electronic coupling effect between the FeCo alloy nanoparticles and nitrogen-doped carbon, resulting in improved bifunctional catalytic activity and stability. The as-prepared FeCo@NC exhibited high activity for ORR and OER and robust stability in alkaline environments. Furthermore, FeCo@NC also displayed high efficiency with great durability when applied in liquid and all-solid-state zinc–air batteries. This work provided a facile and scalable strategy that may open up a new avenue to develop alloy-coupled heteroatom-doped porous carbon as multi-functional electrocatalyst for other energy conversion systems.

5.2. Outlook

Although ionic liquids have been recognized as effective carbon precursors to prepare highly efficient carbon-based ORR electrocatalysts, much still remains to be resolved regarding the following aspects:

- ❖ The knowledge on the carbonization processes of various ionic liquids and the formation of active centers are not sufficient, which constrains the rational control on the structures and compositions of ORR catalysts derived from ionic liquids.
- ❖ The factors of electrical conductivity, specific surface area, hierarchical pore structure, and defects can directly affect the ORR performance, so the relationship between catalyst morphology and electronic structure should be investigated to optimize the ORR catalysts.
- ❖ Novel synthesis techniques with ionic liquids need to be developed to realize the large-scale production of ideal ORR catalysts.

6. References

- [1] International Energy Agency. World Energy Outlook 2021[Electronic version] (2021).
- [2] M.K. Debe, Nature 486 (2012) 43-51.
- [3] A. Kulkarni, S. Siahrostami, A. Patel, J.K. Nørskov, Chem. Rev. 118 (2018) 2302-2312.
- [4] F. Jaouen, J. Dodelet, J. Phys. Chem. C 113 (2009) 15422-15432.
- [5] X. Lu, B.Y. Xia, S. Zang, X. Lou, Angew. Chem. Int. Ed. 59 (2020) 4634-4650.
- [6] J. Nørskov, J. Rossmeisl, A. Logadottir, L. Lindqvist, J. Kitchin, T. Bligaard, H. Jonsson, J. Phys. Chem. B 108 (2004) 17886-17892.
- [7] Yaobing Wang, et al, Electrocatalysis in Balancing the Natural Carbon Cycle, (2021) 391-419.
- [8] Z. Wang, X. Yao, Y. Kang, L. Miao, D. Xia, L. Gan, Adv. Funct. Mater. 29 (2019) 1902987.
- [9] M. Li, Z. Zhao, T. Cheng, A. Fortunelli, C. Chen, R. Yu, Q. Zhang, L. Gu, B. Merinov, Z. Lin, E. Zhu, T. Yu, Q. Jia, J. Guo, L. Zhang, W. Goddard, Y. Huang, X. Duan, Science 354 (2016) 1414-1419.
- [10] W. Xia, A. Mahmood, Z. Liang, R. Zou, S. Guo, Angew. Chem. Int. Ed. 55 (2016) 2650-2676.
- [11] Y. Nie, L. Li, Z. Wei, Chem. Soc. Rev. 44 (2015) 2168-2201.
- [12] A. Morozan, B. Jusselme, S. Palacin, Energy Environ. Sci. 4 (2011) 1238-1254.
- [13] C. Hu, L. Dai, Adv. Mater. 31 (2018) 1804672.
- [14] L. Zhang, Z. Xia, J. Phys. Chem. C 115 (2011) 11170-11176.

- [15] Z. Zhao, M. Li, L. Zhang, L. Dai, Z. Xia, *Adv. Mater.* 27 (2015) 6834-6840.
- [16] K. Gong, F. Du, Z. Xia, M. Durstock, L. Dai, *Science* 323 (2009) 760-764.
- [17] K. Gao, B. Wang, L. Tao, B.V. Cunnning, Z. Zhang, S. Wang, R.S. Ruoff, L. Qu, *Adv. Mater.* 31 (2018) 1805121.
- [18] D. Guo, R. Shibuya, C. Akiba, S. Saji, T. Kondo, J. Nakamura, *Science* 351 (2016) 361-365.
- [19] H. Kim, K. Lee, S.I. Woo, Y. Jung, *PCCP* 13 (2011) 17505.
- [20] J. Zhang, Z. Xia, L. Dai, *Sci. Adv.* 1 (2015) 1500564.
- [21] J. Zhang, L. Qu, G. Shi, J. Liu, J. Chen, L. Dai, *Angew. Chem. Int. Ed.* 55 (2015) 2230-2234.
- [22] C. Yang, H. Jin, C. Cui, J. Li, J. Wang, K. Amine, J. Lu, S. Wang, *Nano Energy* 54 (2018) 192-199.
- [23] J. Gao, N. Ma, J. Tian, C. Shen, L. Wang, P. Yu, Y. Chu, W. Liu, X. Tan, X. Li, Z. Yin, *J. Solid State Electrochem.* 22 (2017) 519-525.
- [24] S. Wang, E. Iyyamperumal, A. Roy, Y. Xue, D. Yu, L. Dai, *Angew. Chem. Int. Ed.* 50 (2011) 11756-11760.
- [25] S. Wang, L. Zhang, Z. Xia, A. Roy, D. Chang, J. Baek, L. Dai, *Angew. Chem. Int. Ed.* 51 (2012) 4209-4212.
- [26] Y. Zheng, Y. Jiao, L. Ge, M. Jaroniec, S. Qiao, *Angew. Chem. Int. Ed.* 52 (2013) 3110-3116.
- [27] K. Qu, Y. Zheng, Y. Jiao, X. Zhang, S. Dai, S. Qiao, *Adv. Energy Mater.* 7 (2017) 1602068.
- [28] J. Zhang, Z. Zhao, Z. Xia, L. Dai, *Nat. Nanotechnol.* 10 (2015) 444-452.

- [29] L. Liu, M. Qing, Y. Wang, S. Chen, *J. Mater. Sci. Technol.* 31 (2015) 599-606.
- [30] A. Castro Neto, F. Guinea, N. Peres, K. Novoselov, A. Geim, *Rev. Mod. Phys.* 81 (2009) 109-162.
- [31] X. Yan, Y. Jia, X. Yao, *Chem. Soc. Rev.* 47 (2018) 7628-7658.
- [32] H. Zhao, C. Sun, Z. Jin, D. Wang, X. Yan, Z. Chen, G. Zhu, X. Yao, *J. Mater. Chem. A* 3 (2015) 11736-11739.
- [33] A. Shen, Y. Zou, Q. Wang, R. Dryfe, X. Huang, S. Dou, L. Dai, S. Wang, *Angew. Chem. Int. Ed.* 53 (2014) 10804-10808.
- [34] R. Jasinski, *Nature* (1964) 1212-1213.
- [35] S. Jahnke H, Zimmermann G. , *Top. Curr. Chem.* (1976) 133-181.
- [36] H. Alt, H. Binder, G. Sandstede, *J. Catal.* 28 (1973) 8-19.
- [37] S. Gupta, D. Tryk, I. Bae, W. Aldred, E. Yeager, *J. Appl. Electrochem.* 19 (1989) 19-27.
- [38] G. Wu, P. Zelenay, *Acc. Chem. Res.* 46 (2013) 1878-1889.
- [39] E. Proietti, F. Jaouen, M. Lefèvre, N. Larouche, J. Tian, J. Herranz, J.-P. Dodelet, *Nat. Commun.* 2 (2011) 1-9.
- [40] S. Hou, R. Kluge, R. Haid, E. Gubanov, S. Watzele, A. Bandarenka, B. Garlyyev, *ChemElectroChem* 8 (2021) 3433-3456.
- [41] M. Lefèvre, J. Dodelet, P. Bertrand, *J. Phys. Chem. B* 106 (2002) 8705-8713.
- [42] U. Kramm, J. Herranz, N. Larouche, T. Arruda, M. Lefèvre, F. Jaouen, P. Bogdanoff, S. Fiechter, I. Abs-Wurmbach, S. Mukerjee, *PCCP* 14 (2012) 11673-11688.
- [43] A. Zitolo, V. Goellner, V. Armel, M. Sougrati, T. Mineva, L. Stievano, E. Fonda, F. Jaouen, *Nat. Mater.* 14 (2015) 937-942.

- [44] J. Li, S. Ghoshal, W. Liang, M. Sougrati, F. Jaouen, B. Halevi, S. McKinney, G. McCool, C. Ma, X. Yuan, *Energy Environ. Sci.* 9 (2016) 2418-2432.
- [45] J. Zagal, M. Koper, *Angew. Chem. Int. Ed.* 55 (2016) 14510-14521.
- [46] Y. Ye, H. Li, F. Cai, C. Yan, R. Si, S. Miao, Y. Li, G. Wang, X. Bao, *ACS Catal.* 7 (2017) 7638-7646.
- [47] Y. He, S. Liu, C. Priest, Q. Shi, G. Wu, *Chem. Soc. Rev.* 49 (2020) 3484-3524.
- [48] U.I. Kramm, I. Herrmann-Geppert, J. Behrends, K. Lips, S. Fiechter, P. Bogdanoff, *J. Am. Chem. Soc.* 138 (2016) 635-640.
- [49] X. Chen, L. Yu, S. Wang, D. Deng, X. Bao, *Nano Energy* 32 (2017) 353-358.
- [50] H. Chung, D.A. Cullen, D. Higgins, B. Sneed, E. Holby, K. More, P. Zelenay, *Science* 357 (2017) 479-484.
- [51] J. Wu, H. Zhou, Q. Li, M. Chen, J. Wan, N. Zhang, L. Xiong, S. Li, B.Y. Xia, G. Feng, *Adv. Energy Mater.* 9 (2019) 1900149.
- [52] L. Yang, L. Shi, D. Wang, Y. Lv, D. Cao, *Nano Energy* 50 (2018) 691-698.
- [53] J. Li, M. Chen, D. Cullen, S. Hwang, M. Wang, B. Li, K. Liu, S. Karakalos, M. Lucero, H. Zhang, *Nat. Catal.* 1 (2018) 935-945.
- [54] H. Shang, Z. Jiang, D. Zhou, J. Pei, Y. Wang, J. Dong, X. Zheng, J. Zhang, W. Chen, *Chem. Sci.* 11 (2020) 5994-5999.
- [55] F. Li, G. Han, H. Noh, S. Kim, Y. Lu, H. Jeong, Z. Fu, J. Baek, *Energy Environ. Sci.* 11 (2018) 2263-2269.
- [56] H. Yu, A. Fisher, D. Cheng, D. Cao, *ACS Appl. Mater. Interfaces* 8 (2016) 21431-21439.

- [57] Z. Cai, P. Du, W. Liang, H. Zhang, P. Wu, C. Cai, Z. Yan, J. Mater. Chem. A 8 (2020) 15012-15022.
- [58] F. Luo, J. Zhu, S. Ma, M. Li, R. Xu, Q. Zhang, Z. Yang, K. Qu, W. Cai, Z. Chen, Energy Storage Mater. 35 (2021) 723-730.
- [59] P. Song, M. Luo, X. Liu, W. Xing, W. Xu, Z. Jiang, L. Gu, Adv. Funct. Mater. 27 (2017) 1700802.
- [60] J. Li, S. Chen, N. Yang, M. Deng, S. Ibraheem, J. Deng, J. Li, L. Li, Z. Wei, Angew. Chem. Int. Ed. 58 (2019) 7035-7039.
- [61] X. Sun, K. Li, C. Yin, Y. Wang, M. Jiao, F. He, X. Bai, H. Tang, Z. Wu, Carbon 108 (2016) 541-550.
- [62] C. Zhu, Q. Shi, B. Xu, S. Fu, G. Wan, C. Yang, S. Yao, J. Song, H. Zhou, D. Du, Adv. Energy Mater. 8 (2018) 1801956.
- [63] H. Shen, E. Gracia-Espino, J. Ma, H. Tang, X. Mamat, T. Wagberg, G. Hu, S. Guo, Nano Energy 35 (2017) 9-16.
- [64] X. Hai, X. Zhao, N. Guo, C. Yao, C. Chen, W. Liu, Y. Du, H. Yan, J. Li, Z. Chen, ACS Catal. 10 (2020) 5862-5870.
- [65] S. Wang, Q. He, C. Wang, H. Jiang, C. Wu, S. Chen, G. Zhang, L. Song, Small 14 (2018) 1800128.
- [66] X. Liu, L. Wang, P. Yu, C. Tian, F. Sun, J. Ma, W. Li, H. Fu, Angew. Chem. Int. Edit. 49 (2018) 16166-16170.
- [67] Y. Hu, J. Jensen, W. Zhang, L. Cleemann, W. Xing, N. Bjerrum, Q. Li, Angew. Chem. 126 (2014) 3749-3753.
- [68] H. Yin, C. Zhang, F. Liu, Y. Hou, Adv. Funct. Mater. 24 (2014) 2930-2937.

- [69] J. Zhu, M. Xiao, C. Liu, J. Ge, J. St-Pierre, W. Xing, *J. Mater. Chem. A* 3 (2015) 21451-21459.
- [70] Y. Hu, J. Jensen, W. Zhang, L. Cleemann, W. Xing, N. Bjerrum, Q. Li, *Angew. Chem. Int. Ed. Engl.* 53 (2014) 3675-3679.
- [71] D. Deng, L. Yu, X. Chen, G. Wang, L. Jin, X. Pan, J. Deng, G. Sun, X. Bao, *Angew. Chem. Int. Ed.* 52 (2013) 371-375.
- [72] M. Tavakkoli, T. Kallio, O. Reynaud, A. Nasibulin, C. Johans, J. Sainio, H. Jiang, E. Kauppinen, K. Laasonen, *Angew. Chem. Int. Ed.* 54 (2015) 4535-4538.
- [73] X. Sun, P. Wei, S. Gu, J. Zhang, Z. Jiang, J. Wan, Z. Chen, L. Huang, Y. Xu, C. Fang, *Small* 16 (2020) 1906057.
- [74] W. Jiang, L. Gu, L. Li, Y. Zhang, X. Zhang, L. Zhang, J. Wang, J. Hu, Z. Wei, L. Wan, *J. Am. Chem. Soc.* 138 (2016) 3570-3578.
- [75] M. Chen, M. Zhu, M. Zuo, S. Chu, J. Zhang, Y. Wu, H. Liang, X. Feng, *Angew. Chem.* 132 (2020) 1644-1650.
- [76] M. Watanabe, M. Thomas, S. Zhang, K. Ueno, T. Yasuda, K. Dokko, *Chem. Rev.* 117 (2017) 7190-7239.
- [77] S. Zhang, K. Dokko, M. Watanabe, *Mater. Horiz.* 2 (2015) 168-197.
- [78] X. Cui, Q. Yang, Y. Xiong, Z. Bao, H. Xing, S. Dai, *Chem. Commun.* 53 (2017) 4915-4918.
- [79] Y. Men, M. Siebenbürger, X. Qiu, M. Antonietti, J. Yuan, *J. Mater. Chem. A* 1 (2013) 11887.
- [80] B. Qiu, C. Pan, W. Qian, Y. Peng, L. Qiu, F. Yan, *J. Mater. Chem. A* 1 (2013) 6373-6378.

- [81] A. Fuertes, M. Sevilla, *Carbon* 94 (2015) 41-52.
- [82] W. Qian, J. Texter, F. Yan, *Chem. Soc. Rev.* 46 (2017) 1124-1159.
- [83] D. Xu, J. Guo, F. Yan, *Prog. Polym. Sci.* 79 (2018) 121-143.
- [84] T. Fellingner, A. Thomas, J. Yuan, M. Antonietti, *Adv. Mater.* 25 (2013) 5838-5854.
- [85] J. Paraknowitsch, A. Thomas, *Macromol. Chem. Phys.* 213 (2012) 1132-1145.
- [86] J. Lee, X. Wang, H. Luo, G. Baker, S. Dai, *J. Am. Chem. Soc.* 131 (2009) 4596-4597.
- [87] Y. She, Z. Lu, M. Ni, L. Li, M. Leung, *ACS Appl. Mater. Interfaces* 7 (2015) 7214-7221.
- [88] Z. Jin, A. Lu, Y.Y. Xu, J. Zhang, W. Li, *Adv. Mater.* 26 (2014) 3700-3705.
- [89] W. Yang, T. Fellingner, M. Antonietti, *J. Am. Chem. Soc.* 133 (2011) 206-209.
- [90] Z. Zhang, G. Veith, G. Brown, P. Fulvio, P. Hillesheim, S. Dai, S. Overbury, *Chem. Commun.* 50 (2014) 1469-1471.
- [91] Z. Cui, S. Wang, Y. Zhang, M. Cao, *J. Power Sources* 259 (2014) 138-144.
- [92] H. Wu, L. Shi, J. Lei, D. Liu, D. Qu, Z. Xie, X. Du, P. Yang, X. Hu, J. Li, *J. Power Sources* 323 (2016) 90-96.
- [93] W. Yang, X. Yue, X. Liu, J. Zhai, J. Jia, *Nanoscale* 7 (2015) 11956-11961.
- [94] N. Ranjbar Sahraie, J. Paraknowitsch, C. Göbel, A. Thomas, P. Strasser, *J. Am. Chem. Soc.* 136 (2014) 14486-14497.
- [95] K. Elumeeva, N. Fechler, T. Fellingner, M. Antonietti, *Mater. Horiz.* 1 (2014) 588-594.
- [96] J. Wang, Z. Xu, Y. Gong, C. Han, H. Li, Y. Wang, *ChemCatChem* 6 (2014) 1204-1209.

- [97] T. Fellingner, D. Su, M. Engenhorst, D. Gautam, R. Schlögl, M. Antonietti, *J. Mater. Chem.* 22 (2012) 23996-24005.
- [98] Y. Sa, C. Park, H. Jeong, S. Park, Z. Lee, K. Kim, G. Park, S. Joo, *Angew. Chem.* 126 (2014) 4186-4190.
- [99] Y. Qian, P. Du, P. Wu, C. Cai, D.F. Gervasio, *J. Phys. Chem. C* 120 (2016) 9884-9896.
- [100] Y. Qian, Z. Liu, H. Zhang, P. Wu, C. Cai, *ACS Appl. Mater. Interfaces* 8 (2016) 32875-32886.
- [101] C. Li, M. Wu, R. Liu, *Appl. Catal. B* 244 (2019) 150-158.
- [102] Z. Wang, J. Ang, B. Zhang, Y. Zhang, X. Ma, T. Yan, J. Liu, B. Che, Y. Huang, X. Lu, *Appl. Catal. B* 254 (2019) 26-36.
- [103] Y. Wu, X. Wu, T. Tu, P. Zhang, J. Li, Y. Zhou, L. Huang, S. Sun, *Appl. Catal. B* 278 (2020).
- [104] Q. Xu, H. Jiang, Y. Li, D. Liang, Y. Hu, C. Li, *Appl. Catal. B* 256 (2019) 117893.
- [105] J. Gao, L. Wang, P. Zhu, X. Zhao, G. Wang, S. Liu, *J. Alloys Compd.* 870 (2021) 159417.
- [106] D. Deng, Y. Tian, H. Li, L. Xu, J. Qian, J. Pang, B. Wang, Q. Zhang, H. Li, *J. Alloys Compd.* 797 (2019) 1041-1049.
- [107] Z. Li, G. Li, L. Jiang, J. Li, G. Sun, C. Xia, F. Li, *Angew. Chem. Int. Ed.* 54 (2015) 1494-1498.
- [108] F. He, X. Chen, Y. Shen, Y. Li, A. Liu, S. Liu, T. Mori, Y. Zhang, *J. Mater. Chem. A* 4 (2016) 6630-6638.
- [109] S. Liu, S. Chen, *Carbon* 105 (2016) 282-290.

- [110] K. Lim, H. Kim, *Appl. Catal. B* 158 (2014) 355-360.
- [111] C. Su, H. Cheng, W. Li, Z. Liu, N. Li, Z. Hou, F. Bai, H. Zhang, T. Ma, *Adv. Energy Mater.* 7 (2017) 1602420.
- [112] X. Hao, Z. Jiang, B. Zhang, X. Tian, C. Song, L. Wang, T. Maiyalagan, X. Hao, Z. Jiang, *Adv. Sci.* 8 (2021) 2004572.
- [113] Z. Wang, X. Zhou, H. Jin, D. Chen, J. Zhu, R. Hempelmann, L. Chen, S. Mu, *J. Alloys Compd.* 908 (2022) 164565.
- [114] F. Zheng, G. Mu, Z. Zhang, Y. Shen, M. Zhao, G. Pang, *Mater. Lett.* 68 (2012) 453-456.
- [115] S. Soll, T. Fellingner, X. Wang, Q. Zhao, M. Antonietti, J. Yuan, *Small* 9 (2013) 4135-4141.
- [116] Y. She, J. Chen, C. Zhang, Z. Lu, M. Ni, P. Sit, M. Leung, *Energy Procedia* 142 (2017) 1319-1326.
- [117] R. Morris, *Chem Commun (Camb)* (2009) 2990-2998.
- [118] P. Fulvio, J. Lee, R. Mayes, X. Wang, S. Mahurin, S. Dai, *PCCP* 13 (2011) 13486-13491.
- [119] Z. Xie, D. Su, *Eur. J. Inorg. Chem.* (2015) 1137-1147.
- [120] J. Le Bideau, L. Viau, A. Vioux, *Chem. Soc. Rev.* 40 (2011) 907-925.
- [121] A. Chen, Y. Yu, H. Lv, Y. Wang, S. Shen, Y. Hu, B. Li, Y. Zhang, J. Zhang, *J. Mater. Chem. A* 1 (2013) 1045-1047.
- [122] K. Elumeeva, N. Fechler, T. Fellingner, M. Antonietti, *Mater. Horiz.* 1 (2014) 588-594.

- [123] X. Ge, A. Sumboja, D. Wu, T. An, B. Li, F.W.T. Goh, T.S.A. Hor, Y. Zong, Z. Liu, *ACS Catal.* 5 (2015) 4643-4667.
- [124] A. Bard, J. Faulkner, *Electrochemical Methods: Fundamental and Applications*, 2nd ed., John Wiley & Sons, New York, 2001.
- [125] M. Pegis, C. Wise, D. Martin, J. Mayer, *Chem. Rev.* 118 (2018) 2340-2391.
- [126] D. Higgins, P. Zamani, A. Yu, Z. Chen, *Energy Environ. Sci.* 9 (2016) 357-390.
- [127] G. Wu, K. More, C. Johnston, P. Zelenay, *Science* 332 (2011) 443-447.
- [128] Z. Chen, D. Higgins, Z. Chen, *Carbon* 48 (2010) 3057-3065.
- [129] L. Feng, Y. Yan, Y. Chen, L. Wang, *Energy Environ. Sci.* 4 (2011) 1892-1899.
- [130] Q. Wei, X. Tong, G. Zhang, J. Qiao, Q. Gong, S. Sun, *Catalysts* 5 (2015) 1574-1602.
- [131] E. Nxumalo, N. Coville, *Materials* 3 (2010) 2141-2171.
- [132] J. Meng, C. Niu, L. Xu, J. Li, X. Liu, X. Wang, Y. Wu, X. Xu, W. Chen, Q. Li, *J. Am. Chem. Soc.* 139 (2017) 8212-8221.
- [133] B. Qiu, C. Pan, W. Qian, Y. Peng, L. Qiu, F. Yan, *J. Mater. Chem. A* 1 (2013) 6373-6378.
- [134] Z. Li, G. Li, L. Jiang, J. Li, G. Sun, C. Xia, F. Li, *Angew. Chem. Int. Ed.* 54 (2015) 1494-1498.
- [135] J. Paraknowitsch, O. Sukhbat, Y. Zhang, A. Thomas, *Eur. J. Inorg. Chem.* 2012 (2012) 4105-4116.
- [136] T. van Deelen, C. Hernández Mejía, K. de Jong, *Nat. Catal.* 2 (2019) 955-970.
- [137] R. McDonald, *J. Am. Chem. Soc.* 79 (1957) 850-854.

- [138] H. Zhong, J. Wang, Q. Zhang, F. Meng, D. Bao, T. Liu, X. Yang, Z. Chang, J. Yan, X. Zhang, *Adv. Sustain. Syst.* 1 (2017) 1700020.
- [139] H. Zhong, J. Wang, Q. Zhang, F. Meng, D. Bao, T. Liu, X. Yang, Z. Chang, J. Yan, X. Zhang, *Adv. Sustain. Syst.* 1 (2017) 1700020.
- [140] C. Yang, S. Shang, Q. Gu, J. Shang, X. Li, *J. Energy Chem.* 66 (2022) 306-313.
- [141] Z. Sheng, L. Shao, J. Chen, W. Bao, F. Wang, X. Xia, *ACS Nano* 5 (2011) 4350-4358.
- [142] J. Liang, Y. Jiao, M. Jaroniec, S.Z. Qiao, *Angew. Chem. Int. Ed.* 51 (2012) 11496-11500.
- [143] L. Lai, J.R. Potts, D. Zhan, L. Wang, C.K. Poh, C. Tang, H. Gong, Z. Shen, J. Lin, R.S. Ruoff, *Energy Environ. Sci.* 5 (2012) 7936-7942.
- [144] H. Zhong, J. Wang, Y. Zhang, W. Xu, W. Xing, D. Xu, Y. Zhang, X. Zhang, *Angew. Chem. Int. Ed.* 53 (2014) 14235-14239.
- [145] M. Thommes, K. Kaneko, A. Neimark, J. Olivier, F. Rodriguez-Reinoso, J. Rouquerol, K. Sing, *Pure Appl. Chem.* 87 (2015) 1051-1069.
- [146] B. Li, F. Dai, Q. Xiao, L. Yang, J. Shen, C. Zhang, M. Cai, *Energy Environ. Sci.* 9 (2016) 102-106.
- [147] E. Mansfield, A. Kar, S.A. Hooker, *Anal. Bioanal. Chem.* 396 (2009) 1071-1077.
- [148] Y. Murakami, Y. Miyauchi, S. Chiashi, S. Maruyama, *Chem. Phys. Lett.* 374 (2003) 53-58.
- [149] C. Choi, S. Park, S. Woo, *J. Mater. Chem.* 22 (2012) 12107-12115.
- [150] Y. Li, W. Zhou, H. Wang, L. Xie, Y. Liang, F. Wei, J. Idrobo, S.J. Pennycook, H. Dai, *Nat. Nanotechnol.* 7 (2012) 394-400.

- [151] W. Chen, Q. Xiang, T. Peng, C. Song, W. Shang, T. Deng, J. Wu, *iScience* 23 (2020) 101532.
- [152] K. Szwabińska, G. Lota, *ChemElectroChem* 8 (2021) 839-849.
- [153] A. Kraytsberg, Y. Ein-Eli, *Nano Energy* 2 (2013) 468-480.
- [154] Y. Li, M. Gong, Y. Liang, J. Feng, J. Kim, H. Wang, G. Hong, B. Zhang, H. Dai, *Nat. Commun.* 4 (2013).
- [155] J. Lee, S. Kim, R. Cao, N. Choi, M. Liu, K. Lee, J. Cho, *Adv. Energy Mater.* 1 (2011) 34-50.
- [156] W. Fang, J. Zhao, W. Zhang, P. Chen, Z. Bai, M. Wu, *J. Alloys Compd.* 869 (2021) 158918.
- [157] Y. Chen, S. Ji, Y. Wang, J. Dong, W. Chen, Z. Li, R. Shen, L. Zheng, Z. Zhuang, D. Wang, Y. Li, *Angew. Chem. Int. Ed.* 56 (2017) 6937-6941.
- [158] Y. Li, K. Xu, Q. Zhang, Z. Zheng, S. Li, Q. Zhao, C. Li, C. Dong, Z. Mei, F. Pan, S. Dou, *J. Energy Chem.* 66 (2022) 100-106.
- [159] P. Cai, S. Ci, E. Zhang, P. Shao, C. Cao, Z. Wen, *Electrochim. Acta* 220 (2016) 354-362.
- [160] M. Burke, M. Kast, L. Trotochaud, A. Smith, S. Boettcher, *J. Am. Chem. Soc.* 137 (2015) 3638-3648.
- [161] T. Schiros, D. Nordlund, L. Palova, D. Prezzi, L. Zhao, K. Kim, U. Wurstbauer, C. Gutierrez, D. Delongchamp, C. Jaye, D. Fischer, H. Ogasawara, L. Pettersson, D. Reichman, P. Kim, M. Hybertsen, A. Pasupathy, *Nano Lett.* 12 (2012) 4025-4031.
- [162] Y. Chang, F. Hong, C. He, Q. Zhang, J. Liu, *Adv. Mater.* 25 (2013) 4794-4799.

- [163] S. Lin, L. Xia, L. Zhang, J. Feng, Y. Zhao, A. Wang, *Chem. Eng. J.* 424 (2021) 130559.
- [164] X. Chen, D. Chen, G. Li, C. Gong, Y. Chen, Q. Zhang, J. Sui, H. Dong, J. Yu, L. Yu, L. Dong, *J. Alloys Compd.* 873 (2021) 159833.
- [165] J. Li, Y. Kang, W. Wei, X. Li, Z. Lei, P. Liu, *Chem. Eng. J.* 407 (2021) 127961.
- [166] J. Tan, T. Thomas, J. Liu, L. Yang, L. Pan, R. Cao, H. Shen, J. Wang, J. Liu, M. Yang, *Chem. Eng. J.* 395 (2020) 125151.
- [167] D. Chen, J. Zhu, X. Mu, R. Cheng, W. Li, S. Liu, Z. Pu, C. Lin, S. Mu, *Appl. Catal. B* 268 (2020) 118729.
- [168] L. Huang, L. Zuo, Z. He, B. Xiao, H. Zhou, S. Su, Y. Li, T. Bian, A. Yuan, *J. Alloys Compd.* 884 (2021) 161011.
- [169] P. Cai, Y. Hong, S. Ci, Z. Wen, *Nanoscale* 8 (2016) 20048-20055.
- [170] A. Thomas, *Angew. Chem. Int. Ed.* 49 (2010) 8328-8344.
- [171] E. Zhang, Y. Xie, S. Ci, J. Jia, P. Cai, L. Yi, Z. Wen, *J. Mater. Chem. A* 4 (2016) 17288-17298.
- [172] D. MacFarlane, S. Forsyth, J. Golding, G. Deacon, *Green Chem.* 4 (2002) 444-448.
- [173] Z. Li, Z. Xu, X. Tan, H. Wang, C. Holt, T. Stephenson, B. Olsen, D. Mitlin, *Energy Environ. Sci.* 6 (2013) 871-878.
- [174] A. Sadezky, H. Muckenhuber, H. Grothe, R. Niessner, U. Poschl, *Carbon* 43 (2005) 1731-1742.
- [175] Y. Liu, H. Jiang, Y. Zhu, X. Yang, C. Li, *J. Mater. Chem. A* 4 (2016) 1694-1701.

- [176] J. Zhang, Y. Sun, J. Zhu, Z. Gao, S. Li, S. Mu, Y. Huang, *Adv. Sci.* 5 (2018) 1801375.
- [177] K. Artyushkova, A. Serov, S. Rojas-Carbonell, P. Atanassov, *J. Phys. Chem. C* 119 (2015) 25917-25928.
- [178] Y. Liang, Y. Li, H. Wang, J. Zhou, J. Wang, T. Regier, H. Dai, *Nat. Mater.* 10 (2011) 780-786.
- [179] W. Xia, R. Zou, L. An, D. Xia, S. Guo, *Energy Environ. Sci.* 8 (2015) 568-576.
- [180] B. You, N. Jiang, M. Sheng, W. Drisdell, J. Yano, Y. Sun, *ACS Catal.* 5 (2015) 7068-7076.
- [181] Z. Wang, J. Ang, J. Liu, X. Ma, J. Kong, Y. Zhang, T. Yan, X. Lu, *Appl. Catal. B* 263 (2020) 118344.

7. Publications

[1] Zhenzhen Wang, Xiaozhuang Zhou, Huihui Jin, Ding Chen, Jiawei Zhu, Rolf Hempelmann, Lei Chen, and Shichun Mu. "Ionic liquid-derived FeCo alloys encapsulated in nitrogen-doped carbon framework as advanced bifunctional catalysts for rechargeable Zn-air batteries." *Journal of Alloys and Compounds* 908 (2022): 164565. DOI: 10.1016/j.jallcom.2022.164565

[2] Zhenzhen Wang, Xiaozhuang Zhou, Rolf Hempelmann, Lei Chen, and Shichun Mu. "Template-promoted synthesis of nitrogen-doped CNTs from ionic liquid for enhanced ORR activity." **to be submitted.**

8. Eidesstattliche Versicherung

Hiermit versichere ich an Eides statt, dass ich die vorliegende Arbeit selbstständig und ohne Benutzung anderer als der angegebenen Hilfsmittel angefertigt habe. Die aus anderen Quellen oder indirekt übernommenen Daten und Konzepte sind unter Angabe der Quelle gekennzeichnet. Die Arbeit wurde bisher weder im In- noch im Ausland in gleicher oder ähnlicher Form in einem Verfahren zur Erlangung eines akademischen Grades vorgelegt.

[I hereby declare that this dissertation is my own original work except where otherwise indicated. All data or concepts drawn directly or indirectly from other sources have been correctly acknowledged. This dissertation has not been submitted in its present or similar form to any other academic institution either in Germany or abroad for the award of any other degree.]

Ort, Datum [Place, Date]

(Unterschrift) [(Signature)]